N°d'ordre NNT : 2020LYSEI081

THESE de DOCTORAT DE L'UNIVERSITE DE LYON
opérée au sein de
L'Institut National des Sciences Appliquées de Ly*on

***Ecole Doctorale** MEGA ED162*
(Mécanique, Energétique, Génie Civil, Acoustique)

***Spécialité de doctorat** : Génie Mécanique*

Soutenue publiquement le 28/09/2020, par :
(Pierre Joseph Benjamin Brossier)

Combined analytical and empirical modelling of power losses in Rolling Element Bearings

Devant le jury composé de :

Harmand, Souad	*professeur des universités UPHF*	*Président*
Seabra, Jorge	*professeur des universités Universidade do Porto*	*Rapporteur*
Bouyer, Jean	*maître de conférences, HdR Université de Poitiers*	*Rapporteur*
Ville, Fabrice	*professeur des universités INSA Lyon*	*Directeur de thèse*
Changenet, Christophe	*HdR ECAM Lyon*	*Co-directeur de thèse*
Jérôme, Belmonte	*ingénieur Airbus Helicopters*	*Invité*

Département FEDORA – INSA Lyon - Ecoles Doctorales – Quinquennal 2016-2020

SIGLE	ECOLE DOCTORALE	NOM ET COORDONNEES DU RESPONSABLE
CHIMIE	**CHIMIE DE LYON** **http://www.edchimie-lyon.fr** Sec. : Renée EL MELHEM Bât. Blaise PASCAL, 3e étage **secretariat@edchimie-lyon.fr** INSA : R. GOURDON	**M. Stéphane DANIELE** Institut de recherches sur la catalyse et l'environnement de Lyon IRCELYON-UMR 5256 Équipe CDFA 2 Avenue Albert EINSTEIN 69 626 Villeurbanne CEDEX **directeur@edchimie-lyon.fr**
E.E.A.	**ÉLECTRONIQUE, ÉLECTROTECHNIQUE, AUTOMATIQUE** **http://edeea.ec-lyon.fr** Sec. : M.C. HAVGOUDOUKIAN **ecole-doctorale.eea@ec-lyon.fr**	**M. Gérard SCORLETTI** École Centrale de Lyon 36 Avenue Guy DE COLLONGUE 69 134 Écully Tél : 04.72.18.60.97 Fax 04.78.43.37.17 **gerard.scorletti@ec-lyon.fr**
E2M2	**ÉVOLUTION, ÉCOSYSTÈME, MICROBIOLOGIE, MODÉLISATION** **http://e2m2.universite-lyon.fr** Sec. : Sylvie ROBERJOT Bât. Atrium, UCB Lyon 1 Tél : 04.72.44.83.62 INSA : H. CHARLES **secretariat.e2m2@univ-lyon1.fr**	**M. Philippe NORMAND** UMR 5557 Lab. d'Ecologie Microbienne Université Claude Bernard Lyon 1 Bâtiment Mendel 43, boulevard du 11 Novembre 1918 69 622 Villeurbanne CEDEX **philippe.normand@univ-lyon1.fr**
EDISS	**INTERDISCIPLINAIRE SCIENCES-SANTÉ** **http://www.ediss-lyon.fr** Sec. : Sylvie ROBERJOT Bât. Atrium, UCB Lyon 1 Tél : 04.72.44.83.62 INSA : M. LAGARDE **secretariat.ediss@univ-lyon1.fr**	**Mme Sylvie RICARD-BLUM** Institut de Chimie et Biochimie Moléculaires et Supramoléculaires (ICBMS) - UMR 5246 CNRS - Université Lyon 1 Bâtiment Curien - 3ème étage Nord 43 Boulevard du 11 novembre 1918 69622 Villeurbanne Cedex Tel : +33(0)4 72 44 82 32 **sylvie.ricard-blum@univ-lyon1.fr**
INFOMATHS	**INFORMATIQUE ET MATHÉMATIQUES** **http://edinfomaths.universite-lyon.fr** Sec. : Renée EL MELHEM Bât. Blaise PASCAL, 3e étage Tél : 04.72.43.80.46 **infomaths@univ-lyon1.fr**	**M. Hamamache KHEDDOUCI** Bât. Nautibus 43, Boulevard du 11 novembre 1918 69 622 Villeurbanne Cedex France Tel : 04.72.44.83.69 **hamamache.kheddouci@univ-lyon1.fr**
Matériaux	**MATÉRIAUX DE LYON** **http://ed34.universite-lyon.fr** Sec. : Stéphanie CAUVIN Tél : 04.72.43.71.70 Bât. Direction **ed.materiaux@insa-lyon.fr**	**M. Jean-Yves BUFFIÈRE** INSA de Lyon MATEIS - Bât. Saint-Exupéry 7 Avenue Jean CAPELLE 69 621 Villeurbanne CEDEX Tél : 04.72.43.71.70 Fax : 04.72.43.85.28 **jean-yves.buffiere@insa-lyon.fr**
MEGA	**MÉCANIQUE, ÉNERGÉTIQUE, GÉNIE CIVIL, ACOUSTIQUE** **http://edmega.universite-lyon.fr** Sec. : Stéphanie CAUVIN Tél : 04.72.43.71.70 Bât. Direction **mega@insa-lyon.fr**	**M. Jocelyn BONJOUR** INSA de Lyon Laboratoire CETHIL Bâtiment Sadi-Carnot 9, rue de la Physique 69 621 Villeurbanne CEDEX **jocelyn.bonjour@insa-lyon.fr**
ScSo	**ScSo*** **http://ed483.univ-lyon2.fr** Sec. : Véronique GUICHARD INSA : J.Y. TOUSSAINT Tél : 04.78.69.72.76 **veronique.cervantes@univ-lyon2.fr**	**M. Christian MONTES** Université Lyon 2 86 Rue Pasteur 69 365 Lyon CEDEX 07 **christian.montes@univ-lyon2.fr**

*ScSo : Histoire, Géographie, Aménagement, Urbanisme, Archéologie, Science politique, Sociologie, Anthropologie

Acknowledgements

My gratitude goes to my two thesis directors, Dr. Christophe Changenet and Pr. Fabrice Ville. Their help, advice and support were of the outmost importance throughout the realisation of this thesis.

I would also like to thank Jérôme Belmonte from Airbus Helicopters. His essential feedbacks as well as his inputs from the private sector enabled the production of an academic work oriented towards industrial use.

My appreciation also goes also to my colleague Dr. Romain Quiban, whose daily friendly support was always available, to Dr. Dimitri Niel for the experimental data provided and to all my other colleagues: Dr. Jean-Baptiste Boni, Dr. Thomas Touret, Dr. Guillaume Vouaillat, Emna Ben Younes, Pierre Navet and many others who brought team spirit to such a solitary task.

I would like to extend my gratitude to ECAM and all its staff for their most welcoming work environment, to INSA de Lyon and especially to Sophie De Oliviera, for her administrative support, to ANRT for the opportunity and the means of this CIFRE contract.

I am extremely grateful to my family, to my parents whose support throughout my life has been unconditional; to my brothers and sisters who endured my stubbornness throughout theirs.

Unsurprisingly, I am also very grateful to all my friends and especially to my roommates who helped me finish this thesis despite being confined due to COVID19.

Last but not least, I extend my everlasting gratitude to my accomplice in life, hoping she might finally accept to marry me someday.

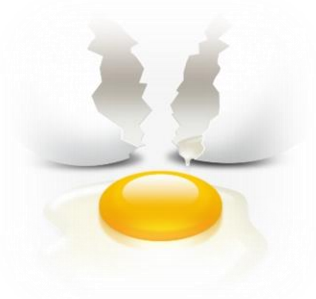

On ne fait pas d'omelette sans casser des œufs

Abstract

The development of the transport industry has led to design lighter and more efficient transmission systems. The components within these transmissions have to withstand the transmitted loads in closer environments. As the housing has become more compact than ever, the cooling system has also become more complex. In that context, Rolling Element Bearings (REBs) are required to produce less heat, to work closer to the gear meshes while having higher life-expectancies. The calculation of REB power loss is essential to quantity the amount of injected oil to cool off these components. This study therefore aims at providing tools to model REB power loss and their thermal behaviour.

As a first step, a bibliographical survey was conducted on REB power losses, including local and global models. A dedicated test rig has been used to analyse the power losses and the thermal behaviour of Deep Groove Ball Bearings. The influence of rotational speed, load, oil injection temperature, oil flow rate and lubrication design has been investigated. The above-mentioned global models have been compared to the experimental data. Finally, a REB thermal model has been developed in order to understand the influence of heat-transfer within REBs on power losses. Comparisons between different lubrication designs and between different geometries have been done. A new formulation to better take into account the REB geometry in the global models has been proposed.

Résumé

Le développement de l'industrie du transport a permis de concevoir des transmissions mécaniques de puissance toujours plus légères et efficientes. Les composants de ces transmissions doivent supporter des efforts transmis dans des environnements de plus en plus restreints. Les carters étant devenus de plus en plus compacts, les systèmes de refroidissement se sont complexifiés. C'est dans ce contexte que les paliers à roulement, plus communément appelés roulements, doivent produire moins de chaleur, opérer dans des espaces plus proches des engrènements, tout en ayant des durées de vie plus grandes. Le calcul des pertes énergétiques des roulements est essentiel pour quantifier la quantité d'huile à injecter pour refroidir ces composants. L'objectif de cette étude est donc de fournir des outils pour modéliser les pertes dans les roulements et leur comportement thermique

Dans un premier temps, une analyse bibliographique a été menée sur les pertes de puissance dans les roulements, incluant des modèles locaux et globaux de pertes de puissance. Un banc d'essais dédié a été utilisé afin d'analyser les puissances dissipées et la thermique de roulements à billes à gorge profonde. Les influences de la vitesse de rotation, du chargement, de la température d'injection, du débit d'huile injecté, des techniques de lubrification ont été examinées. Les modèles globaux précédemment investigués ont été comparés aux données expérimentales. Enfin, un modèle thermique a été développé pour comprendre l'influence des transferts de chaleur dans les pertes de puissance générées par les roulements. Des comparaisons entre différentes lubrifications et différentes géométries ont été faites. Une nouvelle formule du couple résistif a été proposée pour mieux prendre en compte la géométrie du roulement considéré.

Résumé étendu

Ce manuscrit de thèse ayant été rédigé en anglais, un résumé étendu des travaux et des principaux résultats est proposé en français.

La diminution du poids et de l'encombrement des systèmes de transmission de puissance est devenue un prérequis majeur du secteur du transport au cours des années. Ces systèmes de transmission sont en général composés de dentures permettant d'adapter la vitesse, le couple et la direction en fonction du besoin. Les paliers à roulement sont présents de sorte à soutenir les dentures tout en garantissant un frottement minimum. L'amélioration des propriétés des matériaux utilisés a permis d'augmenter le chargement des contacts ainsi que d'obtenir de plus grandes durées de vie tout en réduisant la taille des composants. L'évolution des boites de transmission d'hélicoptères suit la même tendance. Avec une augmentation du couple transmis dans des espaces plus étroits, les pertes de puissance des systèmes de transmission sont plus difficiles à évacuer. Les paliers à roulement, communément appelés roulement, ont par le passé été labelisés paliers sans frottement dans le monde anglosaxon. Néanmoins, ils produisent une certaine quantité de chaleur due à des phénomènes de frottement. Quand le couple transmis est faible, ces pertes de puissance représentent 80 % des pertes totales de la transmission d'hélicoptère. Quand le couple transmis atteint son maximum, ce pourcentage tombe à 20%, les pertes à l'engrènement devenant majoritaires. Dans des conditions réelles de vol, le couple transmis varie et la proportion de chaleur générée aux roulements se situe quelque part entre ces deux valeurs [1]. Les pertes de puissance conduisent à une augmentation des températures et doivent être rigoureusement évacuées du système de transmission.

La proximité entre roulements et dentures augmente l'interdépendance thermique entre composants. La chaleur générée à l'engrènement n'est pas entièrement évacuée par l'huile du système de refroidissement, une partie de cette chaleur passe par conduction au travers des arbres jusqu'aux roulements. Dans certaines conditions de coupure d'huile, des roulements peuvent même devenir les composants les plus chauds du système de transmission [2].

Comprendre comment les roulements produisent de la chaleur et comment ils l'échangent au sein de la boite de transmission est essentiel pour maitriser le comportement thermique d'un tel boitier. Dans cette perspective, la complexité des boites de vitesse d'hélicoptères impose l'utilisation d'un outil efficient, applicable à tout roulement, afin d'en calculer la perte de puissance.

Pour ce faire, les mécanismes de frottement des roulements doivent être appréhendés. Le premier chapitre de cette étude concerne la prédiction des pertes de chaleur des roulements. Après avoir analysé la bibliographie sur les phénomènes locaux de production de chaleur, deux modèles de perte dits « globaux » sont présentés.

Le second chapitre fournit de nouveaux résultats expérimentaux sur les pertes de puissance des roulements. Un banc d'essais dédié à l'analyse thermique des roulements est présenté. Des paramètres d'influence comme la vitesse de rotation, le chargement, la géométrie des roulements et les caractéristiques de lubrification sont évalués. Les modèles globaux sont ainsi ajustés aux données expérimentales et une discussion est alors entamée sur leur adaptabilité.

Le troisième chapitre se concentre sur l'analyse thermique des roulements. Un modèle thermique est développé pour un des roulements testés. Des expériences spécifiques sur le banc d'essais permettent de comparer les températures mesurées et simulées. Enfin, le modèle de perte précédemment ajustée est associé au modèle thermique afin d'analyser l'influence de la lubrification et de la géométrie du roulement sur son comportement thermique.

1.1 Les pertes de chaleur dans le roulement

L'étude des pertes de puissance des paliers à roulement est une discipline complexe et multi- échelle. Au cours des années, les fabricants de roulements ont développé des outils numériques imposants pour modéliser le comportement des roulements. La complexité de ces outils empêche souvent leur utilisation dans des modèles plus larges, par exemple dans le cadre d'une étude intégrale d'une boite de transmission. Ce type d'étude requiert l'utilisation d'un modèle de roulement plus simple, sans calculs itératifs additionnels par exemple. Néanmoins, pour évaluer la justesse d'un tel modèle, les mécanismes de frottement en jeu doivent être examinés.

1.1.1 Sources de frottement

Dans la plupart des systèmes de transmission de puissance, le rendement atteint 98%. Les 2% restant sont dissipés sous forme de chaleur. Cette chaleur est produite par différents phénomènes de frottement qui ont été minutieusement analysées au cours des années. Dans le cadre des roulements, il s'agit principalement du roulement hydrodynamique, de la trainée aérodynamique et du cisaillement du film d'huile du au glissement.

En 1979, Tevaarweck, citant une correspondance privé avec Dawson, révèle une formulation innovante pour le calcul du roulement hydrodynamique et elasto-hydrodynamique [3]. Houpert, citant Tevaarweck, en donne une formulation alternative, prenant en compte les paramètres adimensionnés classiques, afin de calculer un effort résistif de roulement.

$$T_{r_*} = 2.86 \cdot E' \cdot R_{x_*}^2 \cdot G^{0.022} \cdot U^{0.66} \cdot W^{0.47} \cdot k_*^{0.348} \qquad (0.1)$$

Pour ce qui est de la trainée aérodynamique, elle est due au passage de solides dans un fluide, créant un front de pression sur les surfaces et les ralentissant. Dans le cadre des roulements, il s'agit du passage des éléments roulants dans un milieu composé d'un

mélange d'air et d'huile. Cependant au-dessous du seuil d'un million Ndm (produit de la vitesse de rotation d'arbre en tour par minute et du diamètre moyen du roulement en millimètre), ce pôle de perte peut être négligé [4].

Le glissement relatif entre deux surfaces dans un contact lubrifié et chargé crée un frottement non-Newtonien, générant de la chaleur. Ce glissement est à la fois local (provenant de la courbure du contact déformé, d'un éventuel pivotement) et global (provenant du retard des éléments roulants par rapport aux bagues). L'effort de glissement participe à l'équilibre dynamique du roulement. A cause de la non-linéarité de l'expression de cet effort, une méthode inverse est en général utilisée pour calculer la vitesse de glissement à partir du calcul itératif de l'équilibre du roulement. Des études montrent que ce pôle de perte peut-être minoritaire à haute vitesse [5–7], voir négligé pour les roulements à rouleaux[8].

En conclusion, trois principales contributions sont observées dans les pertes de puissance des roulements : le roulement hydrodynamique, la trainée aérodynamique et le cisaillement du film d'huile dû aux glissements relatifs. Ce dernier pôle de perte requiert un modèle d'équilibre du roulement, itératif par essence. La nécessité de prédire facilement la chaleur produite par les roulements rend donc l'étude des phénomènes locaux difficiles. Pourtant, des méthodes alternatives existent pour calculer simplement la perte de puissance des roulements : les modèles globaux. Ces modèles visent à prédire la perte de puissance d'un roulement avec le minimum de paramètres d'entrée. Ils fournissent un couple résistif qui multiplié par la vitesse de rotation de l'arbre, donne la chaleur totale produite. Deux de ces modèles sont présentés : le modèle Harris-Palmgren et le modèle SKF.

1.1.2 Le modèle Harris-Palmgren

Ce modèle de perte a été établi par Palmgren dans le courant des années 1950 [9] et popularisé par Harris [10]. Il sépare le couple de frottement en un couple dépendant de la charge et un couple indépendant de la charge comme le montre l'équation *(0.2*).

$$M_{HPM} = M_1 + M_0 \qquad (0.2)$$

Deux formulations du couple indépendant de la charge, M_0, sont données en fonction du produit de la vitesse de rotation et de la viscosité ($\omega_i \cdot \nu_{oil}$). Dans le cadre de notre étude, seule une de ces contributions est présentée dans l'équation *(0.3)*.

$$M_0 = f_0 \cdot 4.5 \cdot 10^3 \cdot (\omega_i \cdot \upsilon_{oil})^{2/3} * d_m^3 \qquad (0.3)$$

La valeur du coefficient f_0 dépend du type de roulement et de sa lubrification. Il peut également varier d'un facteur deux selon la série du roulement : lourde ou légère selon les termes de Harris. Le produit de la viscosité et de la vitesse de rotation est très caractéristique du roulement hydrodynamique précédemment évoqué.

Le couple dépendant de la charge M_1 est présenté dans l'équation *(0.4)* et dépend de la charge équivalente F_B.

$$M_1 = f_1 \cdot F_B \cdot d_m \quad (0.4)$$

$$f_1 = z \cdot (F_s/C_0)^y \quad (0.5)$$

Pour les roulements à billes, le coefficient f_1 dépend de la charge statique équivalente F_s et d'une paire de coefficients expérimentaux z et y dépendant aussi du type de roulement et de la série du roulement (équation *(0.5)*). Dans le cadre du chargement purement radial, la charge statique équivalente est simplement l'effort radial appliqué [10]. Il peut-être noté que l'étude paramétrique ayant servi à l'élaboration de ce modèle a utilisé des roulements dont le ratio diamètre de bille sur diamètre moyen est proche de 0.2 [9].

	f_0	z	y
Injection d'huile	*4*	*0.0002-0.0004*[i]	*0.55*
Bain d'huile – Arbre horizontal	*2*		

[i]*: en fonction de la série : lourde - légère*

Tableau 0.1 : Coefficients du modèle Harris-Palmgren pour les roulements à billes à gorges profondes

Le Tableau 0.1 fournit les coefficients expérimentaux de ce modèle pour les roulements à billes à gorges profonde. En conclusion, le modèle Harris-Palmgren a l'avantage d'être simple et applicable rapidement à tout type de roulement. Aucune information sur la répartition du chargement du roulement ou de la géométrie fine de celui-ci n'est nécessaire. Seul le diamètre moyen d_m est utilisé pour qualifier l'influence de la géométrie.

1.1.3 Le modèle SKF

Récemment, la société SKF a créé un autre modèle global de calcul des pertes de puissance des roulements. Ce modèle semble provenir d'une interpolation des résultats de leur logiciel de modélisation complet des roulements : BEAST [11,12]. Il sépare trois contributions ici conservées dans leur tournure anglophone : le *rolling*, *sliding* et *drag*. Ces contributions sont donc celles précédemment retenues comme les principaux pôles de pertes de puissance. Cependant, l'auteur argumente que pour le *drag*, il s'agit en réalité d'une combinaison de deux phénomènes : la trainée aérodynamique et le brassage de l'huile par les éléments roulants dans le cadre d'une lubrification par barbotage. Ce modèle est présenté dans l'équation *(0.6)* et sera par la suite détaillé seulement pour les roulements à billes à gorge profonde sous chargement purement axial.

$$M_{SKF} = M_{rr} + M_{sl} + (M_{drag} + M_{splash}) \quad (0.6)$$

Ce modèle utilise différents paramètres géométriques R_1, S_1, K_{rs} et K_z fournis dans le catalogue en fonction de la série du roulement concerné.

Pour le couple de frottement associé au *rolling* (M_{rr} dans l'équation *(0.7)*), le produit de la viscosité et de la vitesse de rotation est encore une fois retrouvé à une puissance proche de 2/3 et rappelle à nouveau la formulation du roulement hydrodynamique. Les deux termes φ_{rs} et φ_{ish} sont respectivement le facteur de réalimentation et le facteur de réduction thermique qui diminuent le *rolling* à haute vitesse et à haute viscosité.

$$M_{rr} = 1.17 \cdot 10^{7} \cdot \varphi_{rs} \cdot \varphi_{ish} \cdot G_{rr} \cdot (\omega_i \cdot \upsilon_{oil})^{0.6} \quad (0.7)$$

$$G_{rr} = R_1 \cdot d_m^{1.96} \cdot F_r^{0.54} \quad (0.8)$$

Le couple de frottement associé au *sliding* (M_{sl} dans l'équation *(0.9)*) ressemble à un produit coefficient de frottement – chargement, ce coefficient dépendant d'un facteur de partage φ_{bl} permettant de passer d'une valeur dite limite μ_{bl} à une valeur du régime de lubrification elasto-hydrodynamique μ_{EHL}. Ces coefficients de frottement, sensés représenter les régimes de lubrification dépendent du type de roulement et de l'huile utilisée.

$$M_{sl} = (\varphi_{bl} \cdot \mu_{bl} + (1 - \varphi_{bl}) \cdot \mu_{EHL}) \cdot G_{sl} \quad (0.9)$$

$$G_{sl} = S_1 \cdot d_m^{-0.26} \cdot F_r^{5/3} \quad (0.10)$$

Les deux termes restants, M_{drag} et M_{splash}, sont prépondérants à haute vitesse (> 1M NdM) ou dans le cadre d'une lubrification par bain d'huile. Dans le cadre de cette étude ils ne seront pas considérés.

Le modèle SKF est donc composé de différentes briques qui tentent de reproduire les phénomènes physiques de frottement au sein du roulement. Il nécessite plus de paramètres que le modèle Harris-Palmgren, notamment des paramètres dépendants de la série du roulement (empêchant donc son application en dehors des roulements SKF). Des études montrent cependant sa capacité à reproduire des essais expérimentaux en maniant seulement μ_{bl} et μ_{EHL} [13,14].

1.1.4 Conclusion

En conclusion, le roulement hydrodynamique et le cisaillement dû au glissement sont les deux principaux pôles de pertes des roulements opérant en dessous du seuil de haute vitesse (> 1M NdM). Le roulement hydrodynamique dépend de la charge et est proportionnel au produit vitesse de rotation par viscosité à la puissance deux-tiers. Le cisaillement associé au glissement n'est pas calculable sans un procédé itératif.

Les deux modèles globaux utilisés par l'industrie sont simples à mettre en œuvre et s'appliquent à tous types de roulements. Le modèle Harris-Palmgren sépare la perte de puissance en deux entités indépendamment mesurées. Le modèle SKF conserve les pôles de pertes cités ci-dessus et donne une formulation analytique au cisaillement.

Ces deux modèles sont bien intégrables à une modélisation complète d'une boite de transmission d'hélicoptère. Cependant, il semble qu'il faille les valider expérimentalement afin de recaler leurs coefficients.

1.2 Investigations expérimentales

Dans le chapitre précédent, la prédiction des pertes de puissance des roulements a été soulignée comme étant la pierre angulaire de l'analyse thermique des boites de transmission de puissance. Deux modèles dit "globaux" ont été détaillés. Leur facilité d'utilisation a montré qu'ils demeurent des outils adaptés à la fois à la recherche et à l'industrie

Afin de pouvoir justifier de leur fiabilité et de leur adaptabilité, un banc d'essai dédié est utilisé afin de fournir de nouveaux résultats expérimentaux concernant la perte de puissance des roulements et des paramètres d'influence l'impactant.

1.2.1 Présentation du banc d'essai utilisé

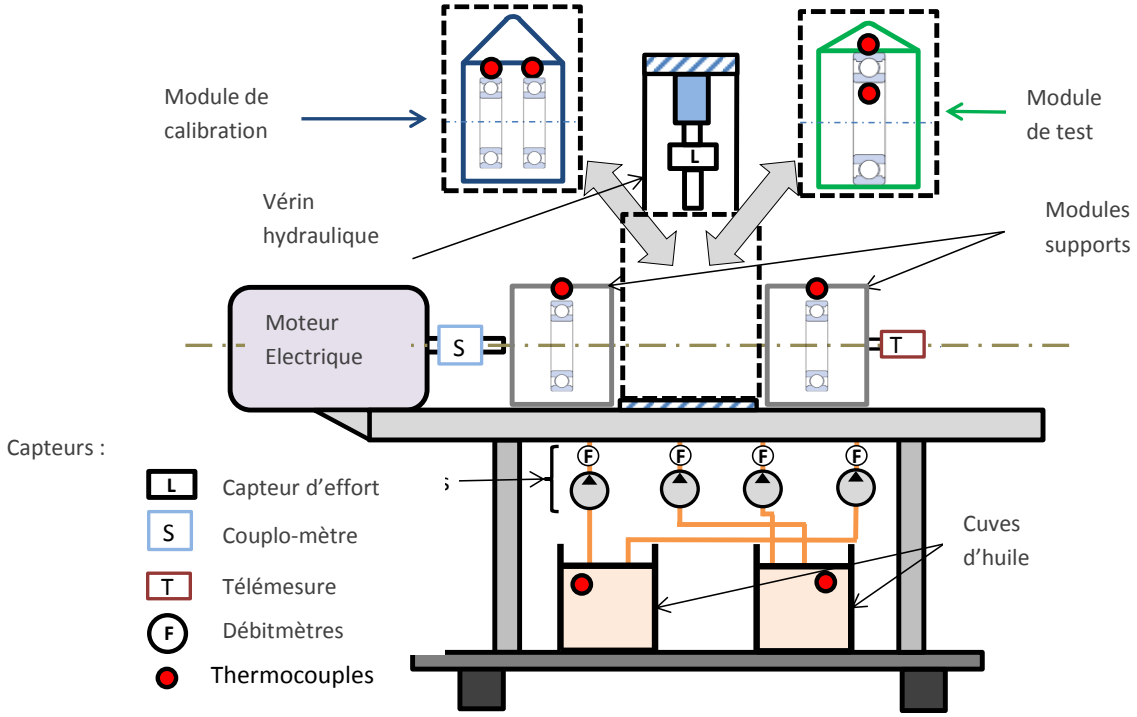

Figure 0.1 : Schéma du banc d'essai

Ce banc d'essai modulable présenté dans la Figure 0.1 a été conçu afin de pouvoir étudier différents roulements. Il est composé de deux blocs appelés "supports", intégrant des roulements de type A. Ces blocs sont répartis de part et d'autre d'un bloc central appelé « mesure » intégrant un roulement de type B. Afin de mesurer uniquement le couple résistif du roulement type B, les couples résistifs des roulements type A doivent être soustraits à la mesure totale du couple résistif. Une phase de calibration où le bloc mesure est remplacé par un bloc calibration contenant deux roulements type A est donc effectuée en amont. En conclusion, ce banc d'essai a permis de mesurer indépendamment le couple résistif de deux types de roulements. Les caractéristiques des roulements type

A et type B sont présentées dans la Tableau 0.2. Une description plus détaillée de ce banc d'essai est faite par Niel [15].

		Type A	***Type B***
Type		*Roulement à bille à gorge profonde*	*Roulement à bille à gorge profonde*
Diamètre moyen [mm]	d_m	*61*	*85*
Diamètre extérieur [mm]	d_e	*72*	*95*
Diamètre intérieur [mm]	d_i	*50*	*75*
Largeur [mm]	B	*12*	*10*
Capacité statique de base [kN]	C_0	*11.8*	*14.3*
Diamètre des billes [mm]	*D*	*6.75*	*5.55*
Nombre de bille [-]	*Z*	*16*	*26*

Tableau 0.2 : Caractéristiques des roulements étudiés

Différents paramètres d'influence sont investigués au cours des essais puis comparés aux modèles de pertes :

- La vitesse de rotation, qui varie pour tous les essais entre 1000 et 10 000 tr/min
- La charge radiale pour le roulement type A uniquement entre 250 et 2500 N.
- La différence entre lubrification par bain d'huile et par injection pour le roulement type A uniquement.
- L'impact de la montée en température pour le roulement A en lubrification par bain d'huile. L'impact de la température d'injection pour le roulement type B uniquement.
- La comparaison entre les roulements type A et type B, lors d'une campagne par injection faiblement chargée
- L'impact du débit d'huile injecté pour le roulement type B uniquement.

1.2.2 Le modèle Harris-Palmgren : résultats

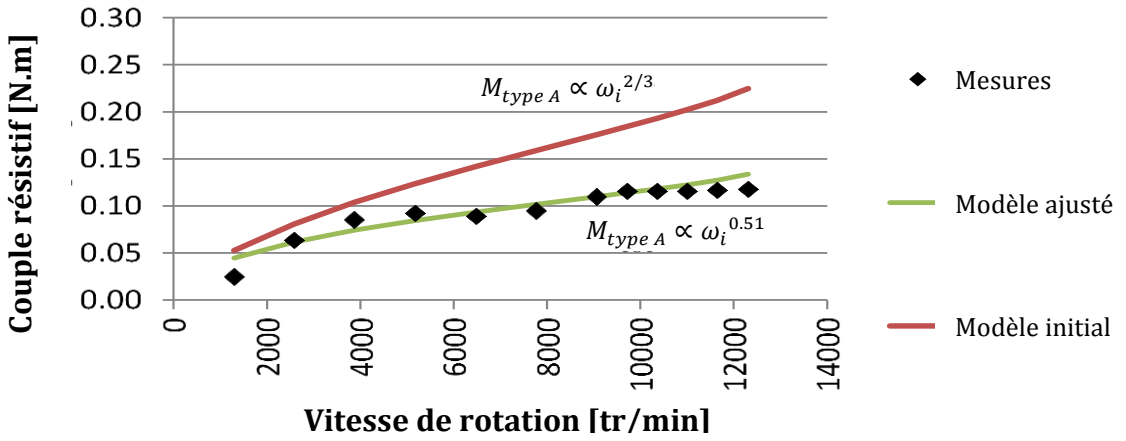

Figure 0.2 : Comparaison entre les modèles et la mesure du couple résistif par rapport à la vitesse de rotation

1.2.3 Le modèle Harris-Palmgren : résultats

Figure 0.2, le modèle Harris-Palmgren initial n'est pas en accord avec l'évolution du couple par rapport à la vitesse de rotation de l'arbre. Cette expérience sur le roulement est faiblement chargée (300N) et a permis de modifier la valeur de l'exposant de la vitesse et le coefficient f_0 dans l'équation *(0.11)*.

$$M_{0-injection} = 7.7 \cdot 4.5 * 10^3 \cdot \omega_i^{0.51} \cdot {v_{oil}}^{2/3} \cdot d_m^3 \qquad (0.11)$$

De la même manière, l'impact de la charge sur le couple résistif a nécessité la modification du paramètre z dans la contribution dépendante de la charge, mais pas de l'exposant y.

La différence entre les lubrifications par bain ou par injection se traduit par une modification de 13% du paramètre f_0, la lubrification par bain d'huile produisant légèrement moins de pertes.

L'impact de la température, que ce soit la température d'injection pour le roulement B ou de la montée en température pour le roulement A, est bien pris en compte par la présence de la viscosité à la puissance 2/3 dans le modèle.

La comparaison entre les deux roulements est faite sur des essais faiblement chargés, pour une température d'injection de 70°C et pour des débits d'injection entre 12 et 15 L/h. Cette comparaison à iso-débit est justifiée par le fait que, bien que le diamètre moyen des roulements soit différent, le volume intérieur du roulement est du même ordre de grandeur. D'autre part, l'impact du débit injecté est minime pour une température d'injection de 70°C.

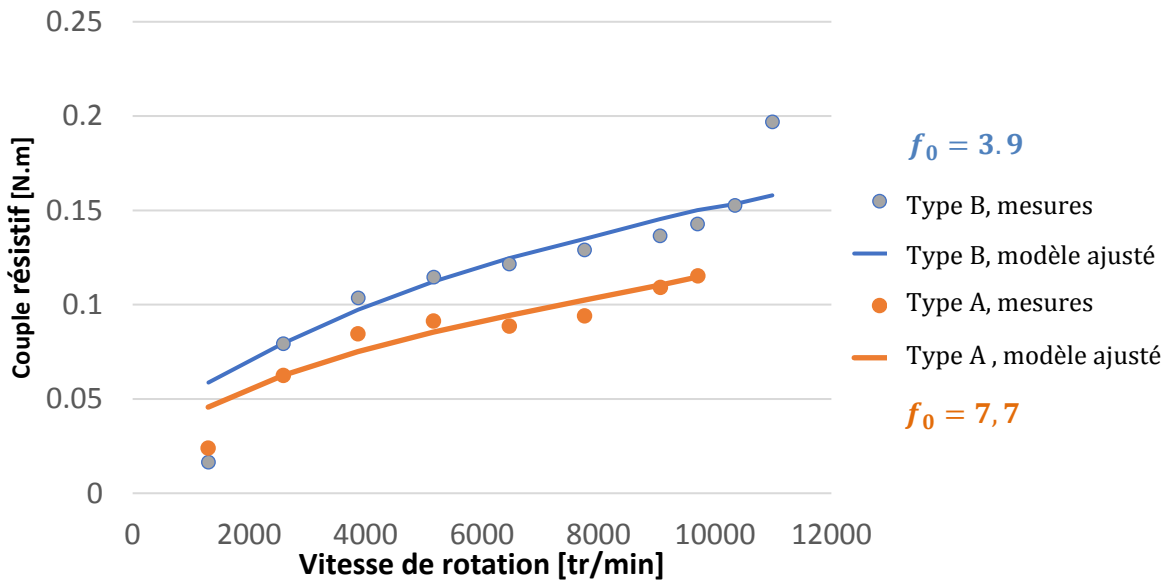

Figure 0.3 : Comparaison des modèles ajustés et des mesures de couple résistif pour les deux roulements testés.

La comparaison entre le couple résistif produit par les deux roulements testés est présentée sur la Figure 0.3. L'évolution du couple par rapport à la vitesse est similaire, le

roulement type B, dont le diamètre moyen est 40% plus important que celui du type A, produit en moyenne 25% de pertes de puissance en plus. Du fait de la présence du diamètre moyen d_m à la puissance trois dans le modèle Harris-Palmgren, deux coefficients f_0 sont nécessaires pour ajuster le modèle sur les deux roulements.

L'influence du débit d'huile injecté sur le couple résistif a été observée pour le roulement type B lors d'essais faiblement chargés pour trois débits d'huile [15 ; 25; 35 L/h] et trois températures d'injection [60;70;90°C].

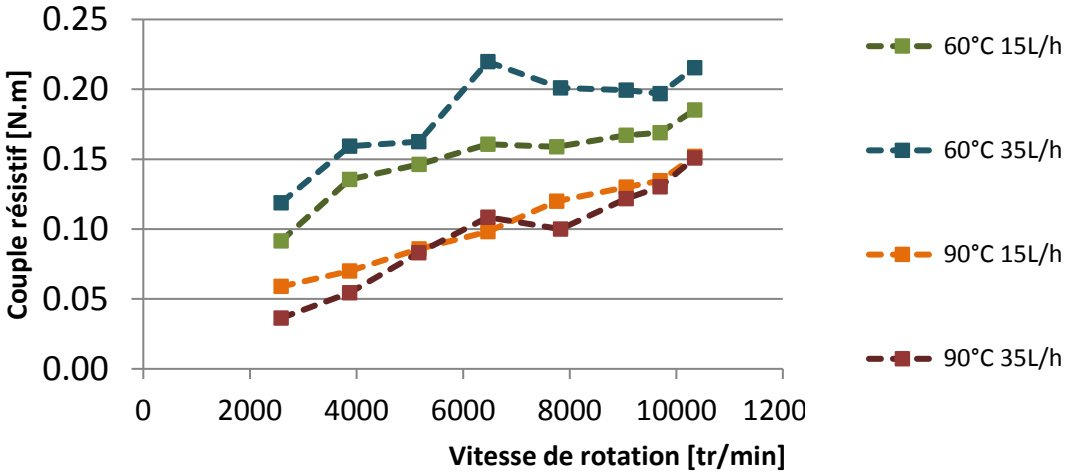

Figure 0.4 : Comparaisons expérimentales du couple résistif par rapport au débit d'huile injecté à deux températures d'injection différentes.

Sur la Figure 0.4, le couple résistif mesuré pour les valeurs limites de cette campagne d'essais est présenté. Il est observé que le débit d'huile a un impact plus important à faible température d'injection qu'à haute température d'injection. L'influence du débit d'huile semble donc intimement liée à la température d'injection.

1.2.4 Le modèle SKF : résultats

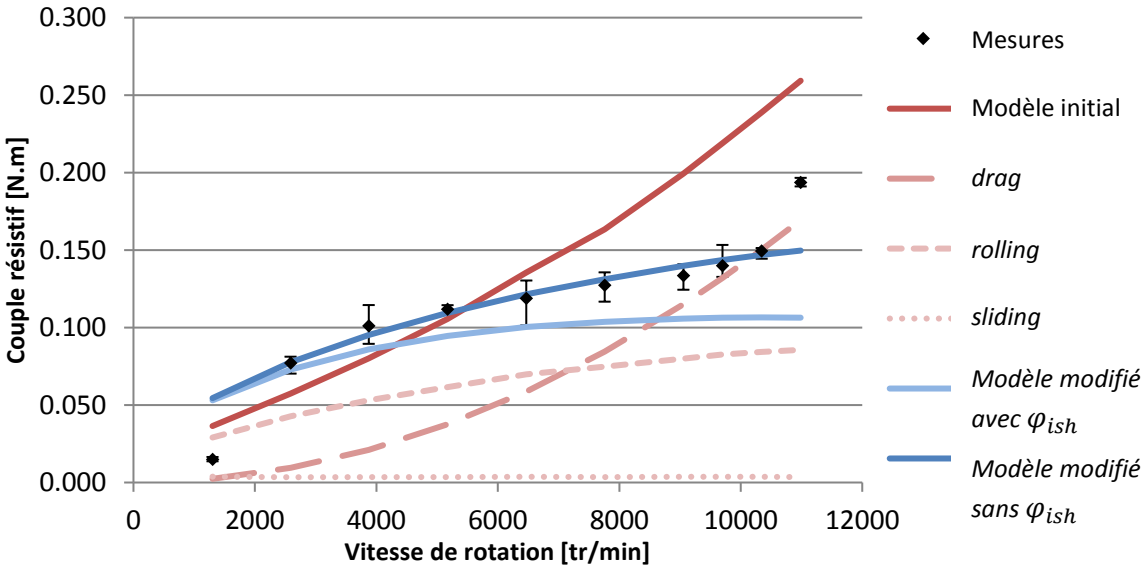

Figure 0.5 : Comparaison entre le modèle initial, ses contributions, le modèle modifié et l'expérience

Le modèle SKF sépare le couple résistif en trois contributions : *rolling, sliding* et *drag*. L'évolution de ces contributions par rapport à la vitesse de rotation est présentée sur la Figure 0.5 pour des essais faiblement chargés [400N].

Sur cette figure, nous pouvons observer que le *drag* est trop important et ne suit pas la même allure que les mesures du couple résistif. Puisque le roulement est étudié en deçà du seuil de haute-vitesse défini à 1 million NdM, le *drag* a été supprimé du modèle modifié. De plus, sur ces essais faiblement chargés, le *rolling* est initialement trop faible comparé aux mesures. Un seuil minimal, équivalent à 10% de la charge statique de base du roulement, est appliqué à l'effort radial dans la formulation du *rolling.* Enfin, la prise en compte du facteur de réduction thermique φ_{ish} ne permet pas de rendre compte de l'évolution du couple résistif. La raison sous-jacente réside dans le calcul actuel de la viscosité : la température de la bague extérieure étant considérée, ce terme associé au comportement thermique du roulement devient inutile.

Le modèle SKF modifié ainsi obtenu est comparé à certains des paramètres d'influence précédemment étudiés :

- La vitesse de rotation, qui varie pour tous les essais entre 1000 et 10 0000 tr/min
- La charge radiale pour le roulement type A uniquement entre 250 et 2500 N.
- L'impact de la montée en température pour le roulement A en lubrification par bain d'huile. L'impact de la température d'injection pour le roulement type B uniquement.
- La comparaison entre les roulements type A et type B, lors d'une campagne par injection faiblement chargée

L'impact de la vitesse de rotation sur le couple a permis d'élaguer les contributions du modèle SKF afin d'obtenir le modèle modifié.

Pour ce qui est de l'impact de la charge sur le couple résistif, un seuil bas a été mis en place sur le *rolling* pour les faibles charges comme précédemment évoqué. A plus hautes charges, il a été constaté que le *rolling* suffit à prédire l'augmentation du couple. Si celui-ci est considéré comme indépendant de la charge, le *sliding* permet à lui seul de prédire l'évolution du couple. Ces deux contributions sont donc en concurrence pour traiter de l'impact de la charge sur le couple résistif. Nous pouvons noter que dans le cadre de nos essais, seul le coefficient μ_{EHL} a un impact sur le *sliding*.

Concernant l'impact de la température, la viscosité à la puissance 0.6 devrait réussir à modéliser l'évolution du couple. Cependant le facteur de réduction φ_{rs} tend à amoindrir l'impact d'une viscosité élevée, ce qui ne correspond pas aux observations expérimentales.

Enfin, la comparaison entre les roulements A et B est présentée sur la Figure 0.6.

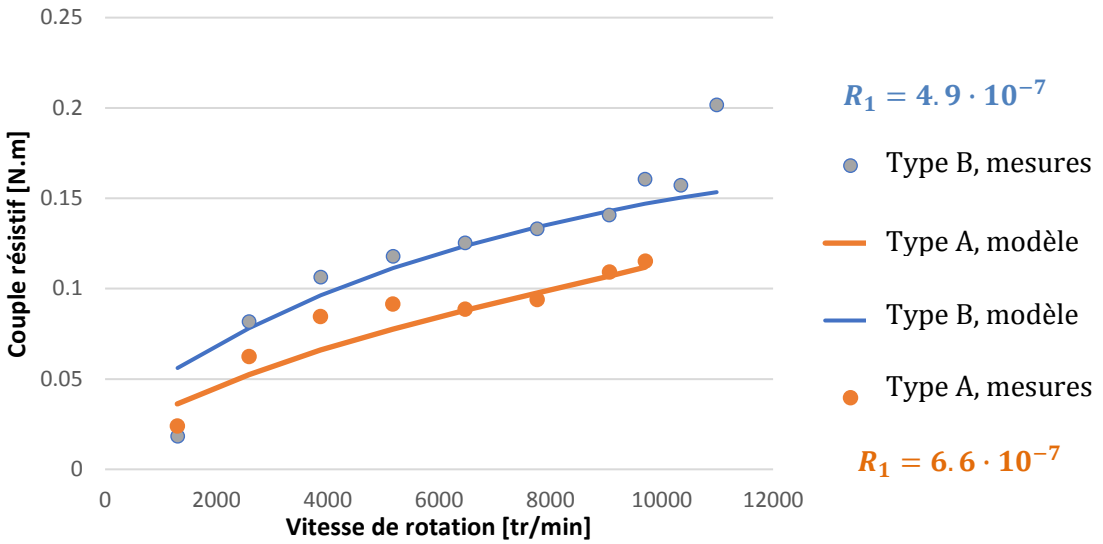

Figure 0.6 : Comparaison entre les modèles et les mesures du couple résistif pour les deux roulements testés

De la même façon que pour le modèle Harris-Palmgren, les deux coefficients R_1 doivent être ajustés afin de pouvoir rendre compte de l'évolution du couple résistif d'un roulement à l'autre. La différence entre les deux coefficients est cependant plus faible pour le modèle SKF que pour le modèle Harris-Palmgren. De plus, aucun des modèles ne prend en compte le débit d'injection qui a un impact sur le couple résistif à certaines températures d'injection.

Le fait que l'impact du débit d'huile dépende de la température d'injection montre que des phénomènes thermiques influencent directement la perte de puissance du roulement. De plus, le fait que les deux modèles ne puissent prédire le couple résistif des deux roulements avec un seul coefficient universel soulève aussi des questions. Les phénomènes thermiques en jeu amènent-ils à des comportements thermiques différents pour les deux roulements ? La thermique des roulements testés doit-être modélisée afin d'en saisir l'impact. Pour ce faire, un modèle thermique des roulements et du banc d'essai est développé.

1.3 Modélisation thermique

Comme vu dans le chapitre précédent, les phénomènes thermiques à l'œuvre au sein des roulements sont intimement liés aux caractéristiques de la lubrification. Afin de modéliser thermiquement ces phénomènes, le débit d'huile arrivant à rentrer dans le roulement doit être quantifié. En effet, des essais ont montré que dans le cadre d'une lubrification par jet d'huile, toute l'huile injectée ne traverse pas le roulement et une partie est refoulée avant de pénétrer dans le roulement [16]. Le ratio du débit d'huile traverssant le roulement divisé par le débit total injecté s'appelle le coefficient de pénétration noté α et est investigué dans un premier temps.

La méthode des réseaux thermiques est ensuite employée afin de modéliser le comportement thermique des roulements testés. Des essais spécialement conçus pour étudier la réponse thermique du banc d'essais sont comparés aux résultats du modèle. Enfin, le modèle thermique est utilisé pour étudier l'influence du débit d'huile à différentes températures d'injection sur le couplage entre pertes de puissance et comportement thermique. De même, les comportements thermiques des deux roulements sont comparés.

1.3.1 Mesure du coefficient de pénétration

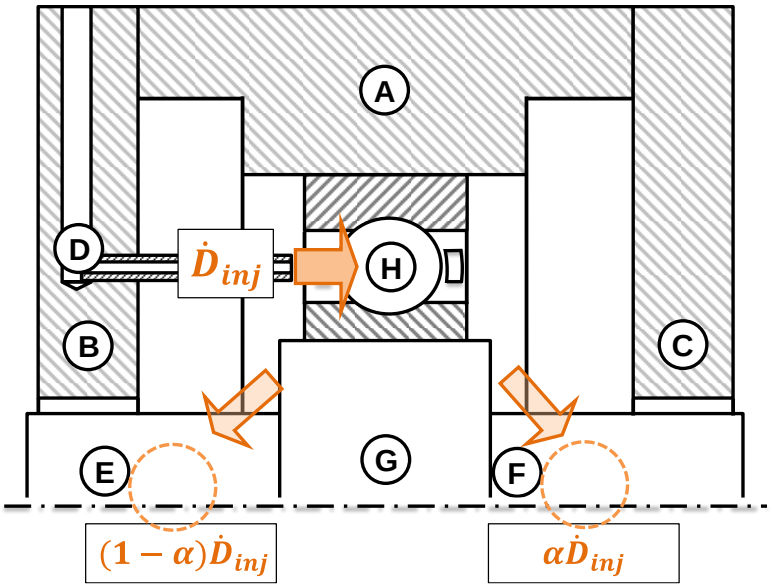

Figure 0.7: Schéma de répartition de l'huile injectée

Sur la Figure 0.7Figure 3.1 est présenté la répartition de l'huile dans un roulement lubrifié par l'injection. Le coefficient de pénétration est déterminé en mesurant le débit de la sortie d'huile opposée à l'injection. Une campagne d'essai a été réalisée sur le roulement B entre 3000 et 10 000 tr/min pour deux températures d'injection [60 ;70°C] et trois débits d'huile [15 ;20 ;30 L/h]. Les conclusions de cette enquête expérimentale sont énumérées ci-dessous :

- Le coefficient de pénétration est indépendant de la température d'huile
- Le coefficient de pénétration augmente avec le débit injecté
- Le coefficient de pénétration diminue avec la vitesse d'injection (pour un débit de 20 L/h, il passe de 45% à 3000 tr/min à 30 % à 10 000 tr/min)

La mesure du coefficient de pénétration est nécessaire pour quantifier la quantité d'huile échangeant de la chaleur dans le roulement. Connaissant cette quantité, les échanges entre l'huile et le roulement peuvent être étudiés.

1.3.2 La méthode des réseaux thermiques

Afin d'analyser le comportement thermique des roulements, la méthode des réseaux thermiques est utilisée. Cette méthode découpe le système étudié en nœuds isothermes

et modélise les échanges de chaleur entre nœuds par des résistances thermiques. Un bilan énergétique est appliqué à chaque nœud qui voit sa température modifiée en fonction de la chaleur échangée avec ses nœuds voisins.

Dans l'enceinte du roulement, l'huile injectée est pulvérisée par le passage des éléments roulants et un brouillard d'huile se forme. Ce brouillard peut être considéré comme un milieu homogène dont les caractéristiques dépendent de la fraction d'huile *X*. Cette fraction d'huile dépend de la vitesse de rotation, du débit injecté et de la dimension du roulement. Par le passé, des études ont établi une corrélation pour la calculer dans le cadre d'une lubrification pas la bague intérieure [17,18]. La formulation utilisée dans cette étude prend en compte le coefficient de pénétration dans le calcul du débit injectée (équation (*0.12*)).

$$\boldsymbol{X = 314 \cdot \frac{(\alpha \cdot \dot{D}_{inj})^{0.37}}{\omega \cdot d_m^{1.7}}} \qquad (0.12)$$

Dans le cadre de l'étude des roulements, un réseau simplifié des roulements a été développé par des études précédentes [4,19]. Ce réseau ne modélise pas finement les contacts et ne requiert pas d'information sur la distribution des pertes de puissance au sein du roulement. L'intégralité de la perte de puissance est injectée dans un nœud fictif dénommé « central » fusionnant l'ensemble des billes, de la cage et des contacts (numéroté #12 par la suite). Dans le cadre d'essais expérimentaux, la mesure du couple résistif permet d'injecter directement la chaleur produite. Dans le cadre de simulations numériques, la chaleur injectée est calculée par les modèles globaux précédemment modifiés.

1.3.3 Analyse du réseau thermique du banc d'essai

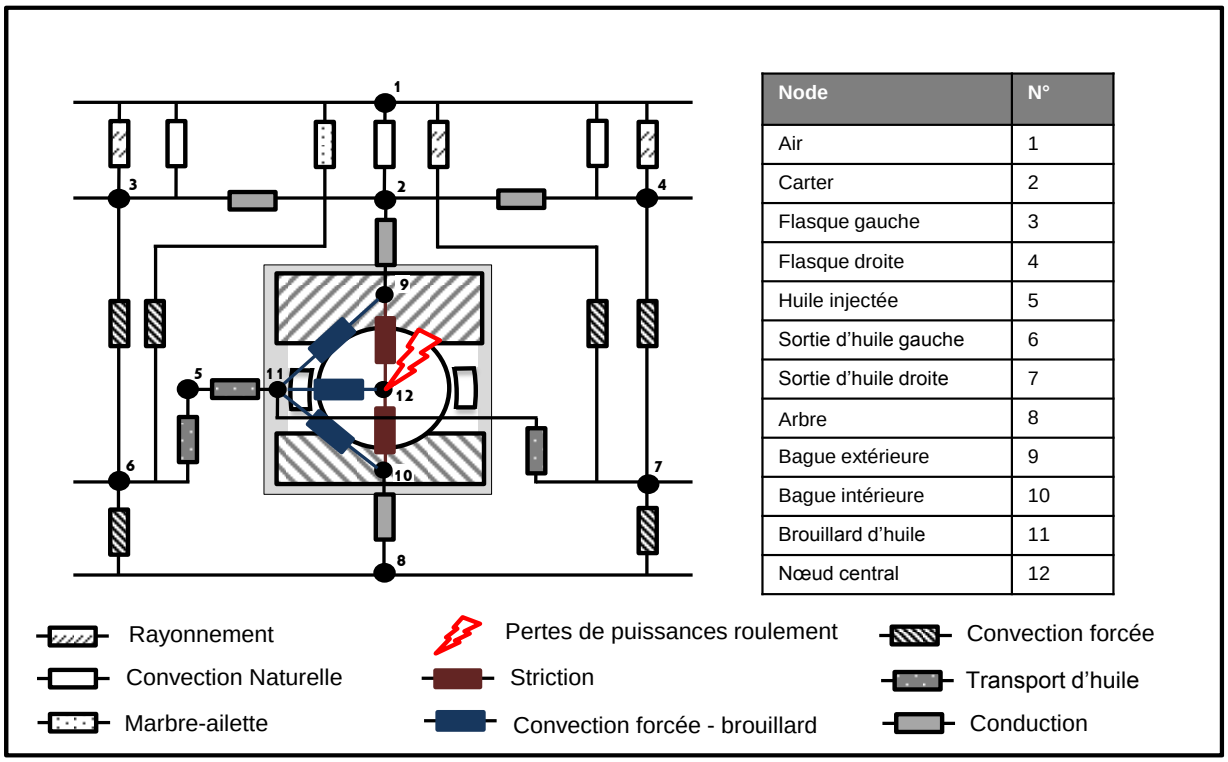

Node	N°
Air	1
Carter	2
Flasque gauche	3
Flasque droite	4
Huile injectée	5
Sortie d'huile gauche	6
Sortie d'huile droite	7
Arbre	8
Bague extérieure	9
Bague intérieure	10
Brouillard d'huile	11
Nœud central	12

Figure 0.8 : Présentation du réseau thermique du banc d'essai intégrant le roulement type B

Sur la ***Figure*** 0.8, le réseau du bloc mesure intégrant le roulement type B est présenté. Les résistances sont calculées à partir de formulations analytiques issues de la littérature. On peut ajouter que :

- Les bagues et le nœud central échangent par convection forcée avec un nœud représentant le brouillard d'huile.
- Les flux de chaleur aux contacts billes-bagues passent par les ellipses de contact, provoquant une striction du flux.
- Entre le nœud représentant l'injection, le brouillard et les sorties d'huile, des résistances de transport intégrant le coefficient de pénétration sont utilisées
- La conduction à travers les solides est représentée par des résistances considérant un flux unidirectionnel.
- L'échange entre le carter, les flasques et l'air extérieur est fait par des résistances de convection naturelle et de rayonnement. Le marbre du banc d'essai est aussi modélisé, sous la forme d'une ailette.

Un essai de refroidissement a permis de valider la prise en compte des échanges entre le bloc mesure et l'air extérieur. Une bonne corrélation entre les températures mesurées et simulées a été observée.

De même, un essai de phase de chauffe du roulement a été effectué à basse vitesse (4700 tr/min) afin d'évaluer les échanges entre l'huile injectée, le roulement et les parois

intérieures du bloc mesure. A cette vitesse, la chaleur apportée par l'injection est équivalente à celle produite par le roulement (respectivement 79 et 90W). La mesure du coefficient de pénétration a permis une bonne corrélation entre mesures et simulations.

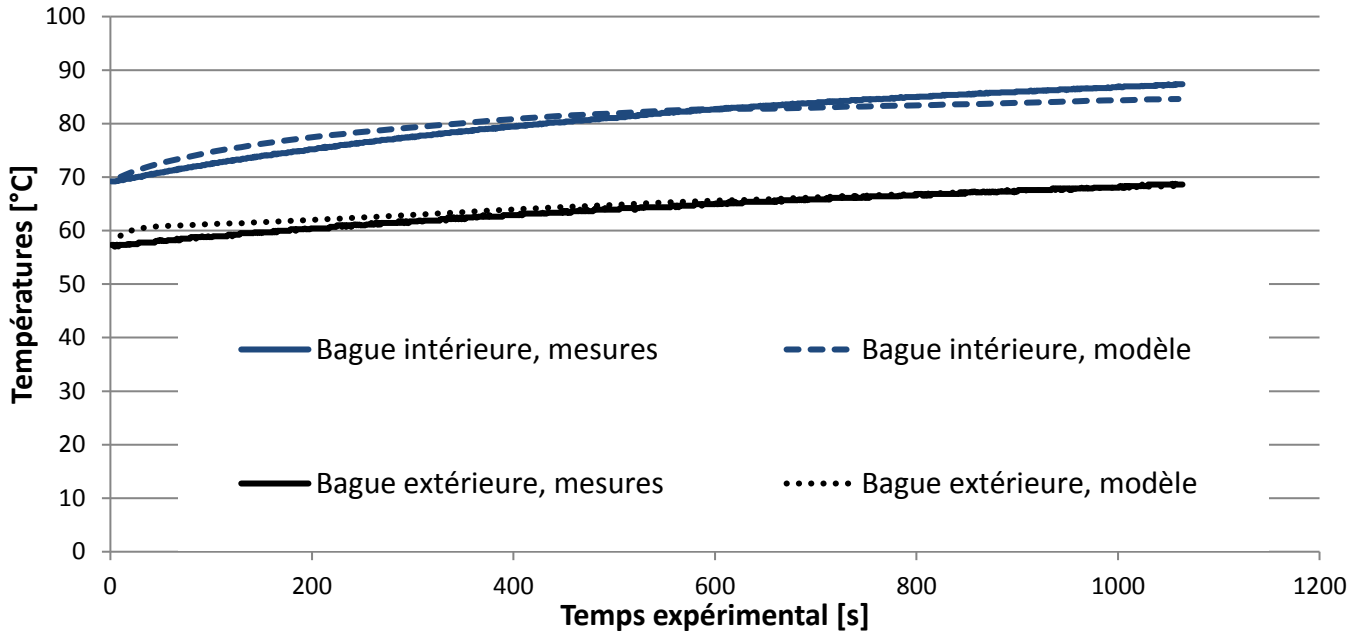

Figure 0.9 : Comparaison entre les températures mesurées et modélisées sur l'essai 9700 tr/min

Un essai a été réalisé à plus haute vitesse [9700 tr/min] avec une mesure de la température de la bague intérieure. Le roulement faiblement chargé (1kN) est lubrifié par une injection d'huile de 20 L /h à 67°C. Le roulement produit alors plus de perte de puissance (200W). Sur la Figure 0.9, force est de constater que les évolutions de température entre les mesures des bagues et leurs simulations thermiques coïncident.

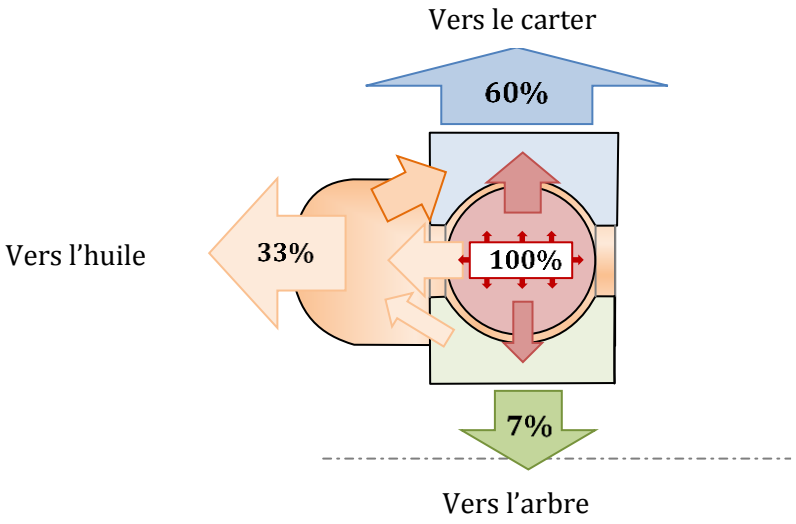

Figure 0.10: Coefficient de répartition du flux à 9700 tr/min

Pour cette expérience, l'huile injectée a un rôle refroidissant sur le roulement. Les coefficients de répartition de flux sont présentés sur la Figure 0.10. L'huile évacue une

portion de la chaleur générée (33%). L'arbre évacue quant à lui peu de calorie (7%) et le carter draine la majeure partie des calories (60%). Le chemin de la chaleur vers le carter passe en partie par des phénomènes convectifs avec le brouillard d'huile. Les échanges convectifs avec le brouillard d'huile dépendent fortement de la fraction d'huile *X*. Une fraction d'huile plus importante entrainerait une température de bague intérieure plus faible, et inversement [20]. Le calcul de la fraction d'huile pour l'injection par jet d'huile est donc validé.

Finalement, le comportement thermique du roulement a été modélisé. Le coefficient de pénétration est nécessaire pour quantifier la quantité d'huile entrant dans le roulement, et donc, quantifier la chaleur que l'huile est en mesure d'extraire du roulement. De plus, le coefficient de pénétration est nécessaire pour quantifier la fraction d'huile dans le cadre d'une lubrification par jet. Cette fraction d'huile permet de caractériser les échanges thermiques entre le brouillard d'huile et le roulement. La comparaison entre résultats expérimentaux et les prédictions du modèle est concluante. Ce modèle thermique ainsi validé peut désormais être utilisé afin d'enquêter sur l'impact de la lubrification et de la géométrie du roulement sur la génération de perte de puissance.

1.3.4 Modélisation de l'impact de la lubrification

Le modèle thermique du roulement précédemment validé est désormais utilisé en tandem avec le modèle Harris-Palmgren ajusté. Le calcul de la viscosité et l'actualisation des pertes de puissance sont intégrées à l'algorithme itératif de la modélisation thermique du roulement.

Le roulement type B est traité en premier, avec deux températures d'injection [60-90°C] et deux débits d'huile injectée [15-35 L/h]. La simulation se fait jusqu'à l'obtention du régime stabilisé. Afin de comparer l'impact simulé du débit d'huile aux expériences évoquées dans le chapitre précédent, le couple résistif obtenu à 35 L/h est divisé par celui obtenu pour 15 L/h.

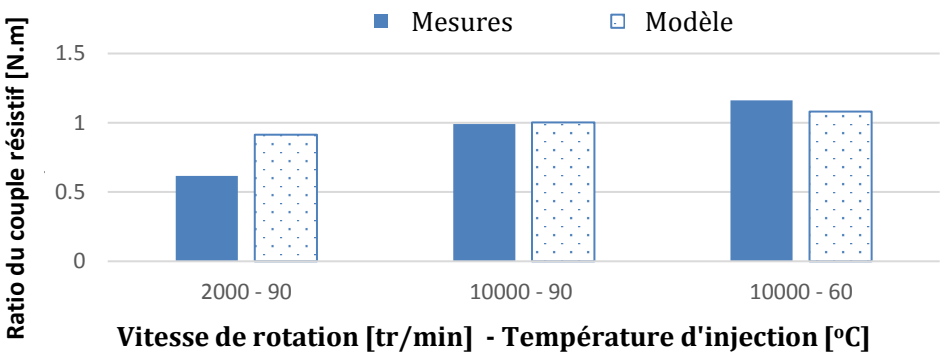

Figure 0.11 : Comparaison du ratio du couple résistif en fonction des conditions opératoires [tr/min - °C]

La ***Figure*** 0.11 montre que les ratios obtenus par la simulation suivent l'expérience. La différence d'ordre de grandeur entre l'expérience et la simulation est due au fait que

l'expérience n'est pas stabilisée en température. Il en ressort qu'injecter plus d'huile à haute température (90°C) et à basse vitesse (2000 tr/min) réduit le couple résistif en augmentant la température du roulement. Inversement, injecter plus d'huile à basse température (60°C) et à haute vitesse (10000 tr/min) augmente le couple en abaissant la température. A haute température d'injection (90°C) et haute vitesse (10000 tr/min) l'impact du débit sur le couple résistif est minime puisqu'un équilibre entre l'amélioration des échanges convectifs et le réchauffement du roulement est atteint. Sur la plage de débit traité, celui-ci n'a donc pas un impact direct sur les mécanismes de pertes mais un impact thermique indirect *via* la viscosité. Un unique paramètre f_0 est donc possible à condition de modéliser thermiquement le roulement.

1.3.5 Modélisation de l'impact de la géométrie du roulement

Le modèle thermique, couplé au modèle Harris-Palmgren ajusté, est maintenant utilisé pour étudier l'impact de la géométrie sur la production de chaleur des roulements. Le roulement B, 40% plus large que le roulement A, produit 25% de pertes en plus. Le modèle Harris-Palmgren considère le diamètre moyen à la puissance trois. Il en résulte que le paramètre f_0 double du roulement B au roulement A. Le comportement thermique des roulements est comparé pour justifier, ou non, d'une telle différence. L'enjeu est d'obtenir un modèle universel, pouvant prédire les pertes thermiques des roulements sans les tester au préalable.

Les deux roulements sont modélisés thermiquement, pour une température d'injection de 60°C et un débit d'huile de 15 L/h. Si un unique paramètre f_0 est employé pour les deux roulements dans le calcul Harris-Palmgren, il en résulte que le roulement B produit environ deux fois plus de pertes que le roulement A. Si les deux paramètres mesurés sont employés, il en résulte que le roulement B produit environ 25% plus de chaleur que le roulement A, ce qui est conforme à l'expérience. Il n'y a pas de différence notable du comportement thermique des roulements, notamment parce que les coefficients de répartition des flux sont similaires. Le comportement thermique des deux roulements ne justifie donc pas à justifier l'emploi de coefficients différents dans les modèles de pertes. La prise en compte de la géométrie dans ses modèles doit donc être investiguée.

La prise en compte de la géométrie dans le modèle Harris-Palmgren est insatisfaisante pour deux raisons : d'une part, le cube du diamètre dans la formulation de la perte indépendante de la charge est trop important. D'autre part parce que deux roulements ayant des éléments roulants différents en taille et en nombre, produisent la même perte de chaleur selon ce modèle. Afin d'étudier l'impact de la géométrie sur la contribution indépendante de la charge, la formulation de la résistance au roulement elasto-hydrodynamique (équation *(0.13)*) est généralisée du contact à l'intégralité du roulement. Il en ressort une relation de proportionnalité qui permet d'intégrer le nombre d'éléments roulants et leur taille à la contribution indépendante de la charge dans l'équation (3.34) :

$$M_{0_{new}} = f_0 \cdot 4.5 \cdot 10^3 \cdot (v_{oil} \cdot \omega_i)^{0.66} \cdot \gamma^* \cdot d_m^{1.66} \cdot Z \cdot D^{1.34} \quad (0.13)$$

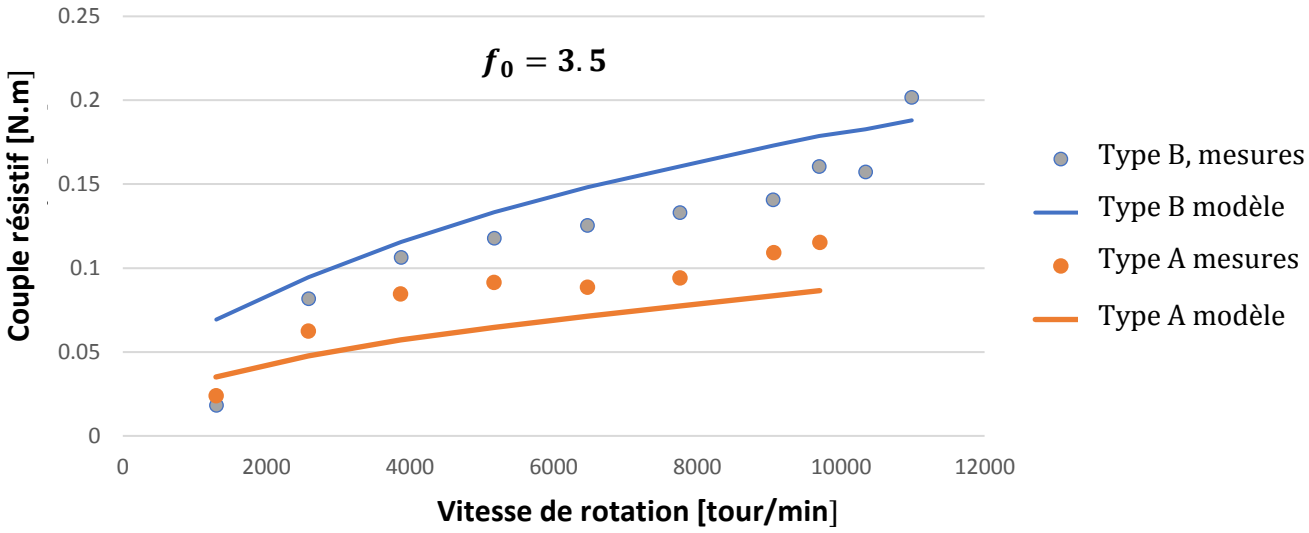

Figure 0.12 : Comparaison entre mesures et les prédictions du nouveau modèle pour les deux roulements testés.

Ce nouveau modèle pour la contribution indépendante de la charge est présenté sur la Figure 0.12. Le nouveau modèle ne permet pas de coller parfaitement aux mesures des deux roulements. L'erreur maximale est de l'ordre de 20%. Il permet néanmoins d'intégrer des paramètres géométriques plus fins que le modèle original et de n'utiliser qu'un seul coefficient empirique. Un travail de comparaison entre ce modèle et le modèle SKF a été réalisé sur dix-huit roulements issus du catalogue afin de comparer leur prise en compte de la géométrie. Il en résulte que le modèle SKF, via des paramètres dépendants de la série du roulement concerné, intègre d'une manière similaire la géométrie. L'intérêt du nouveau modèle, comparé au modèle SKF, est qu'il peut être appliqué à des roulements hors-catalogue, comme les roulements aéronautiques par exemple.

1.4 Conclusion générale

En conclusion, le roulement hydrodynamique et le cisaillement dû au glissement sont les deux principaux pôles de pertes des roulements opérant en dessous du seuil de haute vitesse (> 1M NdM). Le roulement hydrodynamique dépend de la charge et est proportionnel au produit vitesse de rotation par la viscosité à la puissance deux-tiers. Le cisaillement de glissement n'est pas calculable sans un procédé itératif.

Les deux modèles globaux utilisés par l'industrie sont simples à mettre en œuvre et s'appliquent à tous types de roulements. Le modèle Harris-Palmgren sépare la perte de puissance en deux entités indépendamment mesurées. Le modèle SKF conserve les pôles de pertes cités ci-dessus et en donne une formulation analytique.

Pour conclure, les deux modèles ont été comparés à de nouveaux résultats expérimentaux sur le couple résistif des roulements à bille à gorge profonde. Avec quelques modifications, les deux modèles ont pu prédire les pertes de puissance mesurées. L'impact de la vitesse de rotation, de la charge et de la température sont bien

pris en compte dans les modèles. En revanche, la comparaison entre les deux roulements laisse suggérer qu'il faille recaler les modèles sur chaque roulement. De plus, aucun des modèles ne prend en compte le débit d'injection, qui a un impact sur le couple résistif à certaines températures d'injection.

Un modèle thermique du banc a été développé et validé sur des expériences dédiées. La prise en compte du coefficient de pénétration et de la fraction d'huile est primordiale à la modélisation thermique du roulement. Le coefficient de pénétration a été mesuré pour différents débits d'injection et différentes vitesses de rotation. La formulation de la fraction d'huile a été modifiée pour être appliquée dans le cadre de la lubrification par jet d'huile. Le modèle a été validé, notamment par des essais où la température de la bague intérieure du roulement est mesurée. Ce modèle a ensuite été utilisé en tandem avec le modèle Harris-Palmgren précédemment ajusté afin d'étudier l'influence de la lubrification et de la géométrie du roulement sur la perte de puissance. Le rôle thermique de la lubrification et l'interdépendance entre débits d'huile et températures d'injection ont été comparés à l'expérience. Il en ressort que le modèle permet de mieux comprendre comment le débit d'huile impacte le couple résistif *via* des phénomènes thermiques. En revanche, l'impact de la géométrie sur le comportement du roulement ne semble pas être dû à des phénomènes thermiques. Une nouvelle formulation de la contribution indépendante de la charge, développée depuis la formulation analytique du roulement hydrodynamique, est proposée. Cette formulation offre de meilleurs résultats que le modèle Harris-Palmgren puisqu'un seul coefficient est suffisant pour prédire la perte de puissance du roulement à 20% près. La formulation proposée intègre la géométrie du roulement d'une manière similaire à celle du modèle SKF, en utilisant non pas des coefficients issus du catalogue, mais des informations fines de la géométrie du roulement.

Nomenclature

Latin symbols

A	*Surface*	$[m^2]$
a	*Contact ellipse semi-major axis*	$[m]$
B	*REB width*	$[m]$
b	*Contact ellipse semi-minor axis*	$[m]$
D	*Rolling elements diameter*	$[m]$
C_0	*Static load capacity*	$[N]$
C_D	*Drag coefficient*	$[]$
C_P	*Iso pressure Caloric capacity*	$[J \cdot Kg^{-1} \cdot K^{-1}]$
d	*Diameter*	$[m]$
$\dot{D}$	*Volumetric oil flow rate*	$[m^3 \cdot s^{-1}]$
E'	*Equivalent Young modulus*	$[Pa]$
F	*Force*	$[N]$
F_N	*Normal Force*	$[N]$
F_R	*Applied Radial Force*	$[N]$
F_β	*Applied Equivalent Force*	$[N]$
F_S	*Applied Equivalent Static Force*	$[N]$
F_D	*Drag Force*	$[N]$
F_P	*Pressure Force*	$[N]$
F_C	*Cage Force*	$[N]$
f_0	*Harris-Palmgren model load-independent parameter*	$[\,]$
ft	*SKF model splash lubrication parameter*	$[\,]$
G	*Classical dimensionless material parameter* $= \alpha \cdot E'$	$[\,]$
G_{rr}	*SKF model rolling contribution load function*	$[\,]$
G_{sl}	*SKF model sliding contribution load function*	$[\,]$
G_r	*Grashof number*	$[\,]$
h_c^*	*Theoretical central oil film thickness*	$[m]$
h_c	*Reduced central oil film thickness*	$[m]$
I	*Thermal Inertia*	$[J \cdot K^{-1}]$
K_{rs}	*SKF model replenishment/starvation constant*	$[\,]$
K_z	*SKF model bearing type related geometric constant*	$[\,]$
K_{Ball}	*SKF model ball bearing geometric constant*	$[\,]$
k	*Thermal conductivity*	$[W \cdot m^{-1} \cdot K^{-1}]$
L	*Characteristic length*	$[m]$
M_C	*Cage resistive torque*	$[N \cdot m]$
M_{HPM}	*Harris Palmgren model for resistive torque*	$[N \cdot m]$
M_0	*Harris Palmgren model load-independent contribution*	$[N \cdot m]$
M_1	*Harris Palmgren model load-dependent contribution*	$[N \cdot m]$
M_{SKF}	*SKF model for resistive torque*	$[N \cdot m]$
M_{rr}	*SKF model rolling contribution*	$[N \cdot m]$
M_{sl}	*SKF model sliding contribution*	$[N \cdot m]$
M_{drag}	*SKF model drag contribution*	$[N \cdot m]$
M_{splash}	*SKF model splash lubrication contribution*	$[N \cdot m]$
$\overline{M_{adapted}}$	*Adapted Resistive torque*	$[N \cdot m^{-1/3} \cdot s^{2/3}]$
m	*Inlet meniscus distance*	$[m]$
m^*	*Theoretical fully flooded inlet meniscus distance*	$[m]$
m	*Mass*	$[Kg]$
N	*Shaft speed*	$[rpm]$
Nu	*Nusselt number*	$[\,]$
P	*Pressure field*	$[Pa]$

P	*Heat production*	*[W]*
Pr	*Prandlt number*	*[ ]*
P_{max}	*Pressure field maxima*	*[Pa]*
Q_A	*Rolling element normal load*	*[N]*
$Q_{mist\_outlets}$	*Heat exchanged between oil mist and oil outlets*	*[W]*
$Q_{OR\_housing}$	*Heat exchanged between outer ring and housing*	*[W]*
$Q_{IR\_housing}$	*Heat exchanged between inner ring and shaft*	*[W]*
Q_T	*Brinkman number*	*[ ]*
q	*Oil-air mixture quality*	*[ ]*
R	*Thermal resistance*	*[K·W^{-1}]*
R_x	*Equivalent radius in the direction of rolling*	*[m]*
R_1	*SKF model geometric constant for the rolling contribution*	*[ ]*
Re	*Reynolds number*	*[ ]*
R_s	*SKF model splash lubricated projection function*	*[ ]*
S	*Cross-sectioned surface*	*[m^2]*
S_P	*Projected surface*	*[m^2]*
S_1	*SKF model geometric constant for the sliding contribution*	*[ ]*
T_R	*Rolling traction force*	*[N]*
T_S	*Sliding traction force*	*[N]*
U	*Classical dimensionless speed parameter* $= \frac{V_R \cdot \mu}{R_x \cdot E'}$	*[ ]*
V	*volume*	*[m^3]*
V_g	*Sliding linear speed*	*[m·s^{-1}]*
V_R	*Rolling linear speed*	*[m·s^{-1}]*
V_o	*Orbital linear speed*	*[m·s^{-1}]*
V_m	*SKF model drag function*	*[ ]*
W	*Classical dimensionless load parameter* $= \frac{Q_A}{R_x^2 \cdot E'}$	*[ ]*
x	*Axis of rolling motion*	
y	*Axis transverse to rolling motion*	
y	*Harris-Palmgren load-dependent contribution parameter*	*[ ]*
Z	*Rolling element number*	*[ ]*
z	*Harris-Palmgren load-dependent contribution parameter*	*[ ]*

Greek symbols

α	*Penetration ratio*	*[ ]*
α_0	*Original contact angle*	*[rad]*
Γ	*Ratio of resistive torque*	*[ ]*
γ	*Geometrical ratio*	*[ ]*
$\Delta\omega$	*Rotational speed difference*	*[rad·s^{-1}]*
δ	*Load reaction displacement*	*[m]*
δF	*Elemental force*	*[N·m^{-2}]*
ε	*Diametral clearance*	*[m]*
κ	*Ellipse ellipticity*	*[ ]*
Λ	*Tallian number*	*[ ]*
μ	*Dynamic viscosity*	*[Pa·s]*
μ_{EHL}	*SKF model sliding contribution EHL regime constant*	*[ ]*
μbl	*SKF model sliding contribution limit regime constant*	*[ ]*
ν	*Kinematic viscosity*	*[m^2·s^{-1}]*
ρ	*Density*	*[Kg·m^{-3}]*
σ	*Stephan-Boltzmann constant*	*[W·m^{-2}·K^{-4}]*
τ_0	*Newtonian shear stress*	*[Pa]*
τ_{lim}	*Limiting shear stress*	*[Pa]*
φ_T	*Film thickness thermal reduction factor*	*[ ]*
φ_A	*Film thickness starvation reduction factor*	*[ ]*

φ_{bl}	*SKF model sliding contribution regime partition function*	*[ ]*
φ_{rs}	*SKF model rolling contribution replenishment factor*	*[ ]*
φ_{ish}	*SKF model rolling contribution thermal factor*	*[ ]*
χ	*Thermal diffusivity*	*[W·s$^{1/2}$·m^{-2}·K^{-1}}]*
ω	*Rotational speed*	*[rad·s^{-1}]*

Subscripts

e	*Outer ring*
i	*Inner ring*
ge	*Outer ring groove*
gi	*Outer ring groove*
ext	*External*
int	*Internal*
m	*Orbital*
r	*Radial*
R	*Rolling element*
j	*j^{th} rolling element*
k	*k^{th} rolling element*
air	*Pure air property*
oil	*Pure oil property*
$mist$	*Equivalent oil-air mixture property*
$wall$	*Equivalent oil-air mixture property at the solid temperature*
$material$	*Solid material property*
$conduction$	*Conductive heat transfer*
$convection$	*Convective heat transfer*
$radiation$	*Irradiative heat transfer*
$striction$	*Heat transfer through a restriction*
$transport$	*Heat transfer through transport*
$threshold$	*Applied with a threshold*
$total$	*Total*
$Tore$	*Toric*
$Disks$	*Disk*
$Ball$	*From ball element*
$measures$	*Relative to measurements*
$single$	*Relative to a single f_O parameter*
$different$	*Relative to different f_O parameters*

Table of Contents

Acknowledgements 5
Abstract 7
Résumé 9
Résumé étendu 11
1.1 Les pertes de chaleur dans le roulement 12
1.2 Investigations expérimentales 16
1.3 Modélisation thermique 21
1.4 Conclusion générale 28
Nomenclature 31
Table of Contents 35
Introduction 37
1. Friction in Rolling Element Bearings 41
1.5 Introduction 42
1.6 About Rolling Element Bearings 42
1.7 Sources of friction 46
1.8 Global Power Loss Models 54
1.9 Conclusion 59
2. Empirical Investigation 61
2.1 Introduction 62
2.2 Experimental test rig 62
2.3 Calibration phase 64
2.4 The Harris-Palmgren model: results and discussion 66
2.5 The SKF Model: results and discussion 79
2.6 Conclusion and discussion 86
3. Thermal Model 89
3.1 Introduction 90
3.2 Lubrication 90
3.3 Thermal Network 92
3.4 Test Rig Thermal Network Analysis 94

3.5 REB thermal model results and discussion....105
3.6 Conclusion....114
Conclusion 115
Appendix 121
Appendix A: Theoretical speeds....122
Appendix B: Sliding mechanisms....123
Appendix C: Quasi-static Equilibrium....127
Appendix D: REB motion equilibrium without centrifugal forces....130
Annex E: REB equilibrium scheme....131
Annex F: Thin Efficiency Resistance Calculus....132
Appendix G: Rolling Analytical formulation....133
Bibliography 139

Introduction

Transmission systems aim at adapting rotational speeds torques and direction for any application. Gears are the most common solution to do so. A pair of gears transmits a torque in the form of a lever arm force. The pressure angle induces a resultant force back to the shaft. Bearings are required to support this load and to ensure the proper rotation of the rotating parts. Avoiding sliding between surfaces is vital in order to prevent excessive heat production, avoidable wear and potential damages. The addition of rolling elements between the rotating parts thus leads to the development of Rolling Element Bearing (REB). Whether composed of ball, roller or needle, REBs have become a critical component of transmissions systems.

Weight reduction and compactness have become major requirements over the years for the transport industry. Improvements in material properties have enable higher loadings and higher fatigue life expectancies for ever smaller components. The evolution of helicopter transmission systems is following the same trend. For instance, some helicopter manufacturers use REBs with the inner raceway integrated into the shaft. On the epicyclic trains, the outer ring disappears, and the satellite gear incorporates the raceway for the rolling elements. On Figure I.1, a 3D replica of the Super Puma main gearbox provides insights of such a density of mechanical components.

Figure I.1 : Scheme of a Helicopter main gear box and its components [21]

With the increase of transmitted loads in a closer space, heat productions generated within the transmission system are harder to evacuate. Although REBs have been called frictionless bearings, they also produce a non-negligible amount of heat due to friction phenomena. At low transmitted torque, it can represent 80 % of the transmission total power losses. When the transmitted torque reaches full capacity, it diminishes to 20 %, the gear contacts then producing most of the heat [1]. In the real-flight situation, the transmitted torque varies, and the REB heat production fluctuates between these two values. Heat productions lead to temperature increases and should carefully be evacuated from the transmission system.

On helicopter main gearboxes, heat is mainly removed by the lubricant circulating through cooling systems. The lubrication design is a critical cornerstone of helicopter development. The heat production is calculated for each component in order to adjust the required oil flow rate. Due to complex design, the oil pathway is not trivial as it can go through multiple intermediaries before exiting the system. As an example, a secondary cooling system is presented on Figure I.2**Erreur ! Source du renvoi introuvable.**

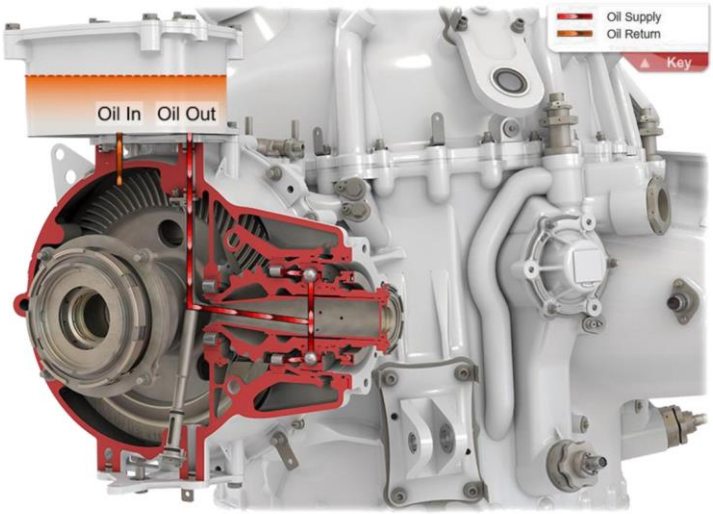

Figure I.2: Cross-sectioned view of a Helicopter gear box cooling system [22]

The proximity of REBs to the gears increases the thermal dependency to one another. The heat produced by the gear contact is not entirely evacuated through the oil, and some of it find its way through the shaft to the REBs. In some loss of oil conditions, the REB can become the hottest part of the transmission system [2]. Comprehension of how the REBs produce heat and exchange it within the transmission system is essential therefore to master the thermal behaviour of a given gearbox. In that optic, the helicopter gearbox complexity imposes the use of an effective tool, applicable to each REB, in order to calculate heat production.

In order to do so, one must first understand the mechanisms of REB friction. The first chapter concerns the prediction of REB heat production. After analysing bibliographical contents on local heat phenomena, two existing global power loss models will be presented.

The second chapter provides new empirical investigations on REB heat production. A test rig dedicated to REB thermal analysis is presented. The influence of some parameters such as shaft speed, load, REB geometry and lubrication designs are assessed. The global models are adjusted to the experimental data and a discussion about their adaptability is given.

The third chapter focuses on modelling the thermal behaviour of REBs. A thermal model of one of the tested REB is developed. Dedicated experiments on the test rig enable comparisons between modelled and measured temperature evolutions. Afterwards, the previously adjusted power loss model is associated with the thermal model in order to analyse the influence of lubrication design and of REB geometry on thermal behaviour.

Chapter 1:
Friction in Rolling Element Bearings

1.5 Introduction

The study of Rolling Element Bearing heat production is a complex multilevel discipline. The contact between two lubricated surfaces is a subject of research on its own. The dynamics of Rolling Element Bearing are another one. REB manufacturers have developed dense numerical tools over the years in order to model REB behaviour. The complexity of these tools often prohibits their use in larger simulations, for instance in the thermal simulation of an entire gearbox. A simulation of this nature requires the use of a simpler REB model, avoiding any additional iterative calculation for instance. Yet, to assess to accuracy of such a model, the friction mechanisms occurring within a REB should be closely examined.

The first part of this chapter presents an overview of REB characteristics and performances. The lubrication regime between two lubricated surfaces is introduced afterwards.

The second part of this chapter focuses on the friction mechanisms occurring within REBs. Three main contributions are presented in light of the literature. A discussion is presented on whether or not they should be included in the scope of this study.

The last part presents two existing REB power loss models. Their simplicity and promptness of use have made them important tools in engineering development.

Finally, a conclusion on the use of such global models is assessed in light of the friction mechanisms previously presented and of empirical analysis from literature.

1.6 About Rolling Element Bearings

1.6.1 Geometrical Features

Several types of REBs have been developed over the years to maximize life expectancies in line of their applications. The choice of one REB against another is made with respect to admissible loadings, speeds, cost, compactness, vibrations and lubrication methods.

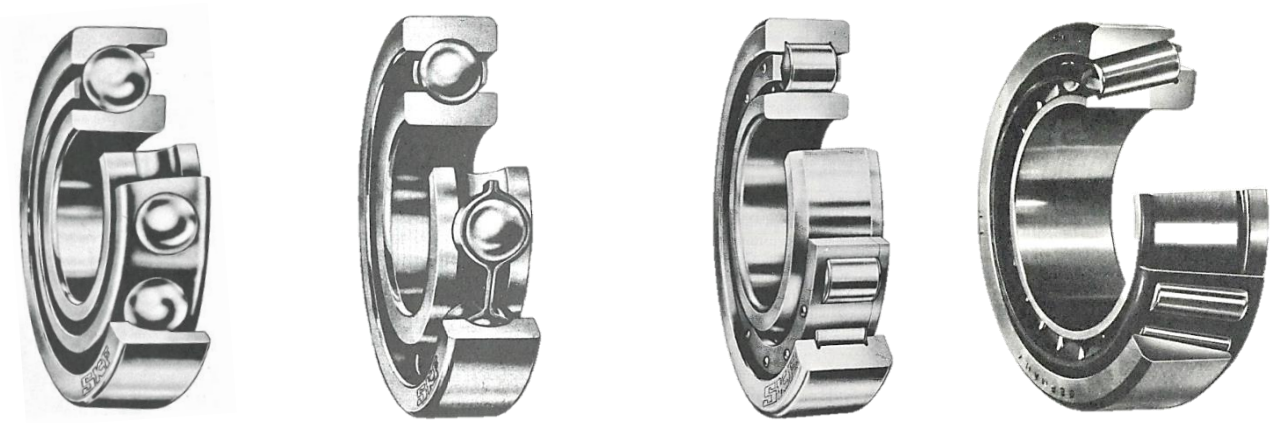

Angular Ball Bearing ***Deep Groove Ball Bearing*** ***Radial Roller Bearing*** ***Tapered Roller Bearing***

Figure 1.1: Photographs of partially cross-sectioned rolling element bearings [10]

On Figure 1.1, different REBs are presented in partially cross-sectioned views. Deep groove ball bearings are widely used in the transport industry. Their compactness and adaptability to both radial and axial loads ease their use. This type of REB has therefore been incorporated in the test rig that will be presented in the second chapter of this study.

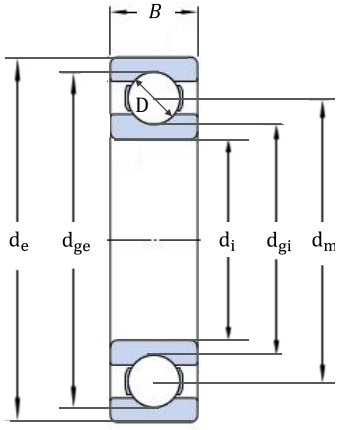

Name	Designation
Inner Ring Diameter	d_i
Inner Ring Groove Diameter	d_{gi}
Outer Ring Diameter	d_e
Outer Ring Groove Diameter	d_{ge}
Bore Diameter	d_m
Ball Diameter	D
Number of Balls	Z

Figure 1.2 : Geometrical characteristics of a deep groove ball bearing

The main characteristics of deep groove ball bearing are presented in Figure 1.2. The bore diameter is defined as the averaged ring groove diameter but can also be accessed with the averaged ring diameter. Most bearing manufacturers do not specify neither the rolling element diameter, nor the number of rolling elements. These geometrical features are extremely important in the REB analysis. Niel has proposed a method in order to calculate them using online calculator [4]. Another interesting parameter is the geometrical ratio γ found in equation (1.1).

$$\gamma = \frac{\cos\alpha \cdot D}{d_m} \qquad (1.1)$$

In the case of deep groove ball bearing, the contact angle α is equal to zero and the geometrical ratio is the ball diameter divided by the bore diameter. This ratio appears in every aspect of REB analysis, from the calculation of the relative motion to the calculation of equivalent contact radii.

1.6.2 Speeds, Deformations and Equilibrium

In order to analyse the REB heat productions and heat transfer mechanisms, some information on the REB mechanisms are required. The cage and rolling element rotations must be taken into account in order to estimate linear speed vectors. Rolling without sliding is a common assumption in order to calculate the REB theoretical speeds. Appendix A presents these features. Yet, sliding can occur within REBs. Depending on operating conditions, either the inner ring, the outer ring, or both are undergoing some sliding. The study of sliding is important has it implies some heat productions. These considerations are presented in Appendix B. The contacts between the rolling elements and the rings are computed to estimate contact ellipses. The deformations of the rolling elements and of the rings are estimated by Hertz theory presented in Appendix C. The study of rolling element bearing equilibrium is complex for two reasons. Firstly, each rolling element has its own equilibrium, which implies its deformation under loads and its rolling and orbiting motions around the REB axis. Secondly, the behaviour of one rolling element influences every other rolling element. Indeed, the load is distributed among them and the cage interlinks them altogether. This two-scale equilibrium finds solution mainly through iterative approaches. Assuming no interaction between loading and motion equilibriums leads to the quasi-static approach, also presented in Appendix D.

At high speed, the centrifugal force unbalances the force equilibrium between the inner ring and outer ring. If the $N \cdot d_m$product (REB bore diameter in millimetre multiplied by shaft speed in rpm) is over a million, the centrifugal force is no longer neglected, and a more complex motion equilibrium is required. Appendix E presents different REB motion equilibrium schemes to estimate the sliding speeds depending on whether centrifugal forces are considered or not.

In helicopters gearboxes, the $N \cdot d_m$product barely exceeds 0.8 million, except for the engine outputs (if the engine manufacturer has not provided the first stage of reduction). Therefore, centrifugal forces can be neglected, and the contact angles are assumed to be constant for both rings.

1.6.3 EHL contact theory

Depending on the operating conditions, different lubrication regimes can be observed in the contact between two solids. Stribeck first described the evolution of contact mechanism *versus* a unique parameter[23]. The Tallian number Λ, which is defined as the ratio of the film thickness divided the surface rugosity can also be used. This leads to the renowned Stribeck Curve shown in Figure 1.3.

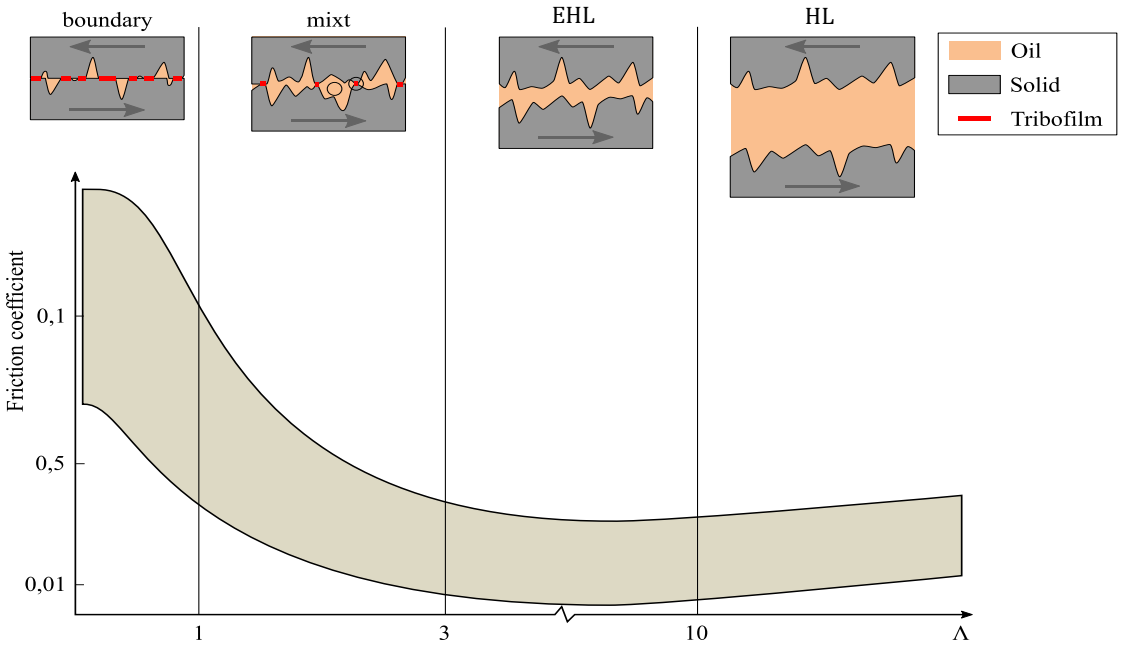

Figure 1.3 : Lubrication regime depending on the Tallian number

The applied load tends to bring the surface closer whereas, depending on the rolling speed and on the fluid viscosity, a hydrodynamic pressure arises in the contact enabling the separation of the surfaces. As the film thickness increases, the surfaces can be fully separated and an increase in rolling speed or in fluid viscosity will result in additional lubricant shearing, which in turn increases the coefficient of friction. The regimes can therefore vary, from the boundary regime where the contacts between surface asperities are prominent to mixed regime where a certain proportion of lift is achieved by the lubricant, and then to the full-film regime. If the pressure within the contact is high enough, the solids in contact will elastically deform. This transition differentiates the hydrodynamic regime (HL) from the elasto-hydrodynamic regime (EHL).

In 1966, Hamrock and Dawson established a formula for linear contact film thickness from numerical computation using three dimensionless parameters [24]. Later on, Dawson and Higginson depicted similar formulae for elliptical contact film thickness (equation *(1.2)*).

$$h_{c^*} = 1.691 \cdot R_x \cdot U^{0.67} \cdot G^{0.53} \cdot W^{-0.067} \cdot (1 - 0.61 \cdot e^{-0.73\kappa}) \qquad (1.2)$$

U, G and W are respectively the speed, pressure and loading dimensionless classical parameters and κ the ellipticity of the contact.

Cheng then proposed a reduction coefficient φ_T for the film thickness to take into account the increase in film temperature due to the inlet shearing [25] which is detailed in equation *(1.3)*.

$$\varphi_T = \frac{1 - 13.2 \cdot \frac{P_{max}}{E'} \cdot Q_t^{0.42}}{1 + 0.213 \cdot \left(1 + 2.23 \cdot \left(\frac{V_g}{V_R}\right)^{0.83}\right) \cdot Q_t^{0.64}} \quad (1.3)$$

In this equation, P_{max} is the maximum Hertzian pressure, E' is the equivalent Young's modulus, Q_t is the Brinkman number, V_g and V_R respectively the sliding and rolling speed. Details of the calculation are found in [26].

Other formulae for the film thickness have been established over the year, the work of Moes, using different parameters can be noted [27]. The above-mentioned formulae for film thickness considered a fully flooded contact, where the integration domain is infinite. In fact, depending on conditions, the amount of lubricant at the inlet is finite, and in drastic conditions, the contact can even be starved from lubrication. Another reduction coefficient φ_A is therefore added to the film thickness formula. Wedeven observed that the reduction in film thickness is linked to the distance from the inlet meniscus location [28]. Hamrock and Dowson proposed a formula to estimate the contact starvation level based upon the inlet meniscus distance m in equation (1.4) [29].

$$\varphi_A = \left(\frac{m - 1}{m^* - 1}\right)^{0.25} \quad (1.4)$$

m^* is the critical inlet meniscus parameter that depends on operative conditions. Chiu considered the replenishment is a mechanism due to the two half-film heights being brought to the contact by the two bodies [30]. Different works have been treating starved lubrication in order to compute the inlet meniscus distance [31,32],[33]. Other works depicted the lateral replenishment from the lubricant trail back to the race as a relaxation mechanism in order to compute the meniscus distance [34], [35]. Other pointed out that the relaxation time from lateral replenishment far outreached the frequency of passage of rolling elements [33]. Finally, both reduction factors are used to reduce the theoretical film thickness in equation *(1.5)*.

$$h_c = \varphi_T \cdot \varphi_A \cdot h_{c^*} \quad (1.5)$$

In helicopter transmissions, REBs operate with linear speed from 3 to 50 m/s. The generated film thickness can vary greatly from the large low-speed REBs that carry the rotor shaft to the small high-speed REBs, closer to the engines. Because of the high-quality superfinishing of the REB surfaces, their rugosity is genuinely small. The lubrication regime varies from the mixt regime to the full hydrodynamical regime.

1.7 Sources of friction

In most modern transmission system, the efficiency reaches 98%. The remaining 2% of transmitted energy is dissipated as heat. Indeed, applying the first principle of

thermodynamics implies that all the energy brought to a steady state system should be somewhat extracted from the system. If vibrations could be considered as an energy sink, its low-energy state often makes it negligible compared to heat production. The heat production is generated by friction and has been thoroughly investigated over the past decades. Friction happens at any interactions between two systems (solid or fluid) in relative motion.

In rolling element bearing, friction occurs at the contacts between raceways and rolling elements, the contact between the cage pocket and the elements, the interaction between the raceways and the cage and finally the interaction between the elements, the cage, the rings and the fluid within the bearing chamber. The contacts between raceways and rolling elements are the most heavily charged, with complex friction mechanisms. In order to understand local frictions mechanisms in REBs, a review of the literature is presented.

1.7.1 Rolling Friction

Does no-slip lubricated contact produce a non-negligible amount of heat? In a dry contact, the hysteresis of the elastic deformation can produce some heat; the train rail-wheel contact is a perfect example of it. Additionally, some studies have considered that some micro-slip occurs in any contact, either due to curvature deformation or to stick-slip phenomena [36]. Whether the heat production resulting from these micro sliding should be included in dry rolling or not is unclear. In any case, in most gear study, dry rolling is neglected compared to the macro sliding contribution to the total power losses [37]. In rolling element bearing, this dry rolling have either been neglected [10,38,39], or considered [40]. An empirical formula has been empirically measured at low speed and low load conditions [41].

$$M_h = 7.48 \cdot 10^{-7} \cdot \frac{D}{2}^{0.33} \cdot Q_A^{1.33} \cdot (1 - 3.519 \cdot 10^{-3} \cdot (k-1)^{0.8063}) \qquad (1.6)$$

In Equation *(1.6)*, the resulting hysteresis moment is presented, depending on the ball diameter D, the normal load Q_A and the ellipticity k.

In a lubricated contact, hydrodynamic and elasto-hydrodynamic rolling are phenomena resulting from the asymmetry of the lubricated contact pressure distribution. Indeed, between two lubricated solids in rotation, a meniscus of lubricant is formed at the contact inlet, enabling a slow increase in pressure due to Poiseuille's flow which will eventually lift the surfaces and generate a film thickness.

The rolling friction have been thoroughly studied over the last 50 years, yet there are some discrepancies on whether to include it in REB calculation or not. On Figure 1.4, three ways of considering rolling friction are presented.

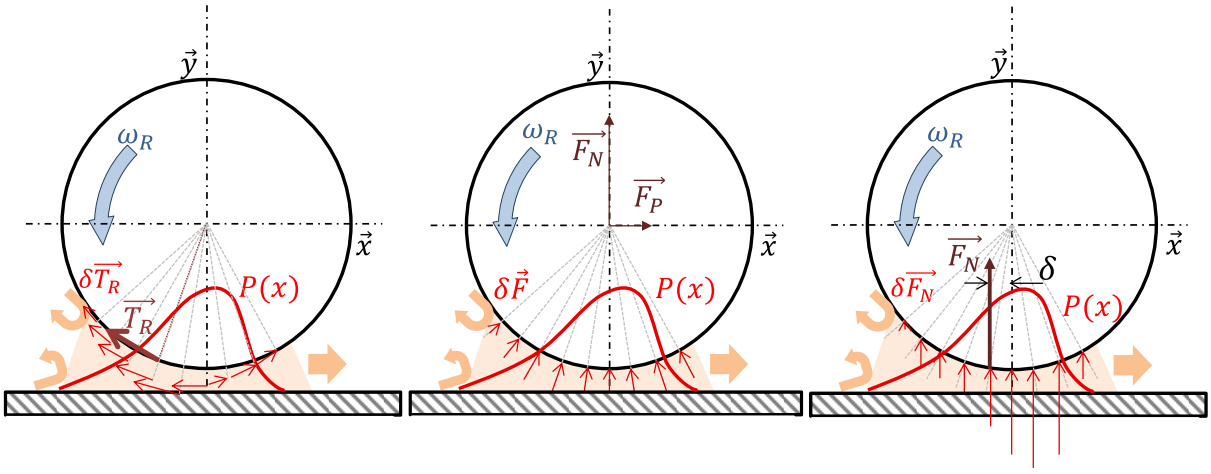

a. Rolling traction force ***b. Pressure forces*** ***c. Load reaction center displacement***

Figure 1.4: Comparisons of the hydrodynamical rolling phenomena

The rolling resistance can be represented as infinitesimal tangent forces $\delta\overrightarrow{T_R}$ opposed to the motion and proportional to the pressure gradient. The integration over the contact then yields a rolling traction force $\overrightarrow{T_R}$ as presented in Figure 1.4.a. The pressure action can also be considered as a sum of infinitesimal pressure forces perpendicular to the surface $\delta\vec{F}$. The total pressure force, applied to the body centers, is then decomposed in two orthogonal vectors: $\overrightarrow{F_N}$ and $\overrightarrow{F_P}$, when $\overrightarrow{F_N}$ is the reaction vector that equals the contact load $\overrightarrow{Q_A}$ and $\overrightarrow{F_P}$ is the pressure force in the direction of rolling, referred as rolling pressure force, as seen in Figure 1.4.b. From another viewpoint, the vertical infinitesimal pressure forces can also be added up to form the reaction vector $\overrightarrow{F_N}$, with an offset δ resulting from the dissymmetry of the pressure field (Figure 1.4.c.). This rolling load reaction displacement will result in a braking moment opposed to the rolling motion. In the past, these three viewpoints were either considered separatly or simutanuesly.

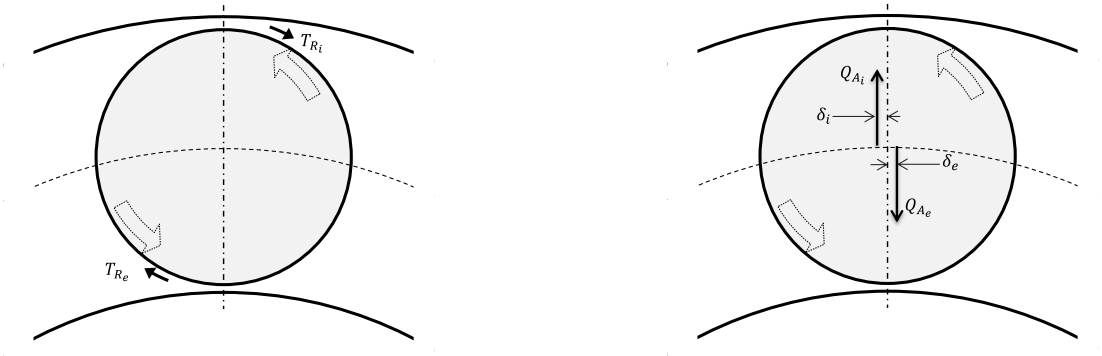

a. Traction force scheme [42,43] ***c. Load displacement scheme*** [3]

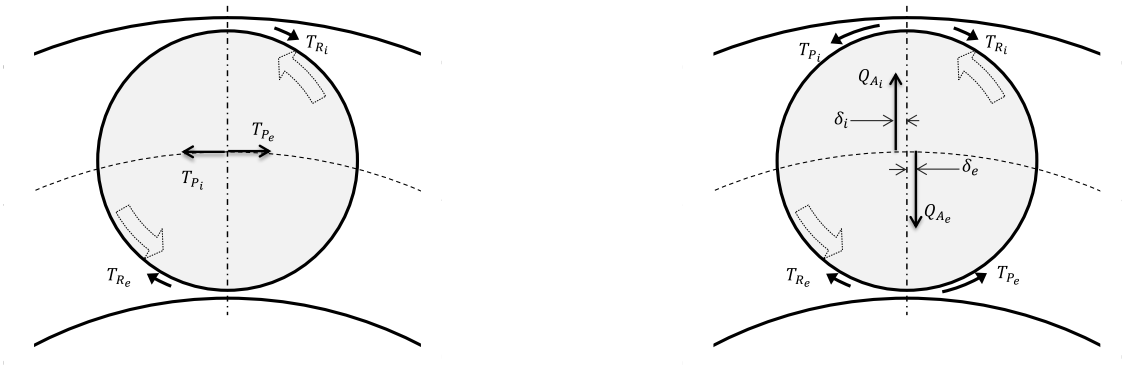

b. Combined traction and pressure force scheme [24]

d. Exhaustif Scheme [40,44–48]

Figure 1.5 : Comparison of the different viewpoints on the rolling phenomenon

Crook studied the rolling and sliding friction on a four disk machine, where the central disk is either free of rotation, or decelerated by a braking moment imposing a certain amount of sliding over the contacts with the three other disks[42]. He concluded that the rolling friction is independent of the sliding speed and acts as a traction force that competes with the sliding force to reach the disk equilibrium. His work therefore leads to apply only a rolling traction force to both to the inner and outer contacts of a ball element bearing as presented on Figure 1.5.a. Townsend studied a cageless angular ball bearing and similarly considered only rolling traction forces [43].

Later on, Dowson and Higginson, using their analytical model for the film thickness, resolved the pressure times film thickness gradient integral to compute the rolling traction force [49]. The rolling pressure force is also considered as presented in Figure 1.5.b. It can be shown analytically that the rolling pressure force is proportional to the rolling traction force as seen in equation *(1.7)*. More precisely, the rolling pressure force is nearly two times the rolling traction force but opposite in direction. This force should be applied to the solid centers of motion and therefore does not contribute in generating power losses.

$$\overrightarrow{F_P} = -2 \cdot \frac{d_g}{d_g + D} \cdot \overrightarrow{T_r} \qquad (1.7)$$

In 1979, Tevaarweck, citing a private correspondence with Dawson, disclosed a ground-braking formula for the rolling friction in the form of a load reaction center displacement [3]. This approach applied to REBs is presented in Figure 1.5.c. and the formula is detailed in equation *(1.8)* using classical dimensionless elasto-hydrodynamic parameters.

$$\delta = 4.25 \cdot a \cdot G^{0.022} \cdot U^{0.66} \cdot W^{-0.87} \qquad (1.8)$$

Houpert, citing Tevaarweck, depicted this formulae with classical dimensionless elasto-hydrodynamic parameters, although Houpert used it simultaneously as a rolling traction force and a load reaction center displacement.

$$T_{r_*} = 2.86 \cdot E' \cdot R_{x_*}^2 \cdot G^{0.022} \cdot U^{0.66} \cdot W^{0.47} \cdot k_*^{0.348} \qquad (1.9)$$

Houpert also considered a rolling pressure force [36,50]. He applied the pressure force at the contact this time, which results in an accelerating moment that counteracts the braking moment resulting from the offset of the load center. This exhaustive approach of the ball equilibrium is presented in Figure 1.5.d. In 1991, Zhou established a similar calculation for tapered roller bearing torque prediction including elasto-hydrodynamic rolling traction force, pressure force and load offset [46].

Biboulet contributed to the study of rolling friction by focusing on the inlet integral domain for both linear and elliptical contact. He then used his integral domain to elaborate a smooth transition from iso-viscous rigid to elasto-hydrodynamical regime[48].

The previously mentioned analytical integration considered a fully flooded contact. Some research suggest that REB contacts are in fact partially starved [32,51]. The rolling traction force should therefore be reduced by the same starvation factor as for the oil film thickness in Equation *(1.4)* [35]. Yet, the difficulty of measuring meniscus distance prohibits an universal formulation for the starvation factor, even more so in a complex environment such as Rolling Element Bearings.

To conclude, rolling friction has raised some questions over the years. Different contributions have been used to investigate rolling friction in rolling element bearing. The most recent works considered the exhaustive scheme where all three contributions (rolling traction force, rolling pressure force and load reaction center displacement) are considered for the ball equilibrium. The resulting rolling heat production on the other hand has not reached consensus. Should it be calculated from the three contributions ? Some rolling element software does not seem to include it [5,52] although it appears not negligible.

1.7.2 Churning and drag

Any solid moving through a medium will imply friction. This friction is caused by the fluid viscous and pressure actions on the solid. In REB analyses, the resulting power losses have been referred as churning or drag over the years, although the author argues that churning is a viscous phenomenon whereas drag is pressure related. Because of the complexity of fluid motions within REBs, different fluid-solid interactions are presented. Some analytical formulations of these phenomena are discussed. The outcomes of recent CFD analysis are also presented.

Depending on how the fluid flows around solids, the pressure and speed distribution change. The flow will induce a drag force, a lift force and a moment force on the solid depending on these distributions. Van Karman disclosed that the aerodynamical

drag can be calculated from a drag coefficient C_D and a projected surface S_p seen in equation *(1.10)*.

$$F_D = \frac{1}{2} \cdot \rho_{equ} \cdot C_D \cdot S_p \cdot V_o{}^2 \qquad (1.10)$$

These coefficients depend on the flow regime and velocity streamlines. Studies and measurements showed that an isolated sphere in a constant velocity steam has a drag coefficient $C_D = 0.45$ within the following range of Reynolds number: $10^3 < R_e < 10^5$ [53]. Similarly, the drag coefficient of a cylinder in constant velocity stream is $C_D = 1$ over the same Reynolds interval [54].The obtained drag force is given in (1.10), with ρ_{equ} the density of the considered fluid and V_o the constant speed of the flow (for REB, the orbiting speed).

In the case of REB, the rolling elements are not isolated in space. Firstly, assuming an overall stationary regime will imply that the flow trail past one rolling element will influence the front of the next one. Some repetitions therefore occur inside the bearing chamber. Pouly suggested that the drag coefficient C_D should be taken for a sphere aligned with other spheres[17]. With Computational Fluid Dynamics analysis confirmed with some measurements, he managed to show that its value is $C_D = 0.09$ [55]. Marchesse found a similar comparison for the study of the flow across aligned cylinders[54]. He also found that the presence of the cage does not change the flow regime, *ie* the drag coefficient, but the projected area [56]. Furthermore, the flow takes place in a confined environment. The presence of the rings around the rolling elements also contributes to modify the flow regime. Needless to say, the inner ring own rotation also changes the flow regime. Finally, in addition of the rolling element orbital motion, the elements also rotate around their own axis. This additional rotation has scarcely been studied in the REB drag analysis. In conclusion, analytical formulas are provided to calculate drag power losses for aligned rolling elements with the presence of rings and cage. The complex motions within REB has not been thoroughly modelled by analytical formulae yet. The drag power losses are negligible below one million $N \cdot d_m$criteria.

In addition to the rolling element fluid interaction, the cage rotates with a relative motion with both rings. Because it has a relatively small clearance with the guiding ring, it can be assimilated as a short journal bearing filled with oil which formulae for resistive force is given in equation *(1.11)*.

$$M_C = \frac{2\pi * \mu_{oil} * L * \Delta\omega * \left(\frac{d_m}{2}\right)^3}{\epsilon} \qquad (1.11)$$

In this equation, μ_{oil} is the oil dynamic viscosity, L the width of the cage, $\Delta\omega$ is the relative speed difference and ϵ the diametral clearance between the cage and the concerned ring. This moment applied to the cage centre generates by reaction a cage force acting on each rolling elements. Below the one million $N \cdot d_m$ criteria, it is relatively low compared to the rolling resistance but increases linearly with shaft speed.

In another matter, bath lubricated REBs have another heat production from fluid interaction. Their lower rolling elements are completely submerged while the upper rolling elements are not. A free surface is formed at the interface between oil sump and air. This free surface is rammed by the rolling elements. Heat is generated by this percussion. Gear studies showed that the splash-lubricated gear phenomenon differs from a gear rotating in a homogenous fluid. This comparison with gear studies highlights the difficulty of creating a single model for both bath and jet lubrication.

Recent Computational Fluid Dynamics analyses have also tried to grasp the REB fluid interaction. In 2014, Hu *et al.* used Volume Of Fluid technique with the Reynolds averaged equations to model the repartition of oil for different configurations of jet nozzle [57]. Some comparisons are offered concerning outer ring temperature measurements. Adeniyi modelled the jet injection on a portion of the bearing chamber using repetitive limit conditions [58]. Using transient VOF, he was able to show that the droplets of oil in the oil-air mixture were moving at about 30% of the inner ring rotation, and that this ratio is nearly constant with speed increase. In 2016, Wu *et al.* continued the work of Hu on the same test rig and were able to test more parameters such as, number of nozzles used, oil flow rate, inner ring speed and jet velocity[59]. The temperature measurements agreed well with experiments, yet no emphasis was put on the prediction of power losses. In 2017, Feldermann used a coupled model to compute the flow within the roller bearing chamber then past only one element with higher resolution [60]. In doing so, he was able to include both orbital motion and the elements rolling into the computation. The result yielded speed distribution and generated power losses. Good agreements are found with experiments, but no parametric law was extrapolated from the result.

In conclusion, the recent REB CFD-based models are far too complex a tool to predict REB power losses yet. The simpler drag formulae in *(1.10)* using empirical coefficients is a simpler method to do so. The drag and churning power losses are altogether negligible below a certain speed.

1.7.3 Friction from Sliding

Sliding between two surfaces will result in heat production. Concerning the contact between two dry surfaces, Coulomb defined that the coefficient of friction is constant towards operating conditions and depends on the material properties [61]. In opposition, the contact between two lubricated sliding surfaces is an entire branch of science. The classical Newtonian fluid traction model dictates that the shear stress τ_0 of a fluid is proportional to the gradient of speed across the fluid, thus defining the viscosity.

$$\tau_0(x,y) = \eta(x,y) \cdot \frac{V_g(x,y)}{h_c} \qquad (1.12)$$

In equation *(1.12)*, the gradient of speed can be assumed to be the sliding speed V_g divided by the central film thickness h_c, nearly constant over the ellipse. This sliding speed has a constant component called macro sliding, corresponding to a rolling speed difference and a local component depending on the ellipse coordinates. Within highly

loaded contacts, Barus described an exponential expression for the dynamic viscosity η towards pressure[62]. Indeed, the high-pressure glass transition of the lubricant constrains it to behave as a solid. Roelands derived Barus's formula to enable a closer understanding of high pressure viscosity[63]. Both models are widely used for the calculation of EHL contact viscosity today. A review on the pressure coefficient calculation can be found in [64].

Because the viscosity of the film thickness is high, the fluid does not act as a Newtonian fluid anymore. Ree-eyring established a limiting shear stress $\tau_{\lim}$ that will prevent an unreasonable shear stress[65]. The limiting shear stress is a parameter depending on oil characteristics, pressure and temperature. The sliding traction force T_S is calculated over the contact from the shear stress in equation *(1.13)*.

$$T_S = \iint_{-a\ -b}^{a\ \ b} \tau_{\lim} \cdot \sinh^{-1}\left(\frac{\tau_0(x,y)}{\tau_{\lim}}\right) dxdy \qquad (1.13)$$

Johnson added an elastic term that accounts for the linear behavior of shear stress derivative towards time[66]. Applied to REB contacts, most studies used this form to calculate the shear stress [52,67]. This elastic addition has been sometimes neglected [37,68]. New research showed that in steady state conditions, elastic response of the lubricant is definitively negligible [69].

The sliding friction calculation is highly nonlinear. The main unknown in this calculation is the macro sliding speed. This macro sliding speed depends on the ball equilibrium, which depends on the sliding traction forces. In 2002, Houpert showed that the sliding traction can be calculated from the motion equilibrium [38]. He showed that the macro sliding traction forces depends on the rolling contribution previously mentioned. In appendix D, the sliding forces are calculated considering only the rolling traction force scheme. It is shown that depending on whereas the drag force and churning force are negligible, the macro sliding forces are equal to the rolling force and opposite in signs. Equation *(1.13)* is then inversed to calculate the sliding speed.

As a conclusion, the complexity of the REB local sliding contribution makes a single power loss model impossible. Because of the nonlinearity of the problem, only an iterative calculation can yield the sliding speeds.

1.7.4 Conclusion

In conclusion, three main contributions are observed for power losses in REB: the rolling resistance, the drag and churning heat production and the sliding friction from the contact between rolling elements and raceways. For the rolling resistance, different formulations have been used over the years. Yet, it has sometimes been completely neglected in past studies. Fluid interaction contribution has been thoroughly studied over the years. At high speed, it is the first contribution to power losses. Different methods exist, either algebraic, empirical or more recently, CFD analysis. Ultimately, they are negligible below the high-speed criteria. Finally, the sliding traction forces are the

consequences of different sliding mechanisms. At high speed, a dedicated software is compulsory to compute the equilibrium. The different sliding mechanisms such as skidding, spinning, gyroscopic motion and micro-sliding are intertwined due to the non-linear traction models. Some models predict relatively low sliding power losses in the case of high speed angular ball bearing [5–7] and negligible sliding power losses in the case of roller element bearings [8].

	Speed	Load	Viscosity	Oil flow rate
Rolling Hysteresis	-	1.33 [41]	-	-
Rolling	2/3 [3,36,38,39]	0.47 [38]	2/3 [3,36,38,39]	*TBD*
Sliding	*TBD*	*TBD*	*TBD*	-
Cage interaction	1 [5,55]	-	1 [5,55]	*TBD*
Drag and Churning	2 [5,55]	-	-	*TBD*

**TBD: To Be Determined*

Table 1.3 : Known exponents over parameter of influence for the friction mechanisms developed as a shaft resistive moment

On Table 1.3, the exponents over some parameter of influence are presented for each friction mechanisms. For the influence of oil flow rate, some questions remain: has oil flow rate a role in the replenishment mechanisms for the rolling friction? How does oil flow rate impact the drag and churning interaction? Houpert showed that the impact of oil flow rate is strictly thermal [40]. Other advances that drag power loss depends on the oil flow rate [70,71]. It can also be noted that only the rolling hysteresis is speed independent. The load independent mechanisms are the drag, the churning and the cage interaction. In any case, because of the non-linearity of the sliding friction, no exponent can be directly expressed. The load and motion equilibriums are required to compute the sliding friction in an iterative approach.

The necessity of easily predicting REB heat production for industrial purposes makes local phenomena hard to exploit. In order to easily predict the REB power loss, alternatives methods also exist. They are based on either empirical or numerical parametric investigations and are sometimes referred as global power loss models.

1.8 Global Power Loss Models

Predicting power losses in transmission system is an important phase of any new development. The cooling system should be dimensioned to match the amount of heat

generated. REB losses are not negligible in that matter. Global models depicted below aim at predicting REB power losses with minimum inputs. The models yield a resistive torque, which multiplied by shaft speed gives the total REB power loss.

1.8.1 The Harris-Palmgren Model

The need to predict this amount of heat is not recent, in the early 50's Palmgren established a global power loss model for the SKF company [9]. At that time known as the SKF model, it was popularized by Harris's Rolling Bearing Analysis [10].

$$M_{HPM} = M_1 + M_0 \tag{1.14}$$

This model separates a load-independent and a load-dependent contribution (Equation *(1.14)*) , which are measured separately.

If $N \cdot \upsilon > 4770$ $[rad \cdot m^2/s]$

$$M_0 = f_0 \cdot 4.5 \cdot 10^3 \cdot (\omega_i \cdot \upsilon_{oil},)^{2/3} * d_m^3 \tag{1.15}$$

If $N \cdot \upsilon < 4770$ $[rad \cdot m^2/s]$

$$M_0 = f_0 \cdot 15.9 \cdot d_m^3 \tag{1.16}$$

Concerning the load-independent contribution, M_0, two equations *(1.15)* and *(1.16)* exist depending on the product of kinematic viscosity υ and shaft speed ω_i product. The value of the coefficient f_0 depends on the REB type and on the lubrication technique employed. This coefficient can also vary by a factor of two for some heavy design bearing. The kinematic viscosity υ is taken at the oil injection temperature, or at the oil bath temperature. The exponent two-third above the product of kinematic viscosity υ_{oil} and shaft speed ω_i is very distinctive of a rolling friction contribution. The REB bore diameter d_m is taken at the power three to account for the REB geometry. No pieces of information about the test rig conditions or about the tested bearings are available to the author's knowledge.

$$M_1 = f_1 \cdot F_B \cdot d_m \tag{1.17}$$

For Ball Bearing

$$f_1 = z \cdot (F_s/C_0)^y \tag{1.18}$$

Concerning the load-dependent contribution, M_1, the value of the coefficient f_1 also depends on the REB type and another equation is used for ball bearings. The static load capacity C_0 and two empirical parameters z and y are used to define f_1 for ball bearings in equation *(1.18)*. It appears constant for roller bearings although it can also vary by a factor of two in some heavy design bearings. The equivalent load F_B and the equivalent static load F_s depends on the loading case scenario [72,73]. For pure radial load $F_B = F_s = F_r$ and for pure axial load, $F_B = F_s = F_a$. The load-dependent contribution is proportional to the REB bore diameter d_m to account for the REB geometry. It can be noted that the tested REBs all shear a geometric ratio γ of 0.2 [74]. Additionally, the raceway osculations have at direct influence on the load dependent moment according to Palmgren but are left out of the model[74].

In conclusion, the Harris-Palmgren model has the advantage of being a ready-to-use tool. No specific knowledge about load distribution, components temperature or detailed geometry is required. Only the bore diameter d_m is used to characterized geometry.

1.8.2 The New SKF model

Recently, SKF has created another global model to predict REB power losses. This model, assumed to be an interpolation of BEAST results, is catalogue-based [11,12]. The model separates the resistive torque into three contributions: rolling, sliding and drag (equation *(1.17)*). The author points out that the drag contribution can in fact be separated into two by-products, respectively a drag model M_{drag} and a splash-lubricated model M_{splash}.

$$M_{SKF} = M_{rr} + M_{sl} + (M_{drag} + M_{splash}) \quad (1.19)$$

The model uses several parameters R_1, S_1, K_{rs} and K_z. R_1 and S_1 depending on the REB series that can be found in table issued from the catalogue.

$$M_{rr} = 1.17 \cdot 10^{7} \cdot \varphi_{rs} \cdot \varphi_{ish} \cdot G_{rr} \cdot (\omega_i \cdot \upsilon_{oil})^{0.6} \quad (1.20)$$

For DGBB

$$G_{rr} = R_1 \cdot d_m^{1.96} \cdot F_r^{0.54} \quad (1.21)$$

$$\varphi_{ish} = \frac{1}{1 + 1.58 \cdot (\omega_i \cdot d_m)^{1.28} \cdot \upsilon_{oil}^{0.64}} \quad (1.22)$$

$$\varphi_{rs} = \exp\left(-\left(3.02 \cdot 10^{8} \cdot K_{rs} \cdot \omega_i \cdot \upsilon_{oil} \cdot (d_e + d_i)\right) \cdot \left(\frac{K_z}{2(d_e - d_i)}\right)^{0.5}\right) \quad (1.23)$$

About the rolling contribution M_{rr}, the product of shaft speed ω_i times kinematic viscosity υ at the exponent 0.6 is again found in Equation *(1.20)*. The load parameter G_{rr} depends on mean diameter, axial and radial loads and some other catalogue-based coefficients. Equation *(1.21)* provides it for deep groove ball bearing in radial load scenario. The two terms φ_{rs} and φ_{ish} are respectively the replenishment and the thermal reduction factor. They aim at reducing the rolling contribution at high speed and high viscosity conditions, as well as for large bore diameters. The thermal reduction factor stands for the lubricant shearing at the contact inlet, decreasing effective viscosity (equation *(1.25)*). The replenishment reduction factor represents a kinematic starvation that can occur if the ability to self-refill the contacts is insufficient (equation *(1.26)*). The inner ring internal diameter d_i and the outer ring external diameter d_e are used, arguably as a difference to account for the size of the rolling elements. The oil flow rate, or the amount of grease, is absent from formulations. As said earlier in this chapter, using reduction factors to calculate film thickness have been done in the past. However, these models used detailed contact geometry and have not yet been applied to a full REB analysis to the author's knowledge. In contrast, the two terms used in the SKF model only need shaft speed, oil viscosity and external geometry.

$$M_{sl} = 1.66 \cdot 10^{-4} \cdot (\varphi_{bl} \cdot \mu_{bl} + (1 - \varphi_{bl}) \cdot \mu_{EHL}) \cdot G_{sl} \quad (1.24)$$

For DGBB

$$G_{sl} = S_1 \cdot d_m^{-0.26} \cdot F_r^{5/3} \quad (1.25)$$

$$\varphi_{bl} = \exp(-(1.54 \cdot 10^5 \, (\omega_i \cdot v)^{1.4} \cdot d_m)) \quad (1.26)$$

At first glance, the sliding contribution in equation *(1.24)* bears a resemblance to a friction coefficient times load relationship. The load parameter G_{sl} depends on mean diameter, axial and radial loads and some other catalogue-based coefficients. Equation *(1.25)* provides it for deep groove ball bearing under radial load scenario. the model uses the weighting factor φ_{bl} to account for the lubrication regime, from limit to EHL. A value of friction coefficient is given for both regimes, namely μ_{bl} and μ_{EHL}, depending on REB types and oil characteristics. With speed increase, the sliding contribution decreases as the regimes evolve from boundary to EHL.

For Ball Bearing

$$M_{drag} = 3.65 \cdot 10^{13} \cdot V_m \cdot K_{ball} \cdot {d_m}^5 \cdot {\omega_i}^2 \quad (1.27)$$

The original drag contribution is an addition of two terms, M_{drag} and M_{splash}. The first one, M_{drag}, differs from ball bearing to roller bearing. The equation (1.27) is given for ball bearings. The resistive moment M_{drag} is proportional to the square of the shaft speed. The term V_m depends on the oil level for bath lubrication. For jet lubrication, SKF suggests taking half the element diameter instead an oil level into account.

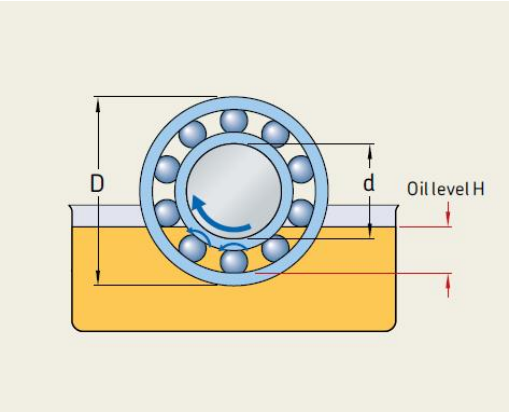

Figure 1.6: Bath lubrication scheme [11]

$$M_{splash} = 4.45 \cdot 10^5 \cdot {d_m}^3 \cdot {\omega_i}^2 \cdot \left(\frac{\omega_i \cdot d_m^2 \cdot f_t}{v_{oil}}\right)^{-1.379} \cdot R_s \quad (1.28)$$

The second term M_{splash} covers the influence of the oil level. The parameter t corresponds to the immersion angle. The parameter R_s corresponds to an equivalent wet surface. The ratio $\omega_i \cdot d_m^2 \cdot f_t / v$ can be looked at as a Reynolds number, where the characteristic length is a projection of the mean diameter along the free surface. It can be noted that the splash contribution will decrease with an increase in Reynolds number. [75,76].

In conclusion, the first term is predominant for low immersion, high-speed conditions, while the other is predominant for low speed, high immersion conditions. No reduction factor is present in the drag and churning terms; therefore, both contributions will escalate at high speed.

The model SKF is made of different bricks that seem inspired from physics. Yet, its manipulation is difficult compared to the two other global models. Nonetheless, some manage to curve-fit this model on a thrust ball bearing using different lubricants under different operating conditions. Only two friction coefficients μ_{bl} and μ_{EHL} are used to catch the different transition regimes for each lubricant [13,14].

1.8.3 Conclusion

In conclusion, the two above-mentioned global models all used coarse geometry and catalogue coefficients as inputs to predict power losses. Both the SKF and Harris-Palmgren model are used for a large panel of REBs, including deep groove ball bearing. Except for the SKF model, the lubricant viscosity is enough to characterize any lubricant propensity to generate heat. Each model has one contribution which includes a product of viscosity and speed at the power about 2/3. For the Harris-Palmgren model this contribution is load-independent, for the SKF model, these contributions depend on the applied load. The SKF model accounts for different lubrication regimes and for fluid-interaction contributions that supposedly can predict pure drag heat production and bath-lubricated bearing splash heat production.

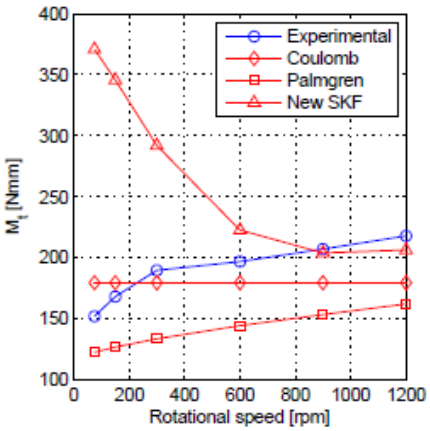

Figure 1.7: Global models comparisons [14]

On Figure 1.7, the SKF model and the Harris-Palmgren model are compared to experiments for a thrust ball bearing [14]. Temperature were kept constant for each speed. The Coulomb model is a simple friction-coefficient model that was represented here. It can be seen that at low speed, the SKF model predicts an increase in resistive torque. This increase in resistive torque is due to the sliding contribution and the weighting factor φ_{bl} that accounts for lubrication regimes. The experiment on the other hand do not show any sign either of a change of lubrication regime, or of sliding friction

for that matter. The Harris-Palmgren evolution towards speed is similar to the experiment, but its value is too low.

1.9 Conclusion

As a conclusion, the different friction mechanisms within REBs were investigated in light of the literature. Three contributions are predominant: the rolling friction at each contact inlets; the sliding friction from the eventual sliding occurring between the rolling element and the raceways; the drag and churning phenomena occurring between the moving parts and the lubricant. Below one million $N \cdot d_m$, the drag power losses are negligible. The rolling friction has been considered via different considerations over the years. The product of speed times viscosity is present at the power two third. The load is also present with a power smaller than unity.

The difficulty to apply local power losses model lead to the creation of different global models. The Harris-Palmgren model separates a load-independent contribution from a load-dependent one. Only the bore diameter is used to characterize REB geometry. The SKF model separates the local phenomena into distinctive contributions. The bore diameter is again used as the main geometrical input, although other REB dimensions are also used alongside with coefficients depending on REB series. The two models present a term with a speed times viscosity product at the power around two third. The Harris-Palmgren term is load-independent while the SKF term depends on the applied load with a power smaller than unity. None of the two global models incorporates the oil flow rate. For the Harris-Palmgren model, the viscosity is the only parameter to account for the lubricant.

Global power loss models are compliant with the requirements of an entire gearbox thermal simulation. Yet, some questions remain on the capacity of global model to predict REB power losses. Are the models accurate as it is, or do they need their coefficients to be adjusted on measurements? In the next chapter, empirical investigations on a REB test rig equipped with a torque sensor are made. Some parameters of influence such as speed, load, temperature, oil flow rate, lubrication design and REB geometrical features will be investigated on a test rig. In order to compare two REBs on this specific test rig, the deep groove ball bearing type was selected. The accuracy of the Harris-Palmgren and the SKF models and their adaptability to predict resistive torque will be discussed.

Chapter 2:
Empirical Investigation

2.1 Introduction

In the previous chapter, the main features of the thermal behavior of rolling element bearings have been detailed in light of the literature. The prediction of power losses has been outlined as a crucial cornerstone in that matter. Local heat production phenomena such as rolling, sliding and drag-churning are examined. Conversely, global power loss models are also detailed. Both the Harris-Palmgren and the SKF models are presented. Their facility of use makes them indisputably powerful tools for both industry and research.

As shown by Niel and reported in the previous chapter, the global power losses are best evaluated when considering the average temperature of the REB rings. In the following section, the inner ring temperature is not measured for each experiment. The outer ring temperature will therefore be considered in the calculation of viscosity.

In order to understand how accurately the global models can predict the REB heat production, a specific test rig is used. Prior to discussing the results, the test rig and its components are presented. Then the Harris-Palmgren model is investigated on dedicated experiments. The SKF model is similarly investigated. Finally, a discussion is presented on whether the two global model can predict accurately power losses for any REB.

2.2 Experimental test rig

The test rig used in this chapter was developed at LabECAM laboratory specifically to measure REB resistive torque and to monitor its temperature distribution (Figure 1.1).

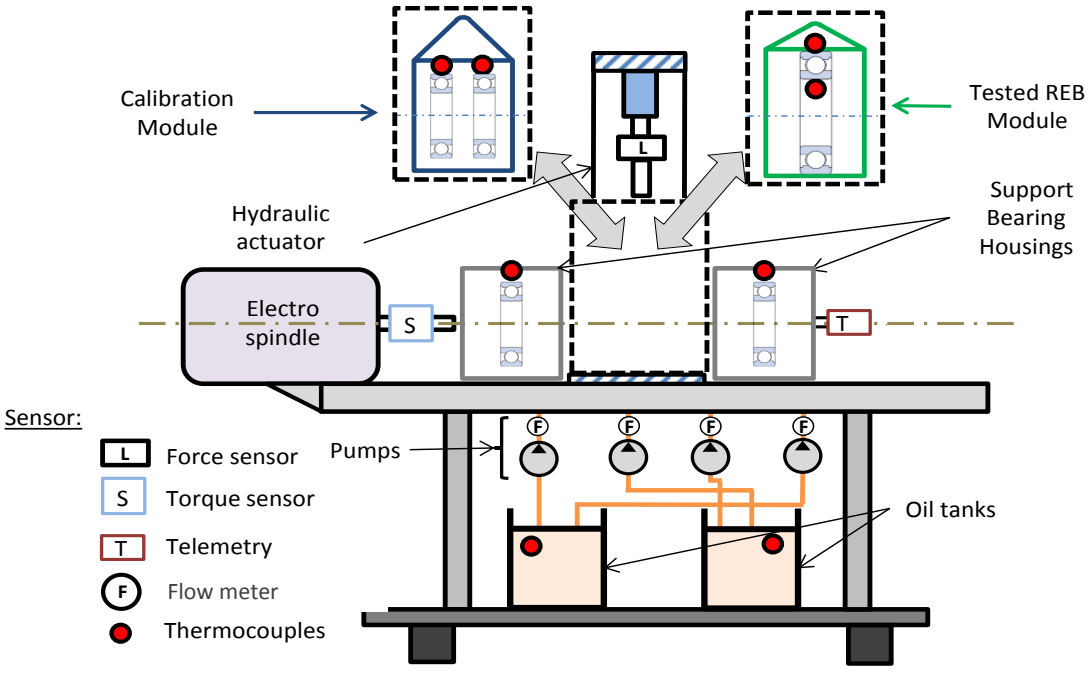

Figure 2.1 : Test Rig scheme

This test rig was designed to be able to investigate REBs of different dimensions. In order to do so, the driveline is dissociated into separated shafts and assembled from the electric spindle to the telemetry system. A hydraulic cylinder provides a load at the center of the module. On both sides of this central module, support REBs are symmetrically located. They carry back the applied radial load. The central space is occupied by either the calibration module or the tested REB module. On the one hand, the calibration module integrates two deep groove ball bearings identical to the support bearings, referred as Type A. On the other hand, the tested REB module integrates a larger single deep groove ball bearing, referred as Type B. During the calibration phase, the torque sensor measures the resistive torque of four Type A bearings being equally loaded. Later, the support REB resistive torque will be subtracted from the whole driveline measured torque to isolate the Type B REB torque measurement. The characteristics of both types A and B are found in Table 2.4. As a conclusion, both calibration module and tested REB module can be used in order to provide experimental data for two different REBs.

		Type A	***Type B***
Location		Support Housings Calibration module	Tested REB Module
Type		Deep Groove Ball Bearing	Deep Groove Ball Bearing
Bore dimeter [mm]	d_m	*61*	*85*
Outer diameter [mm]	d_e	*72*	*95*
Inner diameter [mm]	d_i	*50*	*75*
Width [mm]	B	*12*	*10*
Static load [kN]	C_0	*11.8*	*14.3*
Ball Diameter [mm]	*D*	*6.75*	*5.55*
Ball Number [-]	*Z*	*16*	*26*

Table 2.4 : REB characteristics

The lubrication system is separated into two fully independent circuits with two oil tanks and four oil pumps. The modules can either be bath-lubricated or jet lubricated with different oil jet temperatures and oil flow rates. Therefore, different types of lubrication can be investigated on the tested REB module with given lubrication conditions for the support housings. Both tanks are filled with a standard transmission oil, defined by characteristics presented in Table 2.5.

Kinematic Viscosity at 40°C [cSt]	ν_{oil}	*36*
Kinematic Viscosity at 100°C [cSt]	ν_{oil}	*7.7*
Density at 25°C $[kg/m^3]$	ρ_{oil}	*860*

Table 2.5 : Oil characteristics

The measurement of the resistive torque is achieved by a torque sensor between the spindle and the driveline. A force sensor measures the applied load and the four flow sensors measure injected oil flow rates. Type T Thermocouples are used to measure the temperatures of the outer and inner rings, oil inlets and outlets, oil tanks, ambient air and eventually of housing areas when required. A List of the used actuators and sensors is presented in Table 2.6 and Table 2.7. A detailed description of this test rig is provided by Niel [15].

Component	***Supplier / Model***	***[Min Max] value***
Electrical Spindle	*HSD Mechatronics / H6161H0669*	*[0 24000] rpm*
Hydraulic cylinder	*CMB / A3063H0100C08/CP22S44*	*[0 20] kN*
Pumps	*JABSCO/ 23230-2014*	*[10 100] l/h*

Table 2.6 : Power Actuators description

Component	***Supplier / Model***	***[Min Max] value***	***Relative Error***
Torque Sensor	*Manner / 70234*	*[0 10] N.m*	*0.02%*
Telemetry System	*Manner / Multi Channel Sensor Signal Amplifier*	*[0 20000] rpm*	*0.02%*
Flow sensor	*Kobold ZOK-ExK/ZxK*	*[10 100] l/h*	*1 %*
Force sensor	*SCAIME K1427*	*[0 -20] kN*	*<1%*
Thermocouples	*Type -T*	*[-185 200] °C*	*0.1°C*

Table 2.7 : Sensors description

2.3 Calibration phase

This section presents the calibration phase. The calibration module, which integrates two Type A REBs, is mounted at the centre of the shaft assembly. The calibration phase is performed in order to quantify the support REBs resistive torque. Indeed, the resistive torque of the support REBs should be subtracted in order to isolate the resistive torque of the central module. It can be noted that different lubrication features can be investigated separately for the tested module and the support REBs since the central module has a separated lubrication system from the support ones. However, testing different shaft speeds or applied loads on the tested REB will influence the support REBs resistive torque. Regarding the calibration part, the lubrication method is oil injection. The oil flow rate chosen is the minimal oil flow rate accepted by the flow sensor, *ie* 10 l/h.

In order to do so, the Harris-Palmgren model described in the previous chapter is used. The coefficient and exponent were modified to enable the model to fit the calibration measurements as reported in *(2.1).*

$$M_{support*} = 5.8 \cdot 10^{-4} \cdot \left(\frac{F_r}{C_0}\right)^{0.55} \cdot F_r \cdot d_m + 7.7 \cdot 10^{-7} \cdot d_m^3 \cdot \nu_{oil}^{0.66} \cdot \omega_i^{0.51} \qquad (2.1)$$

In this equation, F_r is the applied radial load, C_0 the static load capacity, d_m the bore diameter, ν the kinematic viscosity taken at the concerned support outer ring temperature and ω_i the shaft speed.

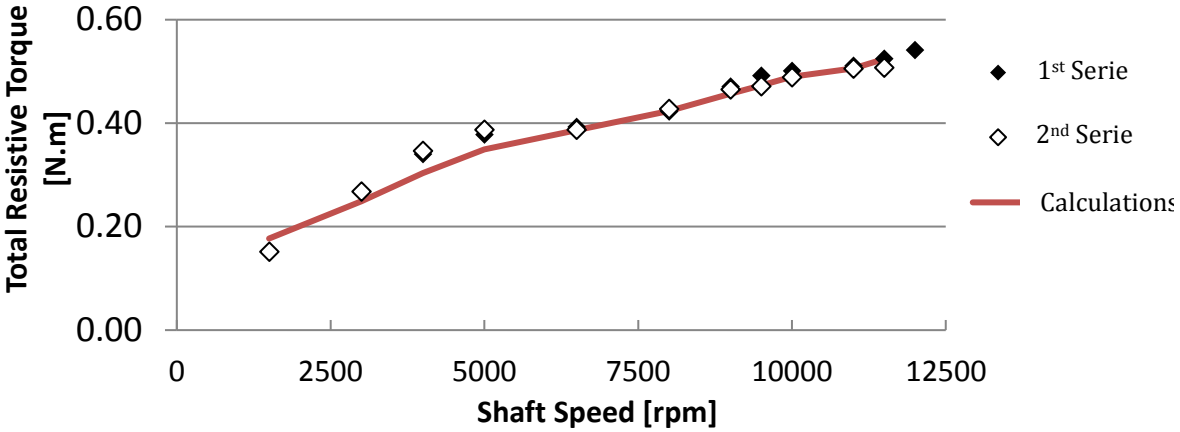

Figure 2.2 : Repeatability and model

Type A Bearing; 70°C – 12L/h oil injection; 400 N Total Radial Load

A repeatability test is conducted for the calibration phase (Figure 2.2). The model presented is sum of the four support resistive torque models. The total average relative error between the two experimental series is less than 2%. However, the total average relative error between the modelled torque and experiments is within 5%. The maximum error (17%) is observed at 1300 rpm. This model is therefore sufficiently accurate to subtract the support bearing resistive torque from the total measured torque in order to isolate the desired torque measurements, as seen in equation *(2.2)* and *(2.3)*.

Calibration Module

Type A Resistive Torque:

$$M_{type\ A} = \frac{(M_{total} - M_{support1} - M_{support2})}{2} \quad (2.2)$$

Tested REB Module

Type B Resistive Torque:

$$M_{type\ B} = M_{total} - M_{support\ 1} - M_{support\ 2} \quad (2.3)$$

The injection campaigns are conducted as follows: after a heating phase of twenty minutes, where the oil injection is brought to the desired temperature, the appropriate oil flow rate and applied radial force are set on the test rig, evolving at the higher desired rotational speed. Afterwards, the shaft speed is successively diminished every two minutes until every speed step is tested.

The bath-lubricated campaign is also conducted after a heating phase, however, each speed step lasts twenty minutes in order to compile sufficient data points at different temperatures for each tested set of conditions.

2.4 The Harris-Palmgren model: results and discussion

This section focuses on analysing the Harris-Palmgren model capacity to predict REB resistive torque. Both the calibration and tested modules are used in order to test two different REBs. The Harris-Palmgren model, detailed in section 1.8.1, separates the load-independent contribution M_0 in *(2.5)* and the load contribution M1 in *(2.6)*.

$$M_{HPM} = M_1 + M_0 \quad (2.4)$$

$$M_0 = f_0 \cdot 4.5 * 10^3 \cdot (\omega_i * v)^{2/3} \cdot d_m^3 \quad (2.5)$$

$$M_1 = z \cdot \left(\frac{F_s}{C_0}\right)^y \cdot F_B \cdot d_m \quad (2.6)$$

	f_0	z	y
Oil Injection	4	0.004-0.006[i]	0.55
Oil Bath horizontal shaft	2		

[i]: *depending on light-heavy bearing series*

Table 2.8 : Original Harris-Palmgren model parameter values for deep groove ball bearing

In ***Table*** 2.8, the Harris-Palmgren model original coefficients are given for deep groove ball bearing in both oil injection and oil bath lubrication for a horizontal shaft. Their value can double depending on the lubrications techniques and on the REB series.

2.4.1 Evolution of resistive torque towards speeds

The calibration module is first used to investigate the resistive torque evolution *versus* speed. Four series of tests are made with a shaft speed from 12 300 to 1 330 rpm. At each speed, the operating conditions are maintained for about two minutes. Two different oil tank temperatures and two radial loads are tested forming four series of tests, as reported in Table 2.9. The calibration module integrates two Type A REBs, where the radial load is divided equally between them.

	Serie 1	Serie 2	Serie 3	Serie 4
Oil Tank Temperature [°C]	80	70	80	70
Total Radial Load [N]	400	400	1200	1200

Table 2.9 : Type A REB series of tests

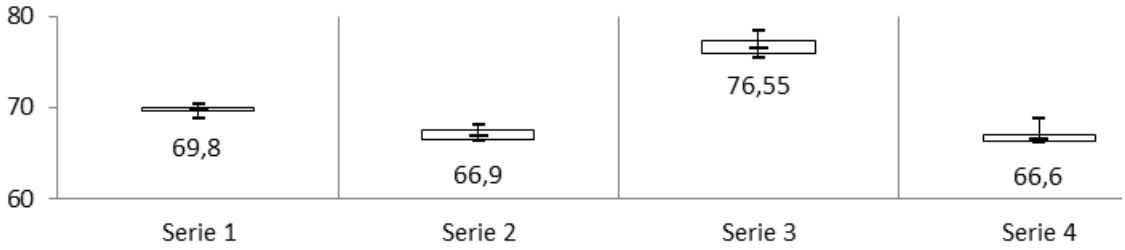

Figure 2.3 : Injection temperature bar plots for the calibration module

The oil injection temperature discrepancy corresponding to the calibration phase is shown in Figure 2.3. The injection temperature is kept constant during each series of tests. The influence of oil tank temperatures on the injection temperature depends on the heat transfer within the tubes and to the surrounding environment. Therefore, for a similar oil tank temperature, the injection temperature may vary. However, the experiments were sufficiently stabilised in temperature with little dispersion as observed.

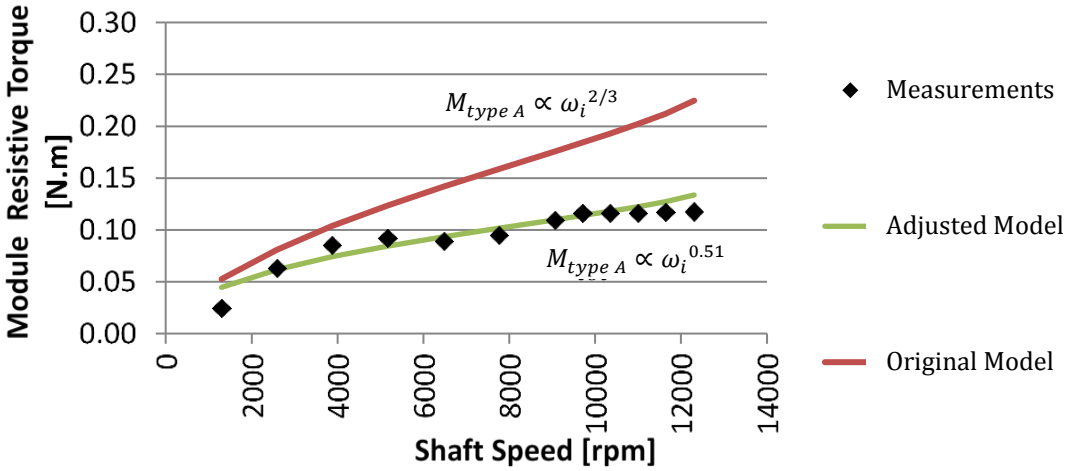

Figure 2.4 : Evolution of resistive torque towards speed increase : Original Model, Adjusted Model and Experiments for serie 4 test.

Type A Bearing; 70°C – 12L/h oil injection; 600 N Radial Load

On Figure 2.4, the original Harris-Palmgren model is not coherent with the experiment. The best fit is found the shaft speed at the power 0.51 instead of 2/3. Between 2500 and 5000 rpm, the model slightly underestimates the resistive torque. This may be due to the insufficient outflow mechanisms at this range of speeds that generates a small increase in resistive torque. On the other hand, at the lowest speeds, the model overestimates the resistive torque. This is linked to the calibration inaccuracy at this specific speed.

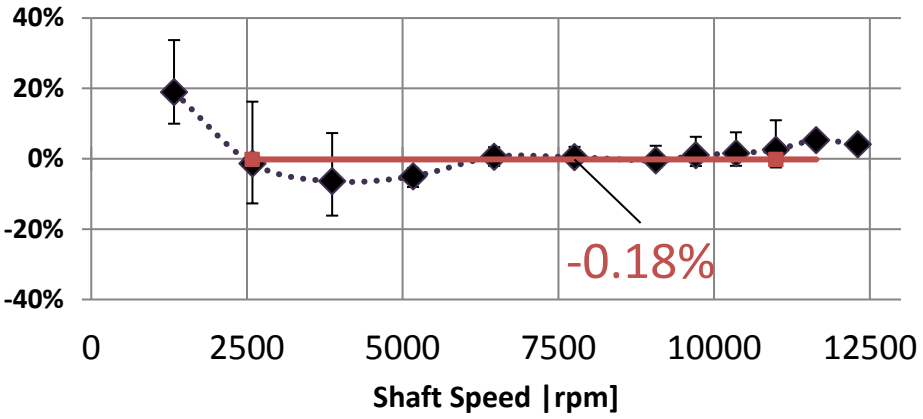

Figure 2.5 : Average relative error between adjusted model and experiments over the four series.

Type A Bearing, oil injection lubrification

The average relative error between the measured resistive torque and the modelled torque for the four series of tests are presented in Figure 2.5. Generally, the model is in good agreement with experiments. The overestimated value at the lowest speed is as high as 19%. At the other speeds, the torque is successfully predicted (less than 7% error). A non-negligible dispersion of error is found between 2500 and 5000 rpm. It confirms that the small increase of resistive torque at these speeds are due to experimental flaws and not model inaccuracies.

During this first set of experiments, it is observed that the load dependent contribution is not significant at both radial loads 200N and 600 N per REB. Indeed, these radial loads represent less than 5% of the static capacity of type A REB. The comparison of these contributions using the Harris-Palmgren model is presented on Figure 2.6 for a radial load per REB of 600N.

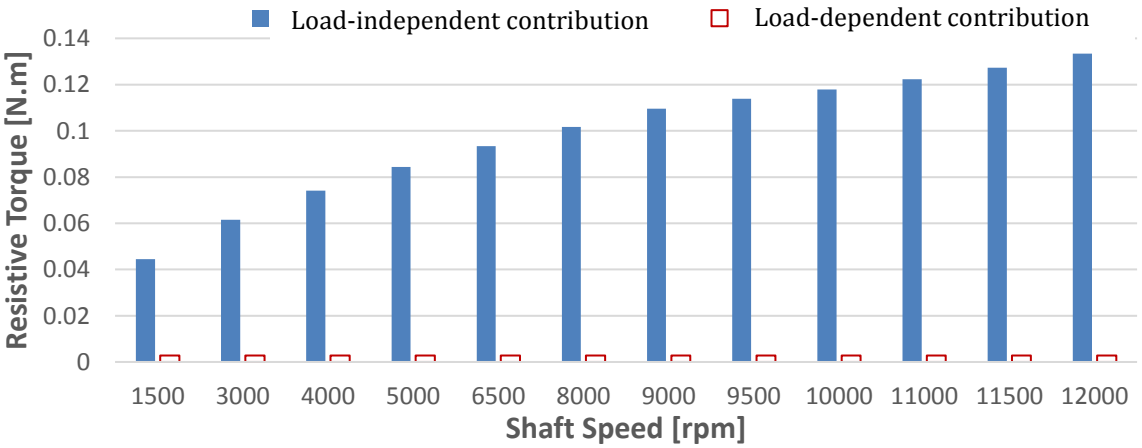

Figure 2.6 : Comparisons of load-dependent and load-independent contribution for serie 4

Type A Bearing; 70°C – 12L/h oil injection; 600 N Radial Load

This set of experiments therefore evaluates the load-independent contribution in the Harris-Palmgren model. This contribution for jet injection is modified as reported in *(2.7)*.

$$M_{0-injection} = 7.7 \cdot 4.5 * 10^3 \cdot \omega_i^{0.51} \cdot \upsilon^{2/3} \cdot d_m^3 \qquad (2.7)$$

2.4.2 Evolution according to lubrication designs

In this section, the calibration module is bath lubricated. Dipsticks ensure constant levels of bath lubrication as shown on Figure 2.7. The test lasts for 20 minutes at each speed. Afterwards, the test rig is stopped to refill the module to the appropriate bath level. The temperature of the calibration module is therefore not controlled. At low speeds, low power losses induce low temperatures, whereas at high speed, temperatures increase, reducing viscosity and heat dissipation. This phenomenon can be seen on Figure 2.8, where the resistive torque is higher for bath lubrication compared to jet lubrication at low speeds.

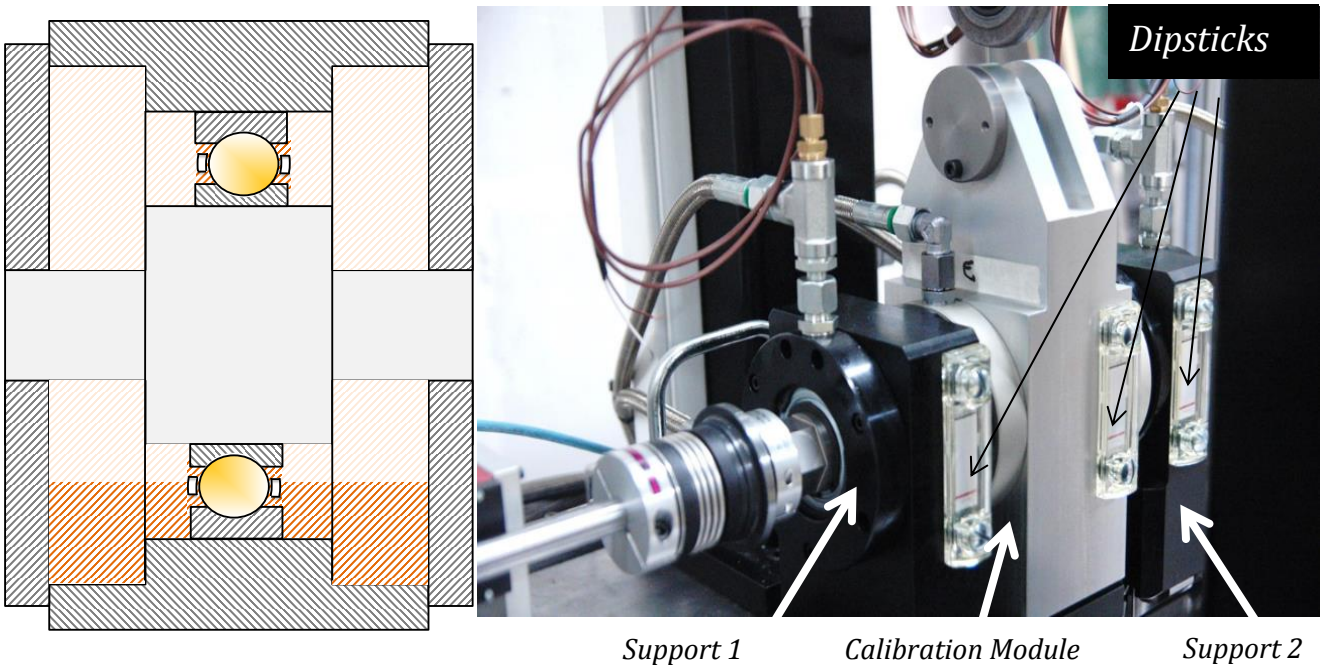

Figure 2.7 : Calibration assembly with bath lubrication dipsticks outlined and bath lubrication scheme

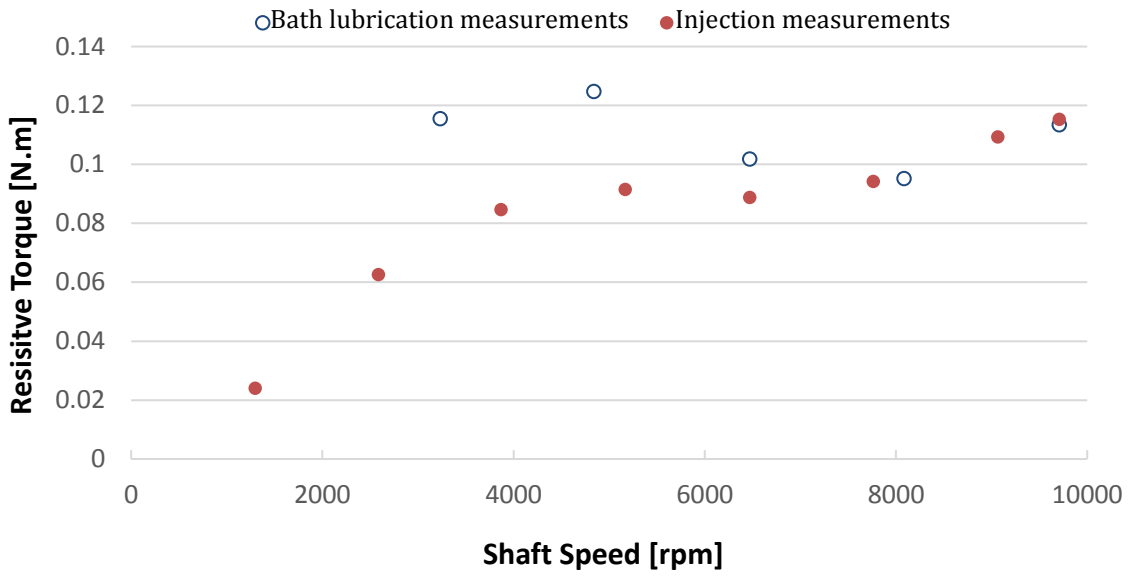

Figure 2.8 : Comparison of resistive torques between oil injection and bath lubrication

Type A Bearing; serie 4 test and bath lubrication; 600 and 500 N total applied radial Load

In order to compare both jet injection and bath lubrication, temperature differences must be taken out of consideration. Both global models consider that temperature only influences viscosity. In the Harris-Palmgren model, the viscosity is to the power 2/3 in the load-independent contribution. Similarly, the SKF model considers 0.6 or viscosity in the rolling contribution, although viscosity also has an influence on the reduction factors and on the lubrication regime partition function. The theoretical rolling phenomenon formula also provides 0.66 for viscosity as seen in the chapter I.

The resistive torque is therefore divided by the viscosity to the power two third as reported in Equation *(2.8)* . A comparison of this new adapted resistive torque for both jet injection and bath lubrication is shown in Figure 2.9. The measurements show that the jet injection produces more resistive torque than the bath lubrication. This adaptation of the resistive torque enables a better comparison of the load-independent contribution in both experiments at different temperatures.

$$\overline{M_{adapted}} = \frac{M_{type\ A}}{\upsilon_{oil}^{2/3}} \qquad (2.8)$$

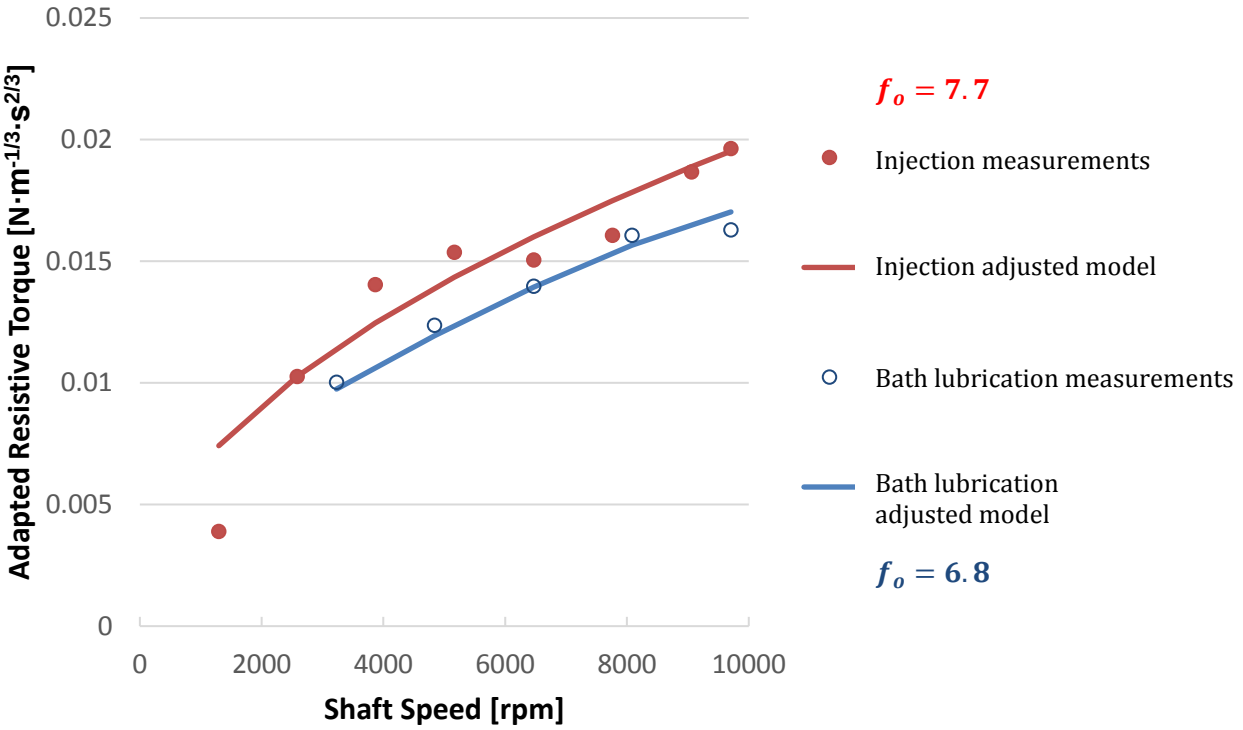

Figure 2.9 : Comparison of resistive torque between oil injection and bath lubrication for both measurements and adjusted model predictions

Type A Bearing; Serie 4 and bath lubrication; 500 N Radial Load

The adapted model for bath lubrication succeeds in predicting the resistive torque for the REB module. The best fit is found with $f_0 = 6.8$. This increase from bath to injection lubrication represents only 13% of the initial parameter. To recall, the original Harris-Palmgren model suggests an increase of 100% of the f_0 parameter (whatever the oil bath level). As a conclusion, the relationship in *(2.9)* is validated for Type A bearings for oil bath lubrication.

$$M_{0-bath} = 6.8 \cdot 4.5 * 10^3 \cdot \omega_i^{0.51} \cdot \upsilon^{2/3} \cdot d_m^3 \qquad (2.9)$$

2.4.3 Investigation on temperature influence

In the following, we aim at validating the assumption that the resistive torque depends only on the temperature *via* the viscosity with 2/3 as an exponent for the load-independent contribution. In this context, some tests are carried out in bath lubrication for the calibration module in heating phases. Bath lubrication is chosen as it is more precise than jet lubrication. Figure 2.10 represents the increase in resistive torque as the temperature increases and thus the viscosity decreases. The model with the power two third perfectly captures this evolution for medium to low viscosity [<54 cSt]. Only a small plateau appears at high viscosity (>54 cSt obtained from outer ring temperature lower than 20°C). The reason might be that a highly viscous oil is less inclined to replenish the ball tracks, generating less power loss due to oil inlet shearing.

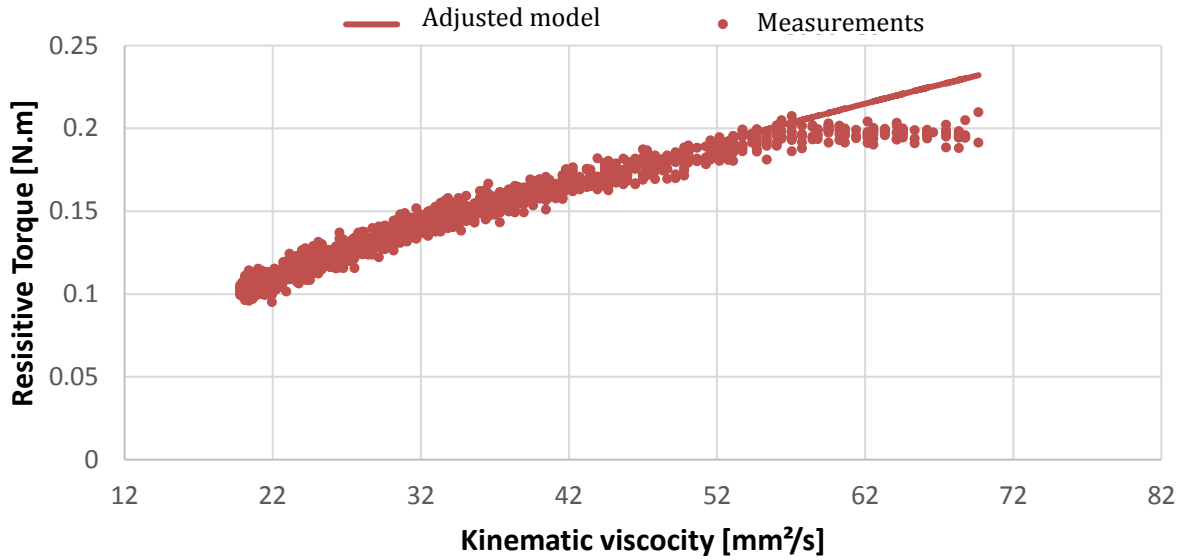

Figure 2.10 : Comparison of Resistive torque* versus *viscosity taken at the module outer ring temperature.

Type A Bearing; Bath lubrication; 6500 rpm; 500 N Radial Load

As a conclusion, the viscosity to the power two third seems to be a reasonable choice in the Harris-Palmgren Model (see Equation *(2.10)*)

$$M_{0-bath} = 6.8 \cdot 4.5 * 10^{3} \cdot \omega_i^{0.5097} \cdot \upsilon^{2/3} \cdot d_m^3 \qquad (2.10)$$

2.4.4 Investigation on load influence

In the previous sections, the load was kept relatively low and only the load-independent contribution was analysed. In order to investigate the influence of radial load on resistive torque, the calibration module is used for a new series of experiments in bath lubrication configuration. Three radial loads, [1000 ;3000 ;5000N], are applied. Each load is successively applied at five speeds from 3200 to 9700 rpm. Each test lasts for 20 minutes, and the temperature increases gradually.

In Figure 2.11, a comparison of the measured resistive torque is shown *versus* the radial load per REB for the series with a speed of 6500 rpm. On the graph, the outer ring temperatures are presented as a function of the radial load. Some of the experiments are selected to compare same-temperature data. The constant outer ring temperatures at a constant shaft speed justify the comparisons of the load dependent contribution with a constant load-independent contribution. The Harris-Palmgren model predicts a dependency of the resistive torque on the load with an exponent of 1.55. This dependency shows a good agreement with the experimental results once the *z* parameter is adjusted.

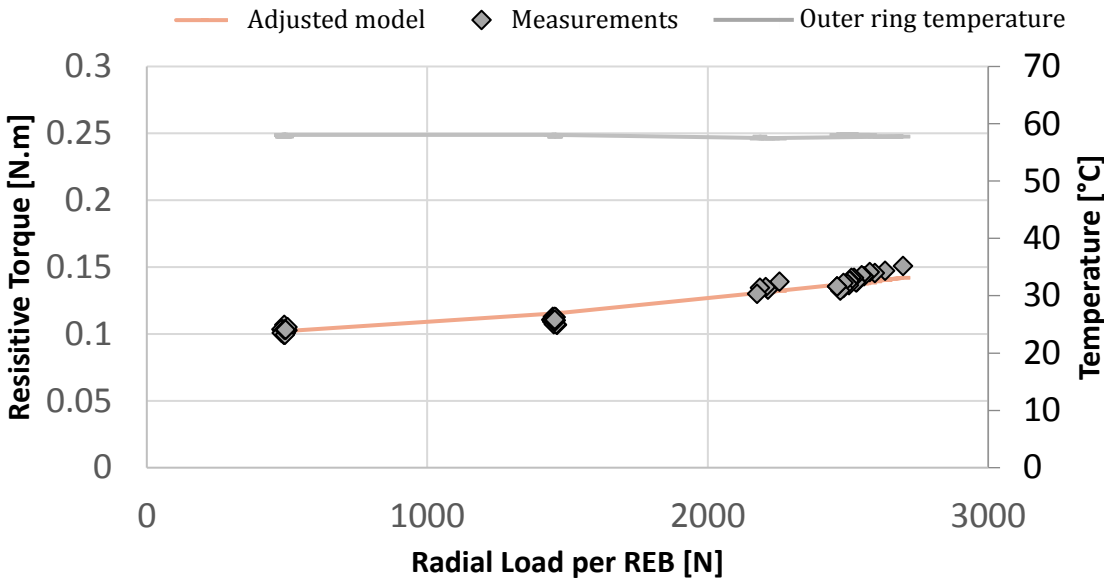

Figure 2.11 :Comparison of resistive torque* versus *radial load per REB

Type A Bearing; Bath lubrication; 6500 rpm

		Shaft Speed [rpm]				
		3200	4800	6500	8070	9700
Radial Load per REB [N]	500	1.78%	5.82%	1.35%	2.01%	3.41%
	1500	1.28%	7.38%	2.19%	2.72%	5.51%
	2500	5.25%	1.87%	1.80%	2.60%	2.07%

Table 2.10 : Mean relative error between model predictions and measurements [%]

The results of this experimental campaign are shown in Table 2.10. The model predictions agree with the measurements at all tested shaft speeds and applied loads. In general, the model predictions and measurements are less than 5% apart. As a conclusion, the modified Harris-Palmgren model, presented in Equation *(2.11)*, can adequately predict the evolution of resistive torque as the radial load increases. The influence of the load on the resistive torque in jet injection lubrication has not been investigated. A load-dependent contribution, independent from the lubrication design, is assumed.

$$M_1 = 5.8 \cdot 10^{-4} \cdot \left(\frac{F_r}{C_0}\right)^{0.55} \cdot F_r \cdot d_m \qquad (2.11)$$

2.4.5 Investigation on the influence of REB dimension

After investigating the resistive torque evolution of type A REB, the tested REB housing and its type B REB can be now investigated. The tested REB module has been lowly loaded and lubricated with the oil jet lubrication. This allows the comparison of the adjusted load-independent contribution of both REBs (type A REB adjusted model for injection being reported in *(2.7)*).

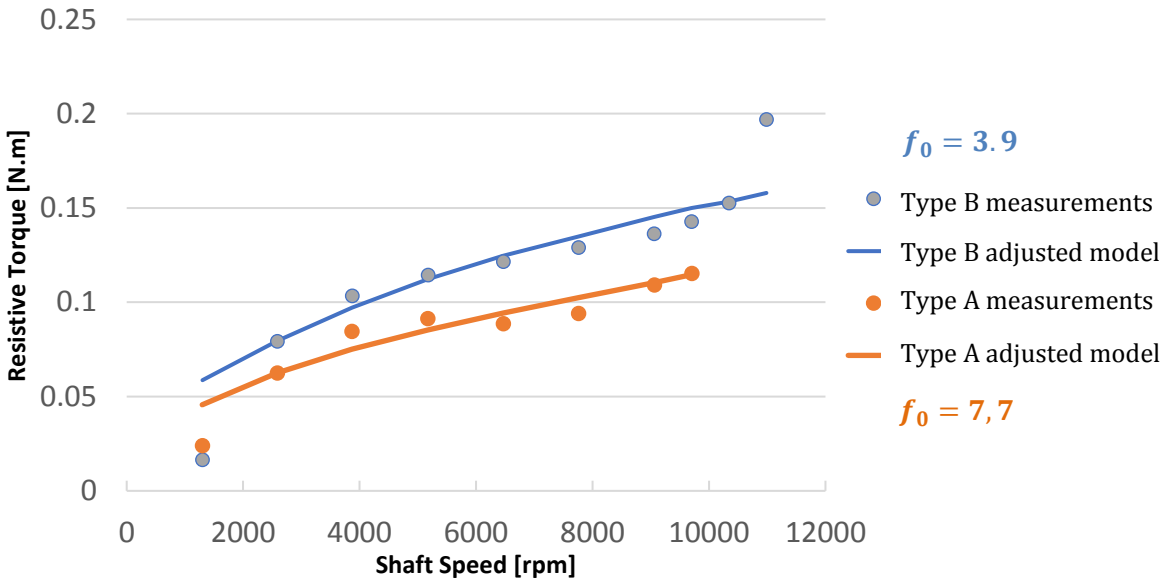

Figure 2.12 :Comparison of resistive torques for two REBs, experiments and adjusted model predictions

Type A: Oil Jet lubrication 70°C 12L/h; 600 N - Type B: Oil Jet lubrication 70°C 15L/h; 400 N

Concerning the measurements, it can be seen from Figure 2.12 that the type B bearing resistive torque evolution with speed is similar to the type A evolution. Eventually the Type B resistive torque drastically increases at high speed [11300 rpm]. This phenomenon has not been investigated since it happens after the maximum recommended speed of the Type B bearing. The similar evolution towards speed justifies a similar adjusted exponent over speed in the load-independent contribution. Yet the f_0 are indeed different with 7.7 for type A REB and 3.9 for type B REB.

In order to compare the influence of the dimensions on the resistive torque, one must first isolate it from all other parameters of influence. As said before, the focus here is on the load-independent contribution, thus the load is kept low for both bearings and its influence is neglected. The oil injection temperature is set to be 70°C for both bearings. On the other hand, isolating the experiments from the influence of oil flow rate is more challenging. Indeed, injecting the same amount of oil in bearings of different dimensions results in an unequal repartition of oil within the bearings. Hence, the churning mechanisms within the bearings may be influenced. Consequently, the larger type B REB should be tested with a higher oil flow rate. However, no method exist to quantify the ratio of oil flow rate ensuring a similar churning behaviour. The amount of empty space within both REB chambers is defined as the chamber volume. It is the sum of two lateral disks and of a central tore. The space occupied by the rolling elements must be subtracted. The chamber volume for both bearings are in fact similar, since one bearing has slightly larger rolling elements than the other as reported in Table 2.11. The hypothesis assuming that the oil flow rates (respectively 12 and 15 L/h for type A and type B REB) do not have any influence on the comparison between their dimensions is made here.

Name	Symbol	Type A	Type B
Bore Diameter [mm]	dm	61	85
Inner Ring Diameter [mm]	di	50	75
Outer Ring Diameter [mm]	de	72	95
Inner Raceway Diameter [mm]	dri	56.9	81.6
Outer Raceway diameter[mm]	dre	65.1	88.4
Ball Diameter [mm]	D	6.75	5.55
Width [mm]	B	12	10
Number of Ball [-]	Z	16	26
Tore Volume [mm³]	V_{Tore}	6858	6460
Disk Volume [mm³]	V_{Disks}	4125	4040
Ball Volume [mm³]	V_{Ball}	161	90
Total Chamber Volume [mm³]	V_{Total}	**8406**	**8173**

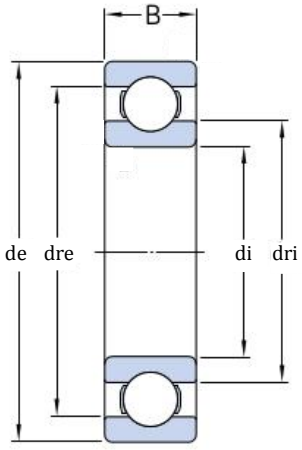

$$V_{Total} = V_{Tore} + V_{Disks} - Z \cdot V_{Ball}$$

Table 2.11 : Geometrical characteristics and chamber volume calculation for both bearings

In conclusion, the larger Type B bearing generates more heat than the smaller Type A bearing as seen on Figure 2.12. In the Harris-Palmgren model, the cube of the bore diameter takes into consideration the dimension of the REB. This assumption might be too significant since it prevents the use of a single f_0 parameter for both bearings. Instead, the f_0 parameter for the Type B bearing is nearly half the f_0 parameter for the Type A bearing.

2.4.6 Investigation on oil flow rate influence

In order to validate the oil flow rate hypothesis, the influence of oil flow rate on the Type B resistive torque is examined. Five shaft speeds from 1000 rpm to 12 000 rpm for three different oil flow rates [15; 25; 35 L/h] are investigated. In parallel, three oil injection temperatures [60;70;90°C] are tested for each oil flow rates.

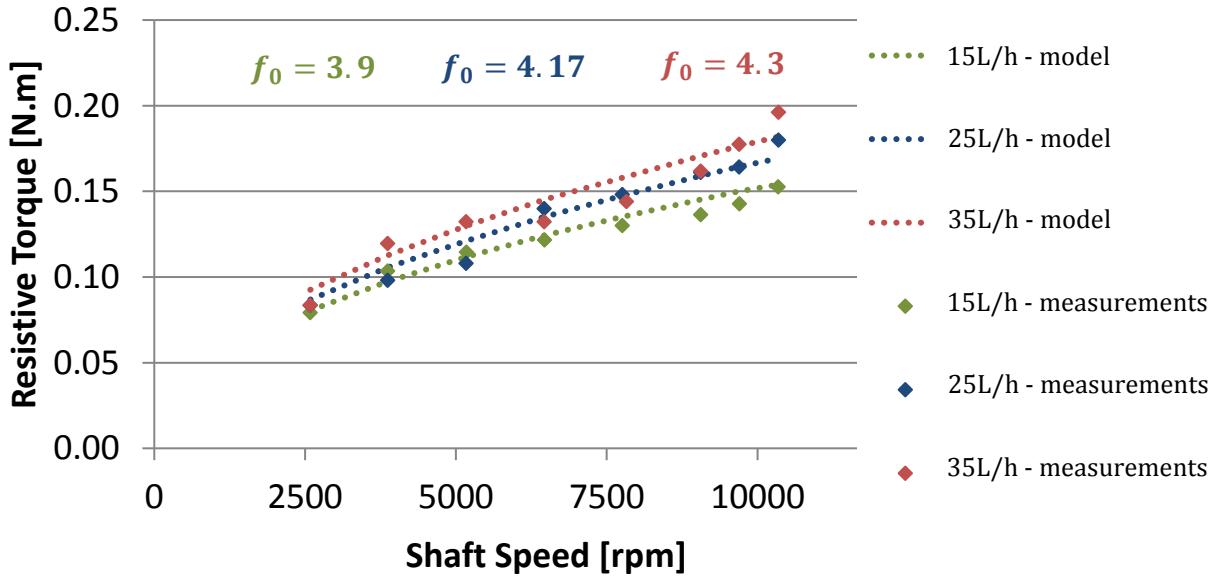

Figure 2.13 : Comparisons of resistive torque measurements and Harris-Palmgren model predictions versus shaft speed for three oil flow rates

Type B: Oil Jet lubrication 70°C injection temperature; 400 N

In Figure 2.13, some series of tests with different oil flow rates are shown for a constant oil injection temperature of 70°C. For shaft speed higher than 7500 rpm, the higher the oil flow rate, the higher is the resistive torque. Below 7500 rpm, some data points overlaps between the different the series. The influence of oil flow rate at low rotational speeds is small. The original model does not allow to estimate different resistive torques at different oil flow rates. The nearly constant outer ring temperature does not solely justify an evolution of resistive torque. The f_0 parameter is adjusted to fit each oil flow rate series as reported in the Figure 2.13.

One can notice that the influence of the oil flow rate on the resistive torque values is not crucial. In fact, when increasing the oil flow rate from 15 to 35 L/h, the f_0 parameter only increases by 10 %. This increase is equivalent to the f_0 increase of 13 % from oil bath lubrication to jet injection. However, it is significantly small compared to the f_0 increase of 97% from one bearing to the other. It can be concluded that the hypothesis of neglecting the influence of oil flow rate to compare the influence of REB dimensions is confirmed at 70°C.

2.4.7 Investigation on oil injection temperature influence

The influence of the oil injection temperature on type B REB is shown in this section. The 15L/h oil flow rate is presented in Figure 2.14 below at three different oil injection temperatures.

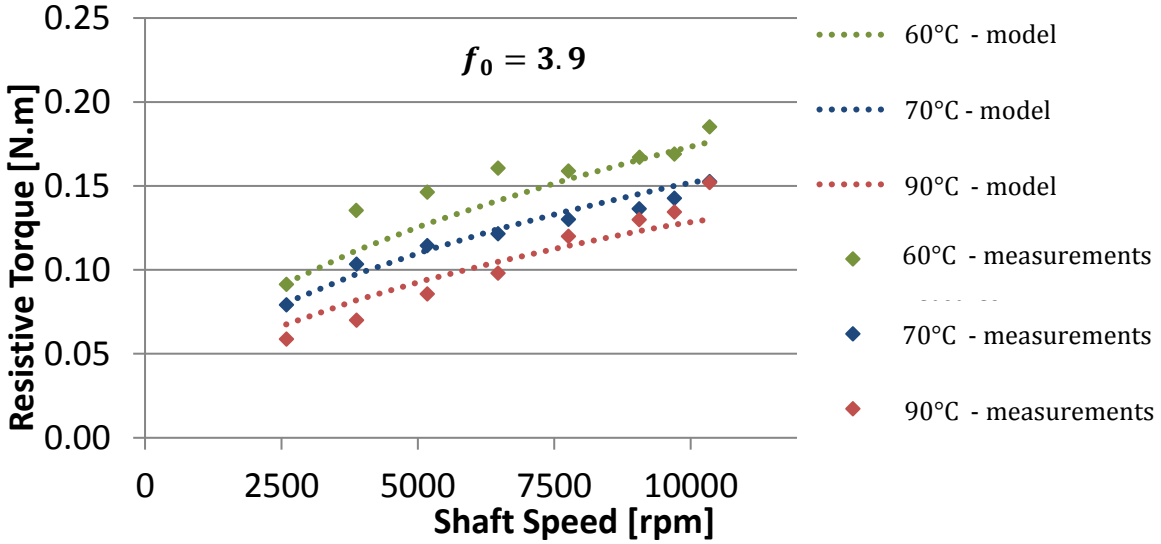

Figure 2.14 : Comparisons of resistive torque measurements and Harris-Palmgren model predictions* versus *shaft speed for three oil injection temperatures

Type B: Oil Jet lubrication 25L/h; 400 N

It can be seen on Figure 2.14 that the lower the injection temperature, the higher is the resistive torque, which is in agreement with the hypothesis that the viscosity is the principal temperature-related variable in REB resistive torque. The model with the viscosity to the power two third can successfully represent this evolution at this oil flow rate.

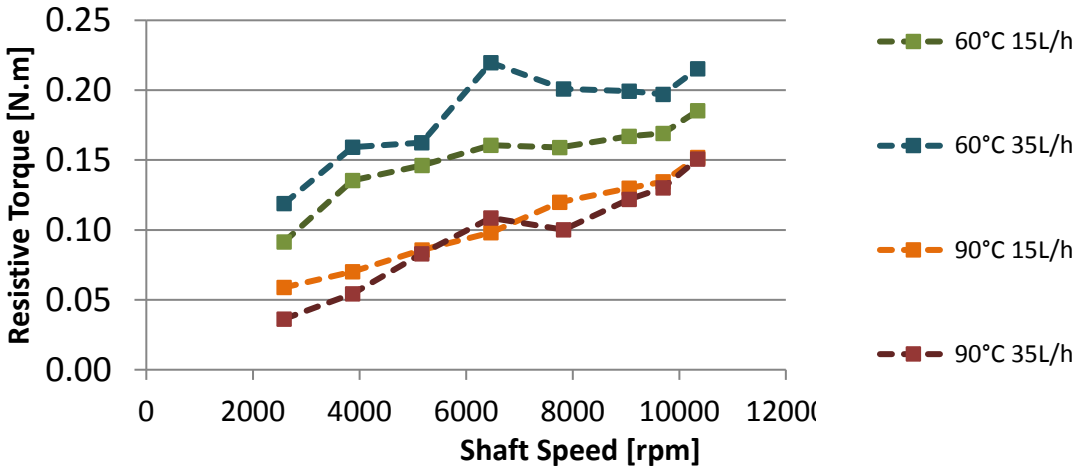

Figure 2.15 : Comparisons of resistive torque measurements for two oil flow rates and two oil injection temperatures

Type B: Oil Jet lubrication; 400 N

On Figure 2.15, the resistive torque obtained for two oil flow rate upper limits are compared at the two oil injection temperature upper limits. Concerning the influence of oil injection temperature, the 90°C oil injection measures are lower than the 60°C ones. This was already outlined in Figure 2.14.

Concerning the influence of oil flow rates, the 60°C 35L/h resistive torque measures are higher than the 60°C 15 L/h ones. This was already outlined at 70°C oil injection temperature on Figure 2.13. However, the difference between the two curves is greater than what was observed. In opposition, the influence of oil flow rate at 90°C and what was observed at 70°C are not alike. The 35 L/h curve more than overlaps the 15 L/h one. Both the influence of oil flow rates and oil injection temperature are therefore intertwined.

The oil injection temperature has an important influence on the REB resistive torque. Nevertheless, as reported previously and demonstrated by Niel [4]. the viscosity should be taken into consideration at the ring temperatures. The viscosity at the contact inlet depends on the solid bulk temperatures. A thermal equilibrium is reached between these solids and the oil inlet. The variation in the oil injection temperature affects this equilibrium, thus changing the bulk temperatures. Moreover, a change in oil flow rate influences the amount of calorie brought or removed by the oil injection. The colder the solids the more heat is produced *via* viscosity-dependent friction mechanisms, increasing in turn temperatures. This phenomenon, defined as thermal coupling, will be discussed in detail in the next chapter.

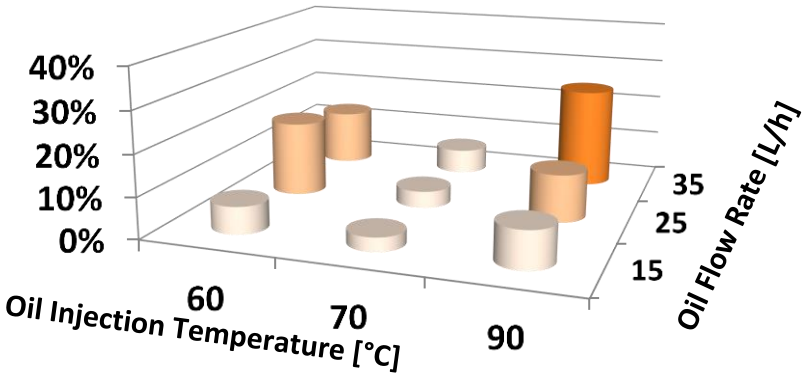

Figure 2.16 :Absolute relative errors between adjusted model and experiments

Type B: Oil Jet lubrication;400 N

To summarize this campaign on the Type B REB, Figure 2.16 presents the absolute relative error between the experiment and the adjusted model using the above-mentioned f_0 parameters fitted for each flow rates (respectively 3.9; 4.17; 4.3 for 15; 25; 35 L/h). In average, the relative error is 11%. Most experimental errors are below 10%. For the oil injection temperature series of 60 °C, the adjusted model underestimates the resistive torque by 13% for the two highest oil flow rates. For the oil injection temperature series of 90 °C, the adjusted model overestimates the resistive torque as high as 21% for the highest oil flow rate. A singe f_O parameter per oil flow rate will lead to inaccuracy as the influence of oil flow rate is linked to the oil injection temperature. Consequently, the adjusted Harris-Palmgren model can reasonably predict the resistive torque evolution towards speed and oil injection temperature for the type B low-loaded bearing. The evolution towards oil flow rates was achieved with more difficulty.

Bearing Type	Lubrification		Value
Type A	Bath Lubrication		**6.8**
	12 L/h	Jet Lubrication	**7.7**
Type B	15 L/h		**3.9**
	25 L/h		**4.17**
	35 L/h		**4.3**

Table 2.12 : Summery of f_0 for both type A and type B bearings under different lubrication designs

As a conclusion, the Harris-Palmgren model is easily adjustable for both tested REBs. The evolution towards speed requires an adaptation. The evolution towards viscosity, however, is in good agreement with the measurements for both bearing types. The evolution towards load is successfully implemented for the Type A bearing only. A change in the lubrication design have an influence on the resistive torque. A thermal dependence

between oil flow rates and temperatures is observed. Finally, a change in the dimensions of the bearing can double f_0 coefficient as reported in Table 2.12. The aim of a global model is to correctly predict heat productions without the need to test each REB. In this context, the dependency of Harris-Palmgren model on the bearing dimensions is a significant drawback. The thermal behaviour, that depends on jet lubrication characteristics, also brings interrogation towards the capacity of a single model to predict accurately resistive torque.

2.5 The SKF Model: results and discussion

In light of the previous section, the new SKF model has also been examined. The original model is composed of a rolling contribution, a sliding contribution, a drag contribution and a bath-lubrication churning contribution. This last contribution is negligible in jet-lubricated campaigns. Originally SKF model used the injection temperature for the calculation of the oil viscosity. Since then, the online model changed and now considers the average ring temperatures[12]. The evolution of the resistive torque as a function of the speed corresponding to the original model is presented in Figure 2.17 for lowly loaded type B REB.

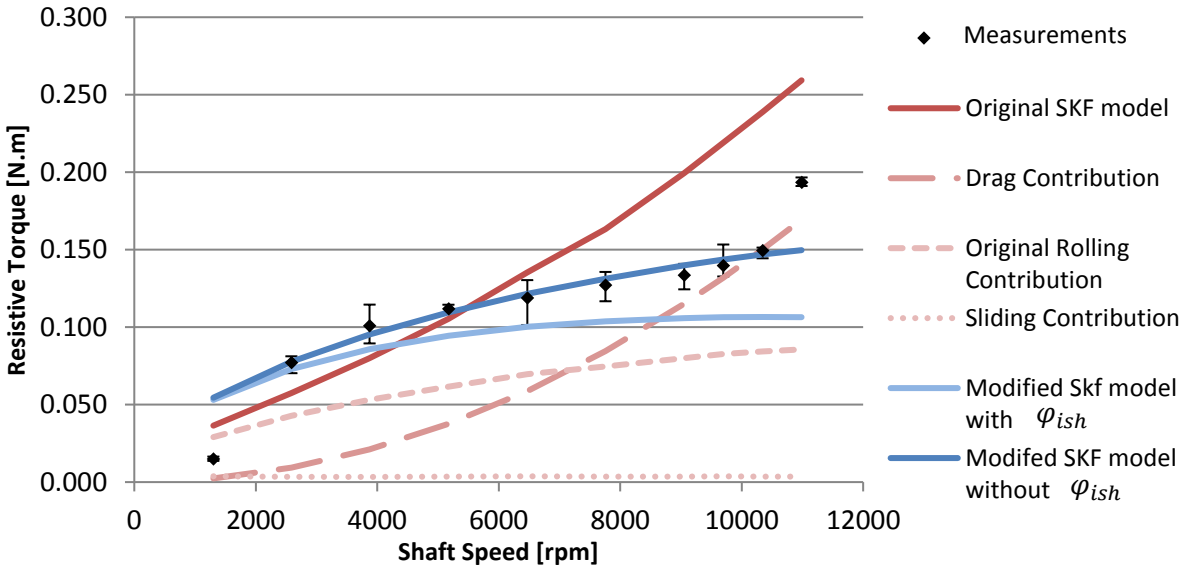

Figure 2.17 : Comparisons between original and adjusted SKF models

Type B: 70°C oil injection temperature; 15 L/h oil flow rate; 400N Radial Load

The original rolling contribution is low compared to the drag contribution since the original rolling contribution tends to zero when the REB is unloaded. The drag contribution evolution towards speed is to the power two. The original total torque evolution follows the drag contribution towards speed which is not realistic of measurements. Below the one million $N \cdot d_m$ criteria (11000 rpm for type B REB), the drag contribution should not be considered. At low load, the sliding contribution is negligible compared to both rolling and drag contributions.

In order to account for the fact that an unloaded REB still induces power losses, a minimal threshold has been applied to the radial load for the rolling contribution. This threshold is arbitrarily chosen at 10 % of the static load capacity of the concerned REB. The SKF model, including this threshold and excluding the drag contribution, is presented in Figure 2.17. The speed to the power two third in the rolling contribution, judged unrealistic previously, is here diminished by the presence of the replenishment factor φ_{rs}. The original model also includes a reduction factor φ_{ish} that supposedly accounts for temperature increases at the contact inlets. This factor was not considered in the present adjusted model as outer ring temperatures are considered sufficient to account for this phenomenon. The geometry constant R_1 has not been changed in the model used for the results presented in Figure 2.17. As can be seen in this figure, the SKF model with the reduction factor φ_{ish} underestimates the resistive torques; however best predictions are shown with the modified SKF model excluding φ_{ish}. This model will be used from now in our study. This modified model is presented below as the sum of equations *(2.12)* and *(2.13)*, where the modified parameter appears in red.

$$M_{sl} = 1.66 \cdot 10^{-4} \cdot (\varphi_{bl} \cdot \mu_{bl} + (1 - \varphi_{bl}) \cdot \mu_{EHL}) \cdot S_1 \cdot d_m^{-0.26} \cdot F_r^{5/3} \qquad (2.12)$$

$$M_{rr} = 1.17 \cdot 10^{7} \cdot \varphi_{rs} \cdot R_1 \cdot d_m^{1.96} \cdot F_{r_{threshold}}^{0.54} \cdot (v_{oil} \cdot \omega_i)^{0.6} \qquad (2.13)$$

The original parameters R_1 and S_1 depend on the deep groove ball bearing series. Table 2.13 presents their original values. The tested REB are from different series and therefore have different original parameters. The corresponding R_2 and S_2 parameters are only used for axial loads, which are not considered in this study.

Geometric constants for rolling and sliding frictional moments of deep groove ball bearings

Bearing series	Geometric constants for rolling frictional moments R_1	R_2	sliding frictional moments S_1	S_2
2, 3	$4{,}4 \times 10^{-7}$	1,7	$2{,}00 \times 10^{-3}$	100
42, 43	$5{,}4 \times 10^{-7}$	0,96	$3{,}00 \times 10^{-3}$	40
60, 630	$4{,}1 \times 10^{-7}$	1,7	$3{,}73 \times 10^{-3}$	14,6
62, 622	$3{,}9 \times 10^{-7}$	1,7	$3{,}23 \times 10^{-3}$	36,5
63, 623	$3{,}7 \times 10^{-7}$	1,7	$2{,}84 \times 10^{-3}$	92,8
64	$3{,}6 \times 10^{-7}$	1,7	$2{,}43 \times 10^{-3}$	198
160, 161	$4{,}3 \times 10^{-7}$	1,7	$4{,}63 \times 10^{-3}$	4,25
617, 618, 628, 637, 638	$4{,}7 \times 10^{-7}$	1,7	$6{,}50 \times 10^{-3}$	0,78
619, 639	$4{,}3 \times 10^{-7}$	1,7	$4{,}75 \times 10^{-3}$	3,6

Type B → 617, 618, 628, 637, 638

Type A → 619, 639

Table 2.13 : Deep Groove Ball Bearing original geometric constants for the SKF model [12]

As it has been seen in the previous section, a change in the lubrication design has a small influence on the adjusted parameter for the load-independent contribution (13% increase from bath lubrication to jet lubrication). The bath-lubricated contribution in SKF model can only bring an additional increase in the resistive torque, which contradicts this

result. Although the comparison between the two different REB operating under jet lubrication requires a relevant oil flow rate ratio, it has been shown that the oil flow rate has a minimal influence on the adjusted f_0 parameter at 70°C. Therefore, the influence of oil flow rate is not investigated in this present section. In the following, both bearings with respectively 12 L/h and 15 L/h are again used in the comparison.

2.5.1 Investigation on the influence of REB dimension

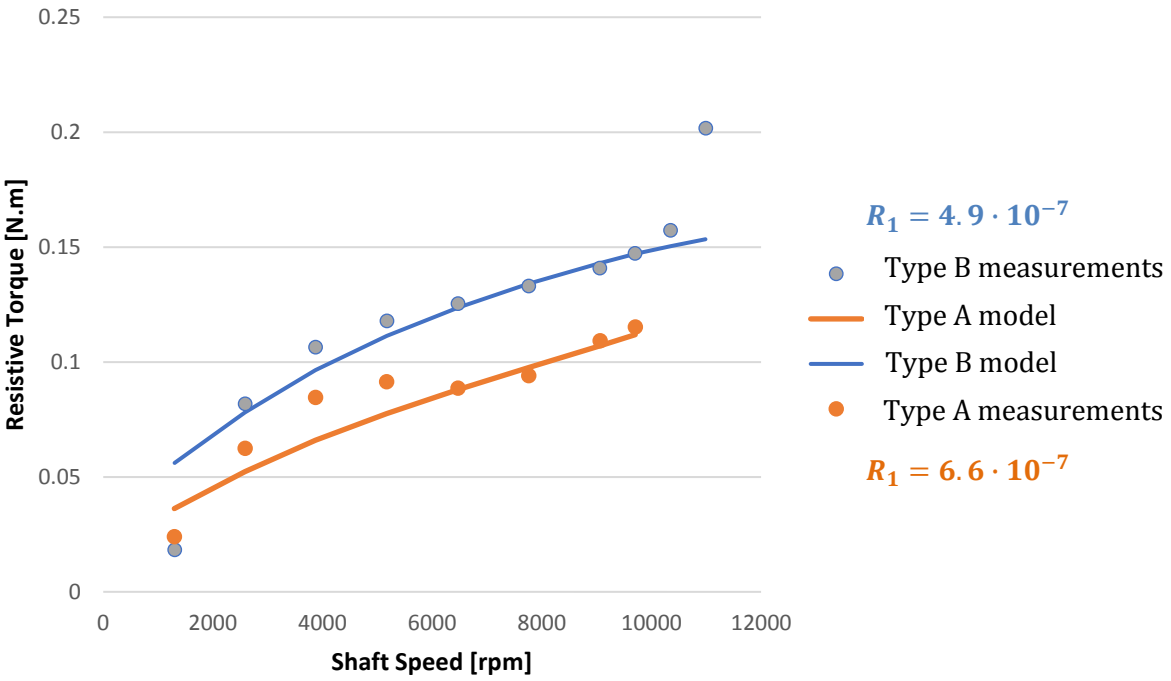

Figure 2.18 : Comparison of resistive torque for two REB, experiments and SKF model

Type A: Oil Jet lubrication 70°C 12L/h; 600 N

Type B: Oil Jet lubrication 70°C 15L/h; 400 N

Recalling the previous result on the dimension comparisons between Type A and Type B REBs, it can be seen in Figure 2.18 that the SKF model also needs different coefficients in order to fit both REB curves. The original R_1 parameter for type B REB is close to the adjusted parameter (respectively $4.7 \cdot 10^{-7}$ and $4.9 \cdot 10^{-7}$). On the other hand, the type A REB R_1 parameter is adapted from $4.3 \cdot 10^{-7}$ to $6.6 \cdot 10^{-7}$. The original parameters follow the inverse trend compared to the adjusted parameters.

Bearing Type	Lubrification	Value
Type A	12 L/h Jet Lubrication	$6.6 \cdot 10^{-7}$
Type B	15 L/h Jet Lubrication	$4.9 \cdot 10^{-7}$

Table 2.14 : R_1 adjusted parameters for both tested REBs

Additionally, the adjusted parameter R_1 for type A REB is 34% higher than type B REB one as reported in Table 2.14. The difference between the adjusted parameter R_1 for type A and B REBs is less important then what has been obtained by the Harris-Palmgren model where it is doubled. This is due to the fact that the bore diameter is taken with a smaller exponent in the rolling contribution compared to the Harris-Palmgren load-independent contribution.

2.5.2 Investigation on the load influence

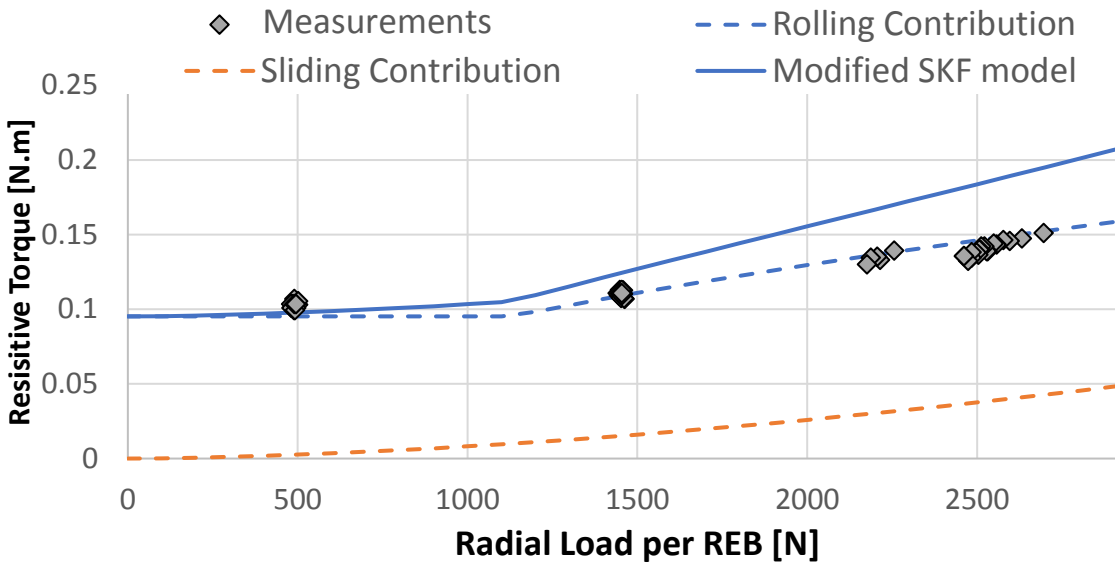

Figure 2.19 :Comparison of resistive torque* versus *radial load per REB

Type A Bearing; Bath lubrication; 6500 rpm

The comparison between the measurements and model prediction *versus* radial load is presented in Figure 2.19. Contrary to the Harris-Palmgren model, the SKF model fails to fit the evolution of the resistive torque versus an increase in applied loads. Although the sliding contribution possesses similar features compared to the Harris-Palmgren load-dependent contribution (exponent 1.66 against 1.55 over the applied load), the rolling contribution also depends on the radial load with an exponent 0.54. This combined dependency on radial load overestimates the evolution of resistive torque. Therefore, either the rolling contribution should be load-independent, or the sliding contribution should be neglected. Both solutions are presented in Figure 2.20 below.

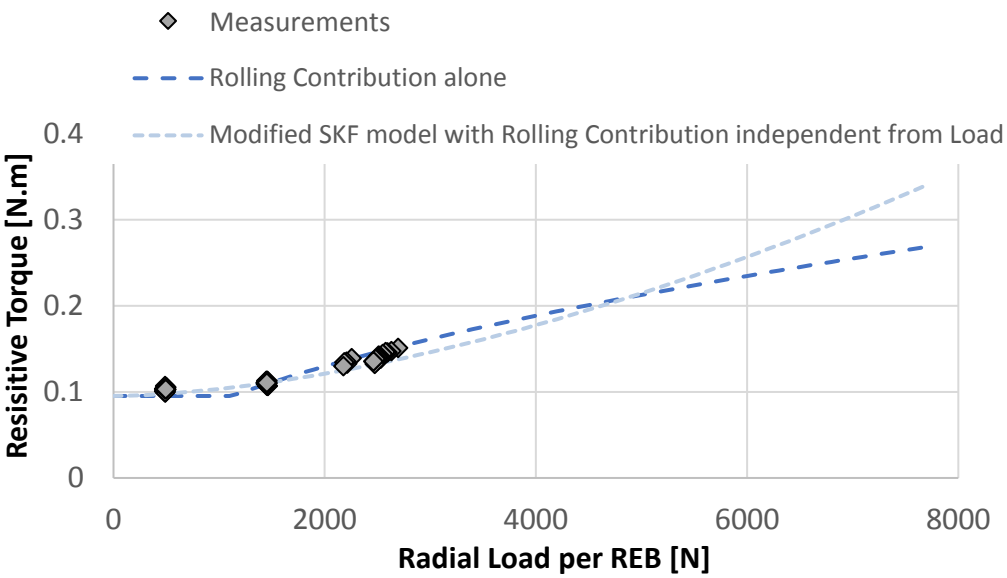

Figure 2.20 :Expectation of resistive torque versus radial load per REB

Type A Bearing; Bath lubrication; 6500 rpm

As it can be seen in Figure 2.20, both solutions are found satisfying enough for a broad range of radial loads. Significant differences between the two solutions are only observed at a radial load higher than 6000 N, which is over 50% of the static load capacity of Type A REB. Contrary to the Harris-Palmgren model that separates two empirical entities, SKF model is allegedly proposed in order to represent physical phenomena. The sliding contribution integrates a lubrication regime partition from mixed lubrication regime to EHL regime. This feature is not investigated in the present study as the EHL regime has been reached in all experiments. Nevertheless, the difference between these two solutions should only be seen at low speed and high load dedicated experiments.

The evolution of resistive torque towards load has only be assessed for type A REB. The impact of REB dimension on this contribution has not been investigated. It can be observed that the Harris-Palmgren load-dependent contribution depends linearly on the REB bore diameter, while the sliding contribution is proportional to the diameter to the power -0.26 for deep groove ball bearing. In fact, depending on the bearing types, the exponent can either be positive or negative. In light of this discrepancy, the load-dependent rolling contribution alone is considered hereafter.

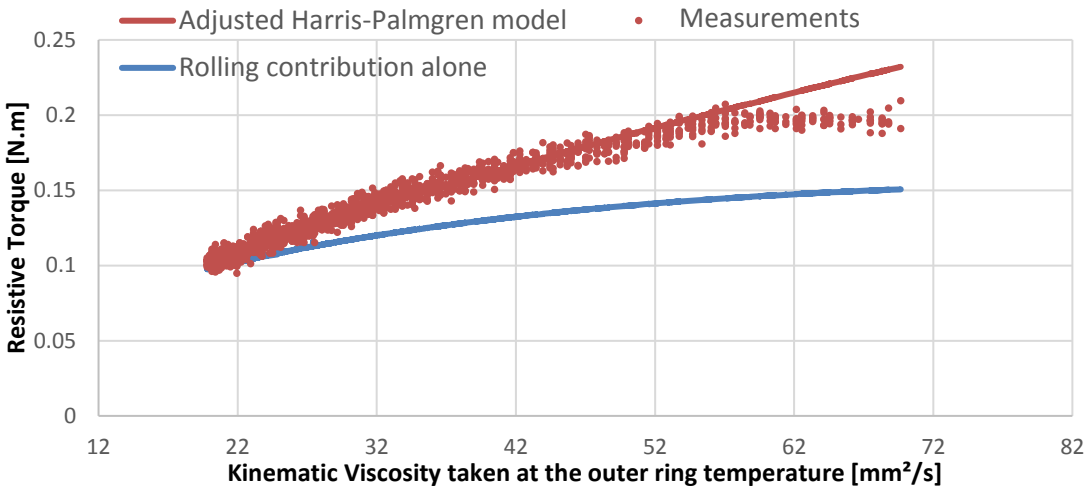

Figure 2.21 : Comparison of the adjusted Harris-Palmgren model and the SKF model towards viscosity

Type A Bearing; Bath lubrication; 6500 rpm; 500 N Radial Load

In Figure 2.21, the comparison of the evolution of the resistive torque corresponding to the rolling contribution of the SKF model, the previously adjusted Harris-Palmgren model, and the measurements is shown versus the kinematic viscosity at the outer ring temperature. It can be seen that if the rolling contribution is successfully adjusted at high temperature (>50°C), it progressively underestimates the resistive torque. Indeed, the addition of a replenishment reduction factor damps the influence of viscosity compared to the Harris-Palmgren model. However, it may be more adequate to predict the plateau observed at high viscosity. An adaptation of this reduction factor should be investigated in order to enhance the SKF model.

		Shaft Speed [rpm]				
		3200	4800	6500	8070	9700
Radial Applied Load [N]	1000	15.57%	23.28%	9.09%	2.75%	2.18%
	3000	13.69%	-6.20%	0.30%	5.68%	-13.66%
	5000	12.30%	-4.20%	-10.05%	-14.81%	-16.08%

Table 2.15 : Mean relative error between the SKF rolling contribution alone and measurements [%]

Nevertheless, this damping effect on resistive torque at low temperature leads to underestimate the resistive torque at low speed and low load for bath-lubricated experimental series. In Table 2.11, the mean relative error between the rolling contribution and the measurements highlights this fact. On the other hand, the rolling contribution overestimates the resistive torque at high speed and high load cases. The total relative error is only 1.3% but the error can increase as high as 23%.

2.5.3 Investigation on oil injection temperature influence

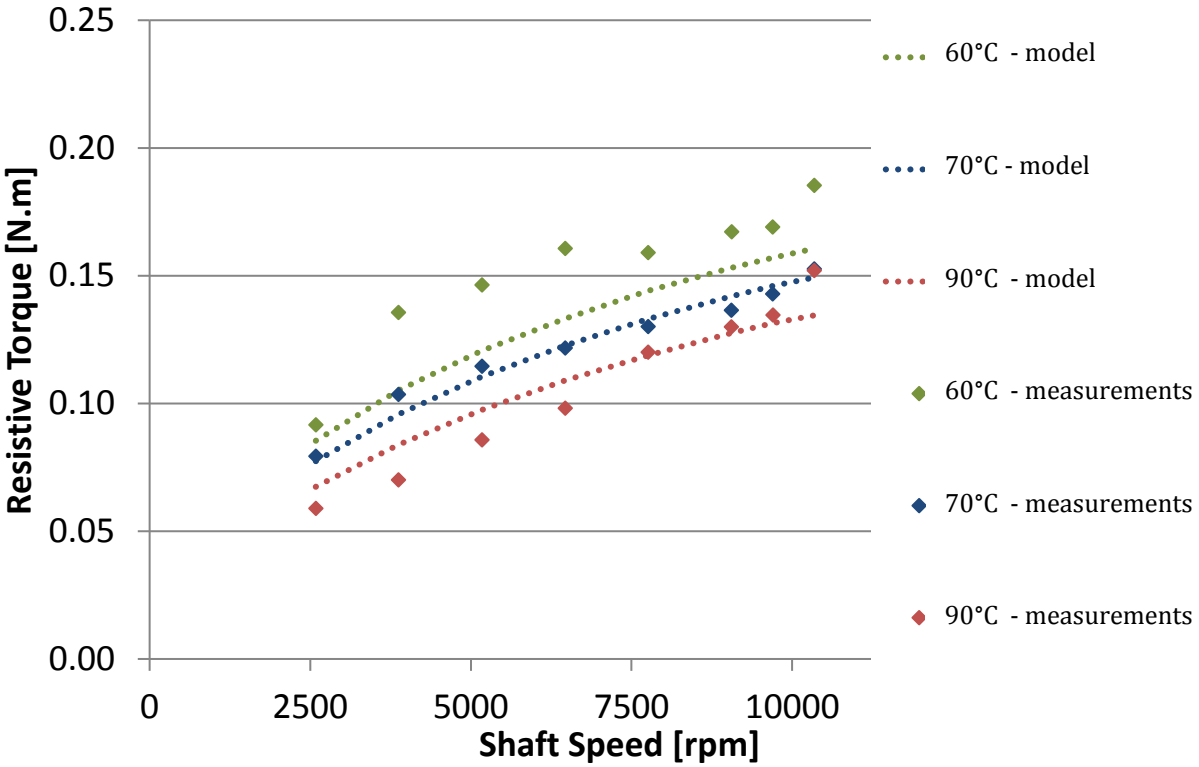

Figure 2.22 : Comparisons of resistive torque measurements and the SKF rolling contribution versus shaft speed for three oil injection temperatures

Type B: Oil Jet lubrication 15L/h; 400 N

Figure 2.22 compares the adjusted rolling contribution predictions and torque measurements for three oil injection temperatures at an oil flow rate of 15L/h. Similarly to the Harris-Palmgren model comparisons (Figure 2.14), the adjusted SKF model sorts the resistive torque depending on the injection temperature. The 70°C and 90°C model predictions are close to the experiments. The 60°C model prediction is too low compared to the experiments as the reduction factor φ_{rs} reduces the influence of a high viscosity. Compared to the Harris-Palmgren model comparisons, the adjusted SKF model therefore underpredicts the resistive torque at low temperature.

As a conclusion, SKF model is adjustable for both tested REB to a certain extent. The evolution of torque towards speed is already in agreement with measurements thanks to a replenishment damping parameter. However, the evolution towards viscosity fails to predict the resistive torque at low temperature due to this parameter. The evolution towards load is hard to model as both the rolling and the sliding contributions compete to explain its evolution. The comparison between bath lubrication and jet injection is not made here. The presence of an additional splash contribution in the model is not realistic as the injection generate more heat than the bath lubrication (for the tested bath level and oil flow rates)

The evolution of torque versus oil flow rates have not been investigated here. Finally, a change in the bearing dimension can increase the f_0 parameter by 34% as reported in ***Table*** 2.14. This difference in f_0 parameter is smaller than that obtained for the adjusted Harris-Palmgren model.

2.6 Conclusion and discussion

To summarize, a new set of measurements is carried out using a dedicated test rig in order to compare the global power loss models on two different deep groove ball bearings. The first REB is tested under jet lubrication and bath lubrication. The influence of radial load is assessed for this REB. The second REB is tested under jet lubrication. The influence of the oil injection temperatures and oil flow rates are investigated. For both REBs, Harris-Palmgren parameters are adjusted to fit the experiments. In addition, the SKF adjusted model is also compared to the experiments for both bearings.

Both the two modified models reasonably predict the evolution of the torque *versus* speed. Concerning the evolution towards viscosity, both models succeed in predicting resistive torque, even though the SKF replenishment factor damping effect is too strong to predict the observed plateau at low temperature. The viscosity at the power two third is valid for a wide range of temperatures. Concerning the influence of load, the Harris-Palmgren model provides better results than the SKF model. The Harris-Palmgren can indeed be more easily adjusted. The SKF model evolution towards load is too steep when both the rolling and sliding contributions are included. The impact of load is only tested on type A REB and should be evaluated for the type B REB in a future dedicate campaign.

Concerning the change in the REB dimensions, the adjusted Harris-Palmgren model coefficients vary from one REB to the other. The adjusted f_0 parameter is divided by two for the smaller REB compared to the larger REB. The cube diameter in the original formulation might be a strong consideration for the dimension. Similarly, the SKF adjusted R_1 parameter is increased by 34% from the larger REB to the smaller one. Additionally, the impact of the oil flow rates depends on the oil injection temperature. The models do not take oil flow rate into account. Between 60 and 90 °C oil injection temperature, the use a single f_0 parameter fitted per oil flow rate leads to inaccuracies in the order of a dozen percent.

The inner ring temperature can be subtracted by the outer ring temperature to provide an additional information. On Figure 2.23, the ring temperature difference are presented at two oil flow rates and two oil injection temperatures for type B REB.

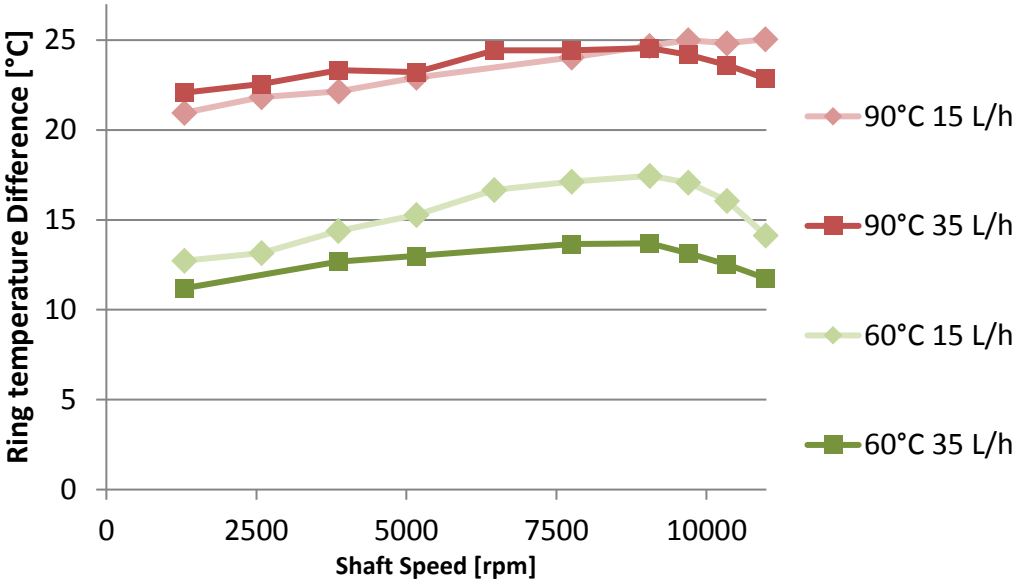

Figure 2.23 : Comparisons of ring temperature difference under different oil injection temperatures and oil flow rates

Type B REB; Oil Jet lubrication 400 N

It is observed on Figure 2.23 that at low oil injection temperature (60°C), a higher oil flow rate induces a lower ring temperature difference. The heat exchange between both rings and the injected oil therefore depends on the oil flow rates. Thus, at low oil injection temperature, a higher oil flow rate brings the temperatures of the inner and outer rings closer. It can be assessed that convective heat exchanges within the REB are enhanced by an increase in oil flow rate.

However, at high oil injection temperature (90°C), the oil flow rate has less influence on temperature difference. At low oil flow rate, the inner ring is more isolated than the outer ring. Increasing the oil flow rate increase its capacity to exchange heat. In the meantime, the inner ring temperature rises as the injected oil conveys more heat. If the heat exchange increases with oil flow rate, the inner ring is still struggling to cool off, which brings balance to the temperature difference.

Therefore, the change in lubrication has an influence on the inner and outer rings temperature difference. All the present modelled results use the outer ring temperature to evaluate the viscosity. Because the temperature difference depends on the lubrication characteristics, both rings temperature should be taken into consideration into the calculation of an equivalent viscosity. The evolution of the temperature differences of the inner and outer rings may be the reason of f_0 parameter depends on the lubrication design.

As a conclusion, the application of the global model using the outer ring temperature to compute the viscosity is beneficial for most experiments. However, to enable a closer understanding of how lubrication influences the resistive torque, the inner

ring temperature should also be considered. This problematic will lead to the thermal considerations in the next chapter. Furthermore, the present study highlights that experiments are required for each bearing prior to apply a model. A method to predict power losses for different REBs is required in order to apply the Harris-Palmgren model as an universal approach.

Chapter 3:
Thermal Model

3.1 Introduction

As seen in the previous chapter, the REB power loss depends on lubrication characteristics and REB geometry. In order to analyse these influences on power losses, a thermal model of the REB must be created. In order to build such a model, the oil heat transfer within the bearing must be modelled. The following section aims at introducing two major parameters of influence: the penetration ratio and the oil volume fraction.

Afterwards, the thermal network method is presented in light of the literature and a thermal network is implemented on the present test rig. The thermal behaviour of the REB is discussed and compared to dedicated experiments.

Finally, having a new model capable of predicting inner ring temperatures, a set of simulation is generated to emphasis the influence of lubrication on the resistive torque. Ultimately, the two REB previously presented will be examined in order to justify if a single model can accurately predict their resistive torques.

3.2 Lubrication

3.2.1 Lubrication

The lubrication has diverse roles: lubricating the surfaces, removing any kind of pollution and cooling the mechanical components. The REB chamber is defined as the volume between the two rings where the rolling elements and the cage evolve. This volume can be more or less filled with lubricant. Different types of lubrication exist: grease, oil mist, oil bath or oil injection.

3.2.2 Types of lubrication

The most efficient lubrication in that manner is injecting cooled-off oil, either through nozzles or through holes in the inner raceway. At high rotational speed, split inner raceway lubrication is preferred due to centrifugal effect [77]. However complex design makes it sometimes impossible. Both jet and split-inner ring methods are found in the main gearboxes of helicopters nowadays, usually with different cooling circuits for redundancy. An alternative lubrication method is oil-mist lubrication where the lubricant is pulverized through sprinklers. Pinel compared it to classical jet lubrication to study its influence on power losses, bearing temperatures and lifetime expectancy [78]. In another matter, greased and bath-lubricated REBs are subject to pollution-related failure modes. The capacity to remove heat is also consequently diminished due to the absence of a cooling device. For practical reasons bath-lubricated REBs can yet be found at the tail gearboxes of helicopter.

Considering oil jet lubrication, the rolling element motion modifies the jet trajectory. Only a portion of the injected oil flow $\dot{D}_{inj}$ actually enters the bearing as seen in Figure 3.1, the rest is deflected towards the housing interiors. The ratio of entering versus

injected oil flow rate is called the penetration ratio and is noted α. This ratio therefore leads to equations *(3.1)* and *(3.2)* to quantify the above-mentioned oil flow rates:

$$\dot{D}_{transmitted} = \alpha \cdot \dot{D}_{inj} \tag{3.1}$$

$$\dot{D}_{deflected} = (1 - \alpha) \cdot \dot{D}_{inj} \tag{3.2}$$

Miyakawa showed the influence of nozzle direction and bearing technologies on the penetration ratio [16]. He also pointed out the penetration ratio dependence on the shaft speed, the oil flow rate and on even the axial load as it changes the contact angle and the bearing internal kinematics. In order to estimate the penetration ratio on the present test rig, a dedicated campaign was conducted.

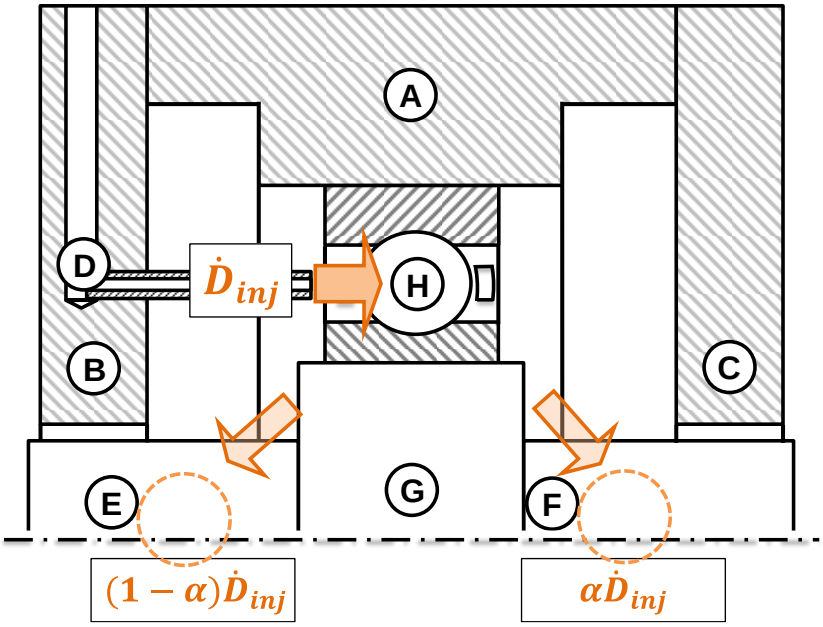

Figure 3.1: Scheme of the penetration mechanism

3.2.3 Measurements of penetration ratio

The penetration ratio is investigated on the test rig integrating type B REB. The transmitted oil outlet is connected to a beaker which is progressively weighted. The data is collected every minute for five minutes at each speed. Both oil outlets were also successively weighted to ensure that the sum of the corresponding oil flow rates is equal to the injected one. Several values of injected oil flow rate were tested for two oil injection temperatures (60 and 70°C). For these operating conditions, the oil jet velocity varies from 5.3 m/s (15L/h) to 12.3 m/s (35 L/h). It can be seen on Figure 3.2 that oil injection temperatures (60 and 70C) do not seem to influence significantly the penetration ratio, whereas it increases with the oil flow rate. For both oil flow rates, the oil struggles to enter the bearing as the shaft speed increases. At low speed and high oil flow rate, the penetration ratio is above 50% which indicates that the jet velocity is high enough to enable most of the oil to cross the REB. The lowest value of 20% is obtained for the lowest

flow rate at the highest speed. The 20L/h oil flow rate measures were averaged in temperature in order to emphasis the evolution of penetration towards speed.

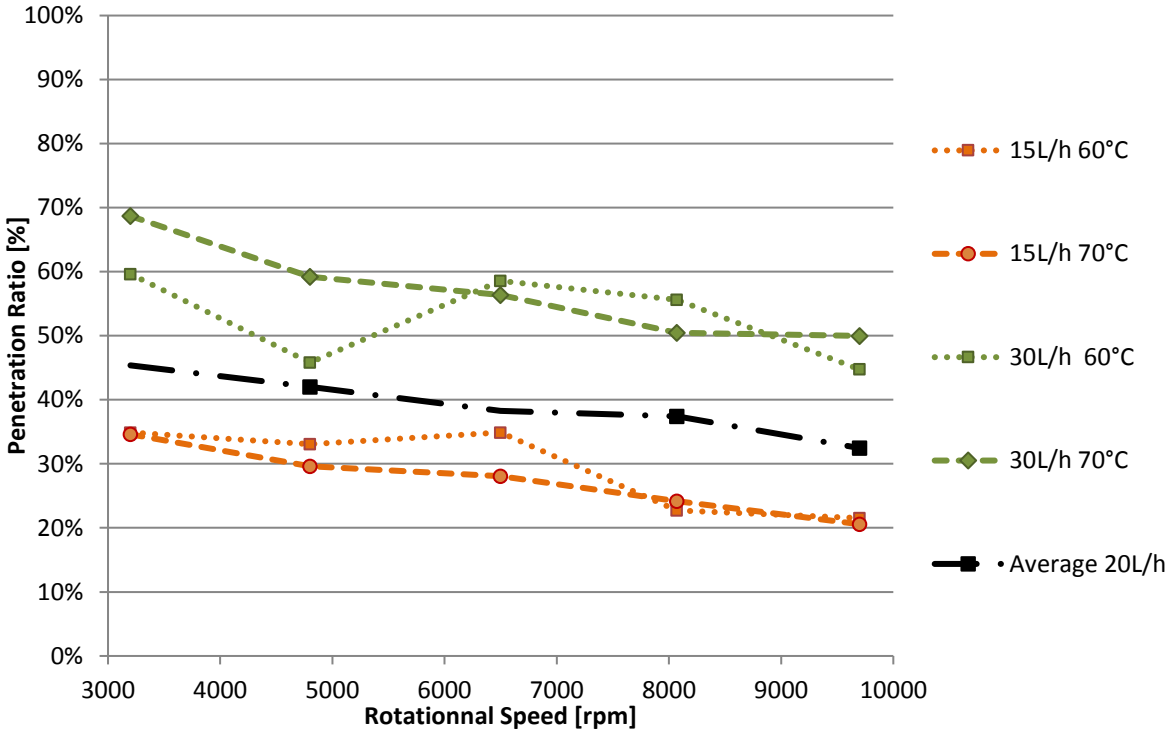

Figure 3.2 : Evolution of penetration ratio versus speed at different oil injection temperatures and oil flow rates

With new measurements of penetration ratio at hand, oil heat transfer mechanisms can be investigated. The REB temperature is dependent on its surrounding environment, the housing of the tested module here. A thermal model is therefore required to enable a closer understanding of the interaction between the REB rings and the oil in order to analyse the potential thermal influence of oil flow rate on power losses.

3.3 Thermal Network

Thermal model analysis, either through nodal approach or by Finite Element Analysis (FEA), at first studied components, such as gears and bearings, isolated from their gearboxes [79,80]. However, temperature distribution within a system is always dependent on the boundary conditions applied to the studied system. Therefore, local thermal models are only relevant if included in a more overall model where the boundary conditions are known or measured. Such a complete approach of a whole transmission system was made by Roulet on a whole automobile gearbox [81]. Because heat productions are dependent on the lubricant properties, themselves dependent on the lubricant temperature, an iterative approach is compulsory [82]. If FEA describes more accurately the conduction in complex 3D solids, it requires some kind of 1D interface to account for more complex heat transfer such as convection or contact between components. Conversely, Computational Fluid Mechanics (CFD) have been used to model thermal heat exchange through fluid within a REB [57,58,60]. It has also required the

analytical parametrisation of the fluid-solid interfaces. To the author's knowledge, no coupled FEA-CFD model has been made to compute simultaneously the conduction through solids and convection through fluids. A nodal network is an efficient method to model this multi-physics thermal behaviour. The considered system is made of nodes assumed isothermal. The boundaries between the system and the outside environment is made of nodes called limit nodes. Applying the first principle of thermodynamics for transient conditions to each node leads to equation (3.3).

$$I_j \frac{dT_j}{dt} = P_j + \sum_{k=1}^{n} \frac{T_j - T_k}{R_{j-k}} \tag{3.3}$$

The $I_j \frac{dT_j}{dt}$ term represents the internal energy rate of variation. The limit nodes are considered to have an infinite inertia and act as heat sinks. The P_j terms represents the power losses generated at the j^{th} node. If it is negative, it represents the heat leaving the system at the limit nodes. The term $\frac{T_j - T_k}{R_{j-k}}$ represents the heat exchange between the j^{th} node and another one which are connected through a thermal resistance (R_{j-k}). This system of equations can be solved by an explicit Adams algorithm [82]. Several studies which use the thermal network approach can be found in the literature [19,82–88].

Concerning the specific study of REB thermal behaviour, Harris disclosed a thermal model of REB which modelized each contact temperature [79]. Hannon used an analytical model to compute temperature distribution for tapered roller bearing [89]. Pouly conceived a jet engine angular ball bearing using a seven nodes network [71]. The contacts between balls and rings are modelled. The angular ball bearing under axial load being axially symmetrical, only one pattern of rolling element is modelled and summarized to the entire REB. Each power loss contribution is injected in the appropriate node (the outer and inner contacts, the oil-air mixture for the drag force and the cage interactions). In order to extend Pouly's model to the study of a REB under radial load, Neurouth first established an eight nodes network for a REB, enabling to dissociate a lower outer ring part in contact with loaded balls from a upper one with unloaded contacts. He modelled then a four-nodes thermal network with only inner ring, outer ring, central node and oil mist. This model is presented in Figure 3.3. Little differences between the two models were found in terms of inner ring and outer ring temperatures. It also enables a simpler calculation of power loss where the overall value is calculated and inserted in a single virtual node, here labelled #3 [90]. Niel developed a method to apply this model on any bearing without knowing its detailed geometry [88].

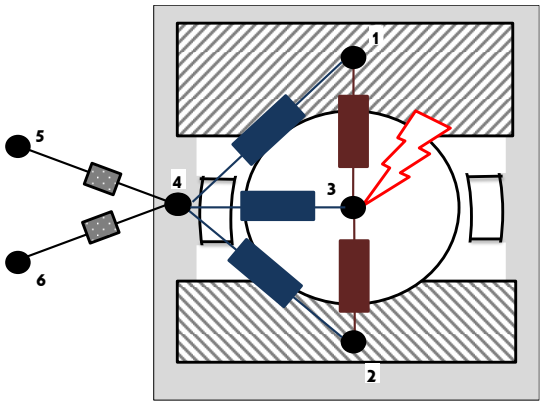

Node	N°
Outer Ring	1
Inner Ring	2
Central Node	3
Oil Mist	4
Oil Injection	5
Oil Outlet	6

Figure 3.3 : 4 Nodes REB Thermal Network Scheme

3.4 Test Rig Thermal Network Analysis

3.4.1 Presentation of the analytical model

The REB four nodes model was inserted in a larger network modelling the tested module housing thermal behaviour which can be seen in Figure 3.4.

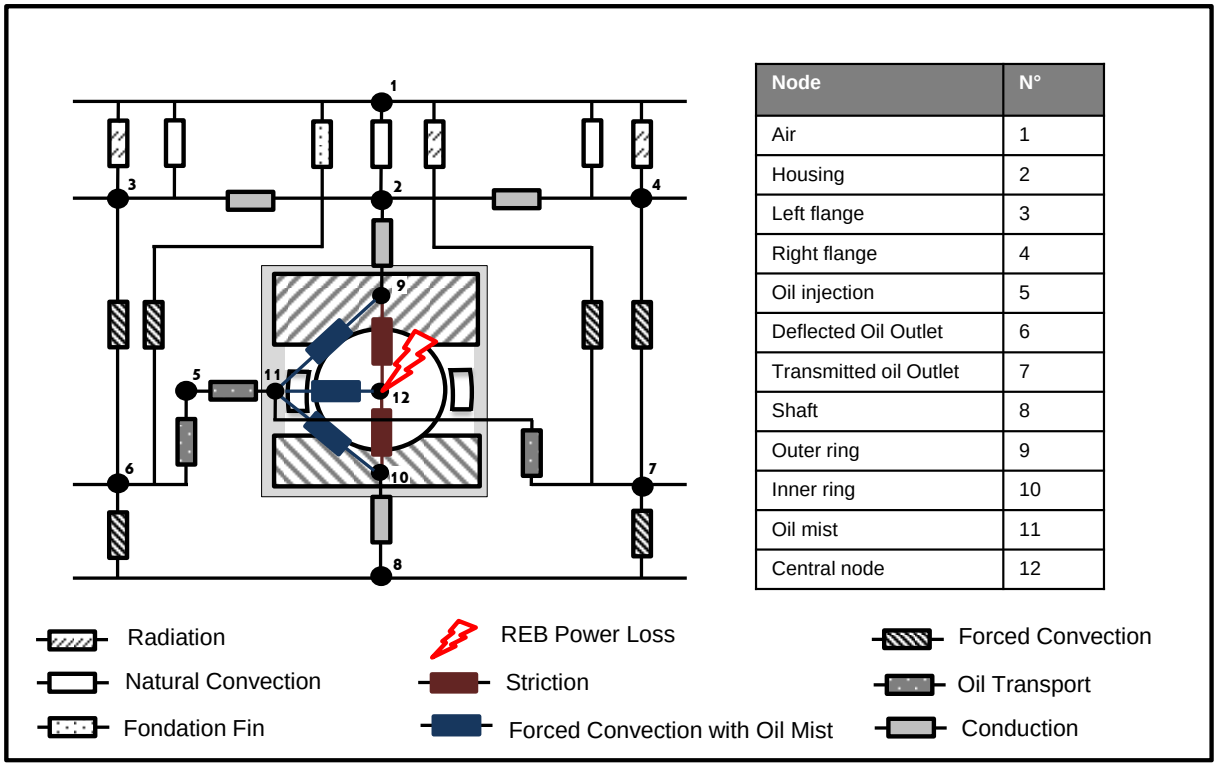

Node	N°
Air	1
Housing	2
Left flange	3
Right flange	4
Oil injection	5
Deflected Oil Outlet	6
Transmitted oil Outlet	7
Shaft	8
Outer ring	9
Inner ring	10
Oil mist	11
Central node	12

Figure 3.4 : Nodal thermal network of the test rig and the type B REB.

The housing has been divided into three nodes (#2, #3 and #4) which represent the three parts (#A, #B and #C) shown in figure 3.1. The nodes numbered 9 and 10 are respectively the outer and inner rings. The node 12, which is called the central node, is a virtual node obtained from the merging of both inner and outer contacts, the balls and the cage. Thanks to the prior calibration campaign, the support REB resistive torque was

subtracted to the measured one to obtain the REB power loss value to inject in the central node. The node 11 is the oil-air mixture within the rolling element bearing chamber and the nodes 6 and 7 represent respectively the deflected and transmitted oil outlet (see Figure 3.1).

In the thermal network, thermal resistances account for the different heat transfer phenomena between two nodes of the network, involving both series and parallel thermal resistances. In the following relationships, the thermal resistances will be detailed, and their locations provided, although equivalent resistance between two nodes are often composed of more than one resistance.

To evaluate thermal resistance of conduction, Fourier's law is applied. To do so, the heat exchange is considered as unidirectional, S is the cross-surface and L the considered distance. $k_{material}$ is the considered material thermal conductivity, in our case either hardened steel or aluminium alloy.

$$\{R_{2-3}; R_{2-4}\} \qquad \boldsymbol{R_{conduction} = \frac{L}{S \cdot k_{material}}} \tag{3.4}$$

An alternative formula is also available to quantify conduction heat transfer in the radial direction, for a solid considered as a cylinder for instance:

$$\{R_{2-9}; R_{8-10}\} \qquad \boldsymbol{R_{conduction} = \frac{ln(R_{ext} - R_{int})}{2\pi \cdot L \cdot k_{material}}} \tag{3.5}$$

where R_{ext} and R_{int} are the outer and inner radii, and L the length of the considered cylinder.

To evaluate thermal resistance of radiation, the Stephan-Boltzmann's law is applied ($\{R_{1-2}; R_{1-3}; R_{1-4}\}$). $\varepsilon_{material}$ is the material emissivity and σ the Stephen-Boltzmann's constant. The radiation is directed towards the ambient air as the heat departs from the system. The form factor is therefore considered equal to one.

$$\{R_{1-2}; R_{1-3}; R_{1-4}\} \qquad \boldsymbol{R_{radiation} = \frac{1}{\sigma \cdot S \cdot \varepsilon_{material} \cdot (T_j^2 + T_k^2) \cdot (T_j + T_k)}} \tag{3.6}$$

For contact between two moving components, the heat flux is confined within the contact area. Muzychka solved this problem for elliptical surface and it was extrapolated to the REB contacts as reported in equation (3.7) [91].

$$\{R_{9-12}; R_{10-12}\} \qquad \boldsymbol{R_{striction} = \left(\sum_{j}^{z} \left(\frac{0.918}{2 \cdot b_j \cdot \chi \cdot \sqrt{2 \cdot a_j \cdot V_R}} \right)^{-1} \right)^{-1}} \tag{3.7}$$

a_j and b_j are respectively the semi-major and semi-minor axis of contact of the j^{th} ball contact, χ is the thermal diffusivity and V_R the linear speed of rolling between the two bodies. For each of the m balls, inverse resistances are summed to obtain the overall resistance between the rings and the central node.

To take into account the heat conveyed by fluid motion, transport resistances are used considering the adequate volumetric oil flow rate. To do so, the penetration ratio α previously measured is used in (3.8) and (3.9). The total oil flow rate used in transport resistances must equal the total injection oil flow rate. The distribution of the total oil capacity to convey heat is equally divided between injection-mist resistance and between mist-outlet resistance. $C_{p_{oil}}$ and ρ_{oil} are respectively the specific heat and density of the oil.

$$\{R_{5-6};\} \qquad \boldsymbol{R_{transport} = \frac{1}{\rho_{oil} \cdot (1-\alpha) \cdot \dot{D}_{inj} \cdot C_{p_{oil}}}} \qquad (3.8)$$

$$\{R_{5-11}; R_{7-11}\} \qquad \boldsymbol{R_{transport} = \frac{1}{\rho_{oil} \cdot {}^{1}/_{2}\, \alpha \cdot \dot{D}_{inj} \cdot C_{p_{oil}}}} \qquad (3.9)$$

For convection heat transfers, the surfaces are considered as simple geometrical shapes. A thermal resistance is then calculated based on a Nusselt number N_u as seen in equation (3.10).

$$\boldsymbol{R_{convection} = \frac{L}{A \cdot k \cdot N_u}} \qquad (3.10)$$

Where L is characteristic length, A the surface area and k the fluid thermal conductivity. Depending on the surface shape and the flow topology, formulas from the literature are used and are reported in Table 3.16. In this table, Gr, Pr and R_e are respectively the Grashof, Prandtl and Reynolds number of the considered flow. A more detailed explanation on the determination of thermal resistance are found in the literature [83].

Convection types	Notation	Surface shapes	Flow topology	N_u Expression		References
Natural Convection	$\{R_{1-2}; R_{1-3}; R_{1-4}\}$	*Vertical Plate*	*Static Air*	$0.28 \cdot (Gr_{air} \cdot Pr_{air})^{0.3}$	*(3.11)*	[92]
	$\{R_{1-2}\}$	*Horizontal Fin*	*Static Air*	$0.2 \cdot (Gr_{air} \cdot Pr_{air})^{0.32}$	*(3.12)*	[83]
Forced Convection	$\{R_{2-6}; R_{3-6}; R_{2-7}; R_{4-7}\}$	*Plate*	*Tangent to Oil*	$0.664 \cdot Pr_{oil}^{1/3} \cdot Re_{oil}^{1/2}$	*(3.13)*	[92]
	$\{R_{6-8}; R_{7-8}\}$	*Cylinder*	*Rotating Air*	$133 \cdot Pr_{air}^{1/3} \cdot Re_{air}^{2/3}$	*(3.14)*	[93]
Forced Convection with oil mist	$\{R_{11-12}\}$	*Sphere*	*Across Oil Mist*	$Pr_{mist}^{0.3} \cdot (1.2 + 0.53 \cdot Re_{mist}^{0.54}) \cdot \left(\frac{\nu_{mist}}{\nu_{wall}}\right)^{1/4}$	*(3.15)*	[92]
	$\{R_{9-11}; R_{10-11}\}$	*Plate*	*Tangent to Oil Mist*	$0.664 \cdot Pr_{mist}^{1/3} \cdot Re_{mist}^{1/2}$	*(3.16)*	[92]

Table 3.16 : Nusselt expression depending on surface shape and flow topology

The ability of the tested REB housing to exchange heat with the surrounding environment depends on natural convection and radiation. The external surfaces of the housing and flanges were assumed as vertical plates of equivalent area in equation (3.11).

An additional resistance was added assuming the foundation acts as a horizontal fin as highlighted by equation (3.12). A fin efficiency can be determined to weight the heat exchange surface area associated with the heat-transfer coefficient. The calculus is detailed in appendix F.

Equation (3.13) is used for the housing and flanges interactions with the oil streaming down to the oil outlets due to gravity. The surfaces were thus considered as plates of equivalent area. The shaft surfaces were considered as a cylinder whose sides act as fins: no heat transfer is assumed at both tips and another fin efficiency is added to weight the exchange surfaces. The equation (3.14) is used considering air rotating at the shaft speed.

For the forced convection with the oil mist in equation (3.15) , the balls are considered as spheres going through the oil mist at the orbital speed. The ball-mist resistance depends on a ratio of viscosity taken at the medium temperature (ν_{mist}) and at the solid temperature (ν_{wall}). In equation (3.16), the REB ring surfaces are assumed as plates on which the oil mist flows at the ring speed. The balls own rotation influence on heat transfer is neglected. The cage interactions with other elements are also neglected. The oil mist is considered as a homogenous equivalent fluid which proprieties depend on mixture laws.

3.4.2 Mixture Laws

At sufficient speed, the oil within the bearing chamber is pulverized into droplets by the passage of rolling elements. This suspension forms a heterogenic mixture with air called oil-mist. This oil mist is denser than pure air and has different characteristics depending on the amount of oil versus air. The ratio of the volume of oil to the REB chamber volume is called the volume fraction and is widely used to depict oil mist properties. The oil mist interacts with the element in rotation, by both applying a resistance to motion and by exchanging heat. A global agreement is found to emphasize the influence of lubrication design and oil flow rate on thermal management *via* the oil mist properties [16,70,94].

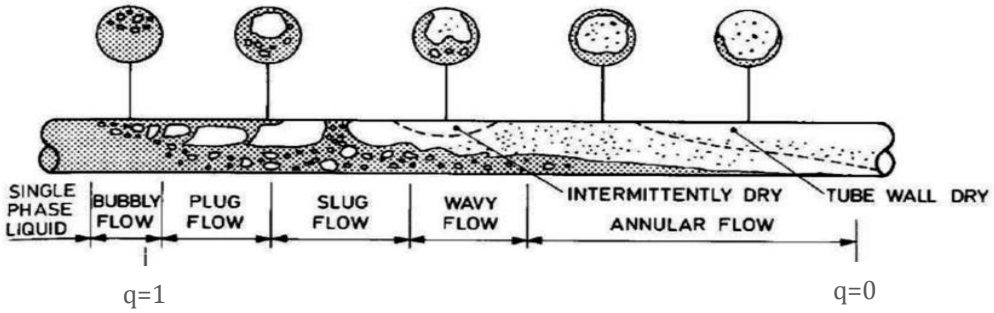

Figure 3.5: Flow regime along a horyzontal tube depending on mixture quality

The flow evolution towards quality for a horizontal pipe is illustrated in Figure 3.5. The assumption of an oil mist is valid as long as the liquid phase does not form ripples on the surfaces [95]. The difference between a horizontal pipe and a REB is that both phases are equally caught up by the REB rotations. In a REB, this hypothesis is acceptable for sufficient rotational shaft speed. If the oil-mist is assumed homogenous, its characteristics will depend on mixture laws. The oil volume fraction as defined previously is presented in *(3.17)*.

$$X = \frac{V_{oil}}{V_{oil} + V_{air}} \tag{3.17}$$

The oil volume V_{oil} and the air volume V_{air} are the theoretical spaces occupied by both fluids. In steady-state conditions these terms can be replaced by volumetric flow rates. The emphasis should be put on the fact that they are not flow rates entering the REB but orbiting the REB in the direction of motion. The oil mass fraction, or commonly named quality, is presented in *(3.18)* depending this time on the oil and air masses, namely m_{oil} and m_{air}. The same remark can be made in steady-state conditions. One can imagine the difficulty of measuring both fractions on a rotating REB.

$$q = \frac{m_{oil}}{m_{oil} + m_{air}} \tag{3.18}$$

The oil mist thermal properties are proportional on either the oil volume fraction or the mixture quality. The density of the mist for instance depends on the oil volume fraction and the density of pure oil and pure air, as seen in equation (3.19).

$$\rho_{mist} = X \cdot \rho_{oil} + (1 - X) \cdot \rho_{air} \tag{3.19}$$

The specific heat capacity of the mist on the other hand depends on the quality in addition to the pure air and pure oil specific heat capacities (equation *(3.20)*).

$$C_{p_{mist}} = q \cdot C_{p_{oil}} + (1 - q) \cdot C_{p_{air}} \tag{3.20}$$

Assuming that the droplets of oil and the air have the same velocity, the equivalent thermal conductivity can be developed in equation *(3.21)*, although this assumption is criticized in [95]. The equivalent thermal conductivity thus depends on the oil volume fraction and the thermal conductivity of pure oil and pure air.

$$k_{mist} = X \cdot k_{oil} + (1 - X) \cdot k_{air} \tag{3.21}$$

Concerning the mist viscosity, the properties are not proportional to neither the oil volume fraction or quality but on their inverse [96]. Kinematic and dynamic viscosity are presented in equations *(3.19)* and *(3.23)* depending on the inverse viscosity of pure air and pure oil.

$$\frac{1}{\mu_{mist}} = q \cdot \frac{1}{\mu_{oil}} + (1-q) \cdot \frac{1}{\mu_{air}} \qquad (3.22)$$

$$\frac{1}{\upsilon_{mist}} = X \cdot \frac{1}{\upsilon_{oil}} + (1-X) \cdot \frac{1}{\upsilon_{air}} \qquad (3.23)$$

As a conclusion, oil-mist characteristics heavily depend on the proportion of oil in the REB chamber. A few percent of oil are sufficient to drastically increase its density, whereas its kinematic viscosity is little affected at first.

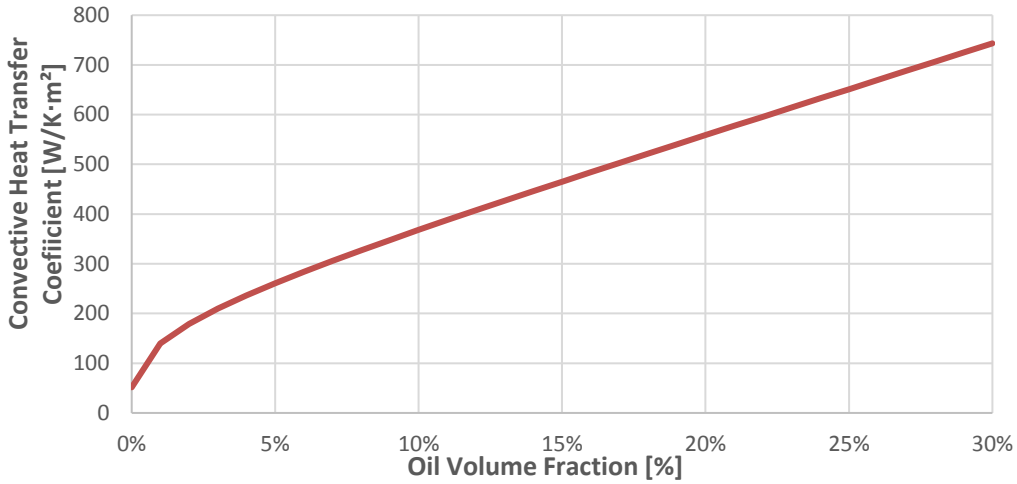

Figure 3.6 : Influence of Volume fraction* X *on the convective heat transfer coefficient

On Figure 3.6, the influence of Oil volume fraction *X* on the convection heat transfer is shown on a theoretical application. The surface is assumed to be a plate, where the characteristic length is taken to be 0.1 meter for a mixture of oil and air at 100°C flowing at 20m/s. It can be seen that the first percent of oil added to the air have a significant influence on the convection heat transfer coefficient. Afterwards, the convection heat transfer will gradually increase to tend to the theoretical value for pure oil. The ability of the REB to exchange heat with the oil flow is therefore strongly dependent on the oil volume fraction.

The oil volume fraction evolves with the REB operating conditions. In 1984, Parker used an inverse method from resistive torque measurements to corroborate the oil volume fraction for an angular ball bearing with either split inner ring lubrication or jet lubrication [70]. The more oil is poured into the bearing, the more power loss increases. By considering a single sphere isolated in space in a stream flow, he managed to curve fit a formula for the oil volume fraction to corroborate the increase in power losses for different speeds and REB diameters. This formula is presented in equation (3.24).

$$X = 62.8 \cdot \frac{\dot{D}_{inj}^{0.37}}{\omega_i \cdot d_m^{1.7}} \qquad (3.24)$$

By considering aligned spheres in a stream flow, Pouly used another drag coefficient and adapted Parker's formula accordingly [86]. This formula is presented in equation (3.25).

$$X = 314 \cdot \frac{\dot{D}_{inj}^{\ 0.37}}{\omega_i \cdot d_m^{1.7}} \qquad (3.25)$$

The $\dot{D}_{inj}$ term represents the volumetric oil flow rate injected to the bearing. In the case of split inner race lubrication, it is equal to the oil flow rate passing through the REB. ω_i and d_m respectively are the shaft speed and the REB bore diameter.

Some consensus in the literature assumes an oil fraction of a few percent at high speed [57,70,78,97] whereas Pouly's formula enlarge its value [71,86]. Pouly showed that if the oil volume fraction cross drag coefficient product can be adapted to fit the power losses measurements, his higher oil volume fraction is required to properly model the measured temperature distribution within REBs. In order to apply Pouly's formula to the test rig, the transmitted oil flow rate should be taken into account. To do so, the penetration coefficient is added to the formula in equation (*3.26*).

$$\boldsymbol{X = 314 \cdot \frac{(\alpha \cdot \dot{D}_{inj})^{0.37}}{\omega_i \cdot d_m^{1.7}}} \qquad (3.26)$$

3.4.3 External Heat exchange

In order to validate the modelled heat transfer between the housing and the surrounding environment, temperature measurements are conducted during cooling experiments of the test rig. Figure 3.7 underlines that a good agreement is found. It can also be noticed that the front area and the back area of the housing measured temperatures are nearly identical. This validates the hypothesis of taking the housing as a unique isothermal node in the network.

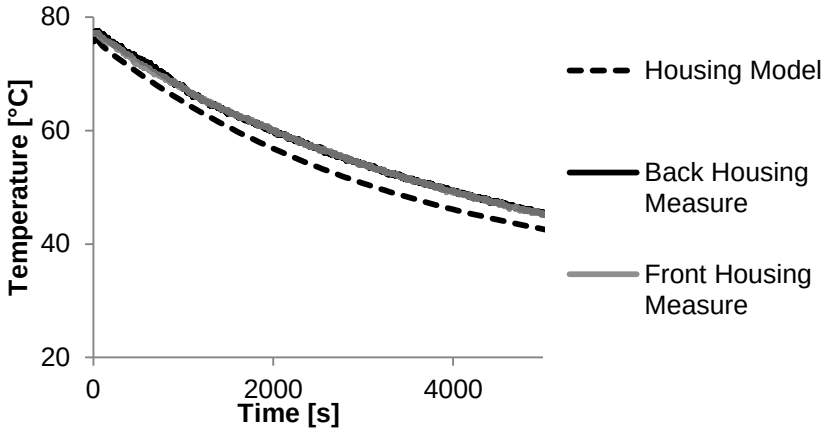

Figure 3.7 : Thermal response of the REB housing during a cooling

3.4.4 Heat exchange with oil injection and outlets

Once the external thermal behaviour of the housing is validated, the heat exchanges between the oil injection, the REB, the housing and the outlets are modelled.

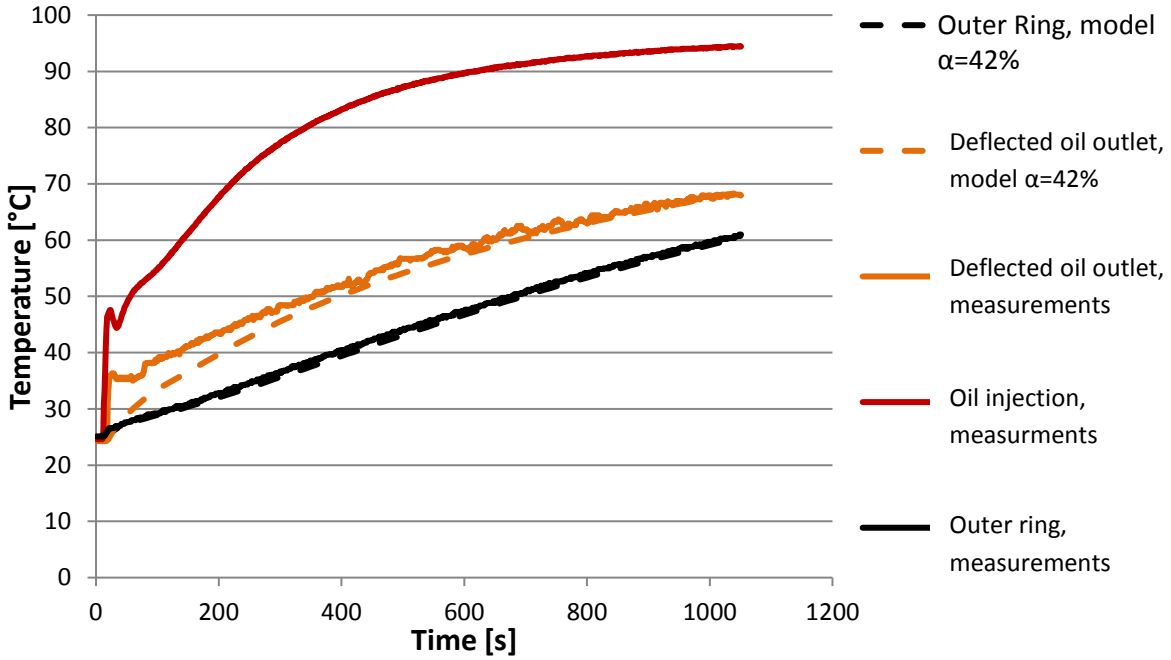

Figure 3.8: Comparison of modelled and measured temperatures

A first set of experiment was made to emphasize the influence of the penetration ratio. A heating phase at low rotational speed (4700 rpm), at low radial loadings (1 kN), with high temperature oil tank set point (100°C) was done. The oil injection was set at 20L/h on a cold test rig. Injection temperature rapidly increases up to a value close to 100°C. The heat produced by the REB was directly measured through the resistive torque. The relatively low shaft speed implies a relatively low convection heat transfer within the REB chamber. Moreover, at this speed, the REB power losses and the heat brought by the injection are of the same order (80 Watts).

Thus, this experiment enables a closer understanding of the oil injection interaction with the REB. It can be seen on Figure 3.8 that a good correlation between deflected outlet temperature measurement and modelled temperature are found for the measured penetration ratio (42%). It can be underlined that the penetration ratio has to be applied to the thermal network in order to properly model the amount of heat being exchanged to the transmitted oil and to the deflected one. The outer ring temperature evolution is also perfectly modelled.

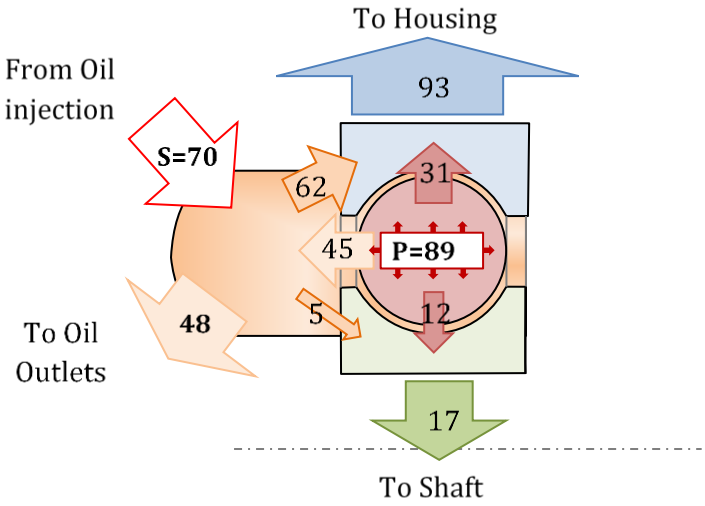

Figure 3.9: Heat transfer within the REB in Watts

A detailed description of the heat transfer within the REB in Watts is shown on Figure 3.9. Moreover, most of the heat is being extracted by the outer ring to the housing, where it will then spread to the ambient air. A common tool to analyse the partitioning of heat within the REB is the partition coefficient, defined as the ratio of heat going through a component divided by the total amount of heat generated. In order to calculate these coefficients, one must first realize the heat balancing of each concerned node.

In a steady state condition, the total amount of heat generated and brought to the system is equal to the amount of heat leaving the system (equation (3.27)).

$$P_{Tot} = S + P = Q_{mist-outlets} + Q_{OR-Housing} + Q_{IR-Shaft} \tag{3.27}$$

The S term represents the amount of heat brought by the oil injection. The P represents the amount of heat the REB produces. $Q_{mist-outlets}$ is the amount of heat exchanged between the oil mist and the oil outlets. $Q_{OR-Housing}$ and $Q_{IR-Shaft}$ are the amount of heat exchanged from respectively the inner ring to the shaft and the outer ring to the housing.

Dividing by the total amount of heat, the partition coefficient can appear in equation *(3.28)*.

$$100\% = \frac{Q_{mist-outlets}}{P_{Tot}} + \frac{Q_{OR-Housing}}{P_{Tot}} + \frac{Q_{IR-Shaft}}{P_{Tot}} \tag{3.28}$$

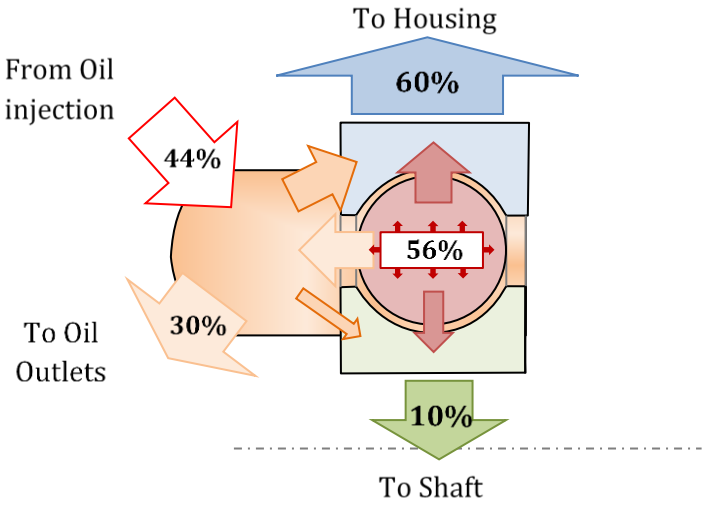

Figure 3.10: **Partition coefficient in percentage**

Figure 3.10 shows the obtained heat partition coefficient for the tested REB in this set of experiments. The outer ring drains 60% of the total heat whereas 30% is driven towards the oil outlets. Only 10% of the heat is conducted through the inner ring. These result shows that the heat partitioning is highly dependent on the boundary conditions applied to the REB, and not solely dependent on operating conditions.

3.4.5 Heat exchange within the REB

A second set of experiment was made at higher speeds [8070 and 9700 rpm] to emphasize the influence of the oil volume fraction on convective heat-transfer coefficients.

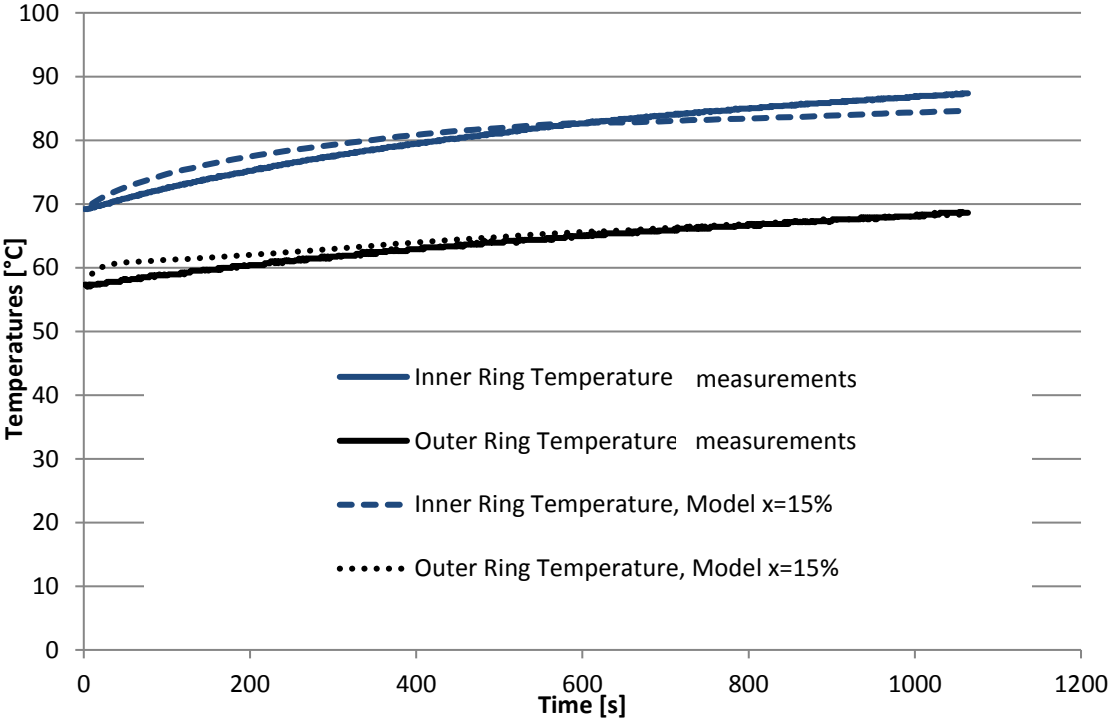

Figure 3.11 : Comparison between temperature measurements and model for 15% oil volume fraction, 37% penetration ratio at 9700 rpm

The radial loading was kept relatively low (1 kN), with medium temperature of oil injection (67°C). The oil injection was set at 20L/h. The heat produced by the REB was also measured and integrated into the model central node. The oil injection now removes heat from the system and the heat produced by the REB is about 200W.

As seen in Figure 3.11, the model succeeds in predicting both the outer ring and inner ring temperatures. A higher oil volume fraction would lead to a lower inner ring temperature, whereas a lower oil volume fraction will lead to a higher one [20]. The oil volume fraction formula for jet lubricated rolling element bearing has therefore been validated.

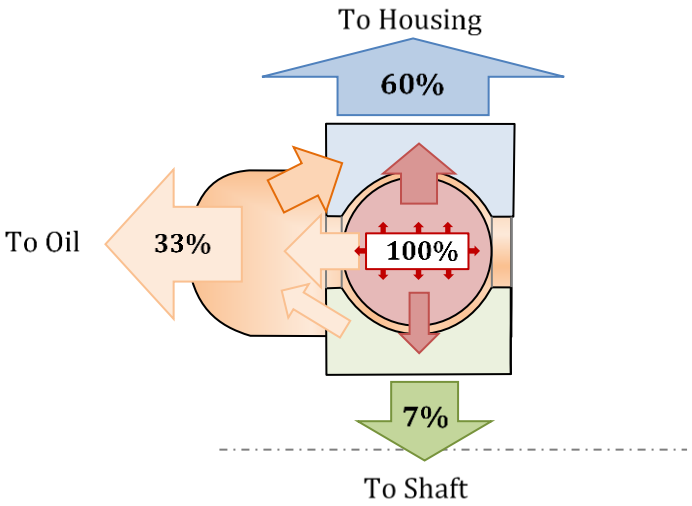

Figure 3.12: **Partition coefficient at 9700 rpm**

For this set of experiment, the oil injection has now a cooling role over the REB. The partition coefficients are shown in ***Figure*** 3.12. The outer ring partition coefficient remains as high as 60%. On the other hand, the inner ring partition coefficient is lower than before. The amount of heat extracted through the oil mist reaches a value of 33%.

As a conclusion, the thermal behaviour of the test rig has been modelled. The penetration ratio is required in order to quantify how much oil entered the bearing and thus, how much heat the oil conveys from the bearing. Moreover, the penetration ratio is an important parameter as it characterizes the oil mist ability to extract heat from the REB. The presented results show that the existing formula to quantify oil volume fraction for split-inner ring lubrication can be extended to oil injection by taking into account this penetration ratio.

With a thermal model of the test rig empirically validated, the analysis now focuses on the influence of lubrication and geometry on REB power losses.

3.5 REB thermal model results and discussion

As was established in the previous chapter, two mean questions remain concerning REB power loss. The first concerns the influence of oil flow rate on resistive torque: how does lubrication influences power losses? The second concerns the influence of geometry, to what extent geometry influences REB power losses and how to model it?

The previously validated thermal model and the adjusted Harris Palmgren model for resistive torque are jointly used. In Figure 3.13, the numerical integration scheme is shown. In the previous part of this chapter, there was no need of a thermal coupling between the temperature calculation and the power losses model as the resistive torque was directly measured.

The type B REB is first simulated with different lubrication using two oil flow rates [15 ; 35 L/h] and two oil injection temperatures [60;90°C]. Then, the type A REB is simulated correspondingly to enable a comparison of both REBs.

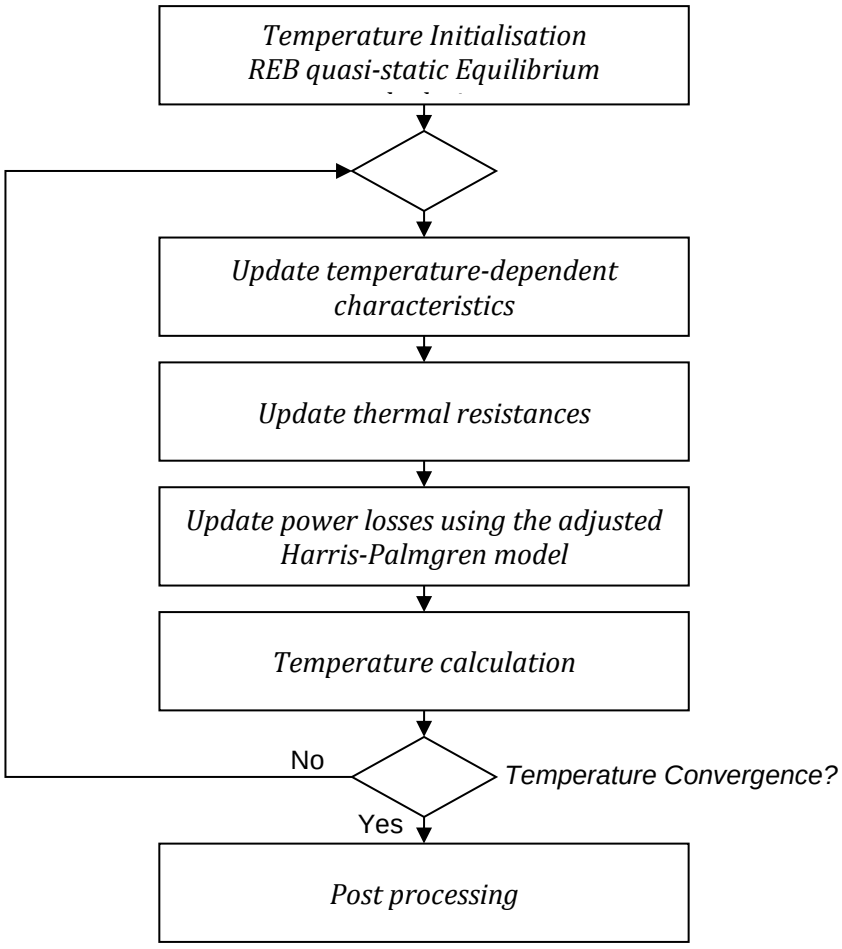

Figure 3.13: **Numerical integration scheme**

3.5.1 The influence of lubrication

In this set of calculations, the adjusted Harris-Palmgren model for resistive torque is used. To recall, the empirical f_0 parameter for type B REB depends on lubrication. For a 70°C oil injection, f_0 parameter values are 3.9 and 4.3 for an oil flow rate of 15L/h and 35 L/h, respectively. At 90°C oil injection, however, both oil flow rates produce a similar resistive torque, requiring a single f_0 parameter, *i.e.* 3.9. Here, the adjusted model will be used with a single f_0 parameter of 3.9 for type B REB. The ambient air is fixed at 20 °C, the radial load at 1kN and the calculations are performed until steady state is reached.

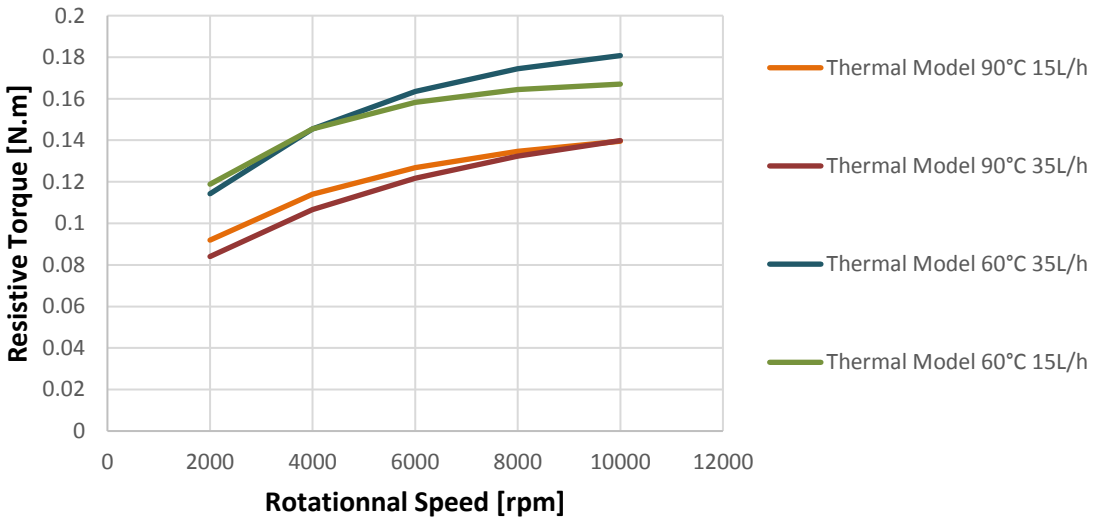

Figure 3.14 : Resistive torque calculations for two oil flow rates and two oil injection temperature

In Figure 3.14, presents the calculated resistive torques for two oil flow rates and two oil injection temperatures. At speeds lower than 6000 rpm, the resistive torque for the [60°C;35 L/h] curve are similar to the [60°C - 15L/h] one. As the speed increases, the [60°C - 35 L/h] calculation gradually produces more resistive torque than the [60°C - 15 L/h] one. Conversely, at speeds lower than 6000 rpm, the [90°C - 35 L/h] resistive torque measures are lower than the [90°C - 15 L/h]. As the speed increases, [90°C - 35 L/h] modelled resistive torque gradually reaches the [90°C - 15 L/h] one. In the previous chapter, Figure 2.15 shows the influence of oil low rates at 60°C and 90 °C oil injection temperatures. A comparison between the calculated and measured results is shown on Figure 3.15. Simulations cannot be compared directly with measurements as the experiments do not reach in steady-state conditions. To do so, the resistive torque values for the 35 L/h are divided by the 15 L/h ones. Thus, the obtained resistive torque ratio represents the influence of oil flow rate on resistive torque.

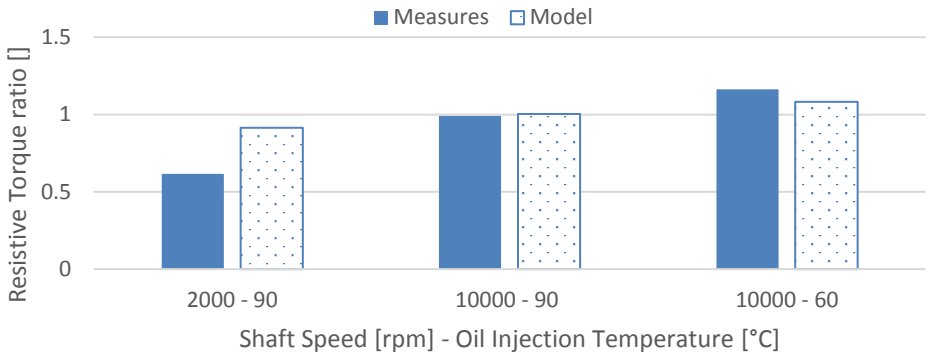

Figure 3.15 : Comparisons of resistive torque ratio between 35L/h and 15 L/h

Figure 3.15 presents resistive torque ratios for different shaft sped and oil injection. It appears that the amplitude of the measured ratio evolution is greater than the simulated one, but the general trend is similar.

At low speed (2000 rpm) and high oil injection temperature (90°C), both simulated and measured ratios are below one, the 35 L/h experiment producing less resistive torque than the 15 L/h one. Indeed, at low speed, power losses are quite low. Hence, with a hot oil injection, an increase in oil flow rate will increase the temperature, reducing the viscosity and the heat production.

At high speed (10 000rpm) and high oil injection temperature (90°C), the resistive torque ratios reach one for both model and measures. The additional heat brought by the high oil flow rate injection is counterbalanced by the enhancement of heat exchange, cooling down the REB. This equilibrium leads to ring temperatures stable towards oil flow rates. Therefore, oil flow rate has a modest influence on resistive torque which result in a ratio near one in these conditions.

At high speed (10 000rpm) and low oil injection temperature (90°C), the resistive torque ratios are above one. The improvement of convective heat exchange leads to a cooler temperature increasing heat production while reaching a lower temperature balance.

To conclude, the influence of lubrication on resistive torque observed in chapter 2 is also observed for steady-state simulations. The influence of oil flow rates is linked to oil injection temperature because of the thermal equilibrium that takes place within the REB. A thermal coupling is required in order to predict it. The comparisons between steady-state calculations and experiments can be explained using a single f_0 parameter for the type B REB. It appears that the oil flow rate has not a direct influence on the friction mechanisms involved within the boundaries of this study.

3.5.2 Geometry influence

Ultimately, the thermal model is also used to compare the two previously tested REBs. The smaller Type A REB produces 25 % less heat than the larger Type B. However,

the original Harris-Palmgren model has an exponent three over the bore diameter. As type B REB has a bore diameter nearly 40 % larger than type A one, the use of a single Harris-Palmgren model leads to a resistive torque nearly three times larger. This consideration leads to the use of different f_O parameters. The empirically obtained coefficients were 3.9 for the Type B REB and 7.7 for the Type A REB.

One hypothesis could be that one REB cools off more easily than the other one and thus generates more power losses than expected. In order to investigate if this result can be explained by different thermal behaviours, the following approach is used:

i. The Harris-Palmgren model was applied to Type B REB using the adjusted f_0 coefficient.
ii. For the type A REB, both its own adjusted f_0 coefficient and the type B adjusted coefficient are tested.

Because the previously mentioned experiments are not stabilized in temperature, the measured and simulated REB temperatures are too different to be compared. In order to do so, type B REB resistive torques are divided by type A REB ones. A resistive torque ratio is obtained for: the measurements in equation (3.29); the model using a single f_0 parameter in equation (3.30); the model using two values for the f_0 parameter in equation (3.31).

$$\Gamma_{measured} = \frac{M_{type\ B}}{M_{type\ A}} \tag{3.29}$$

$$\Gamma_{single} = \frac{M_{0-type\ B}(f_0 = 3.9)}{M_{0-type\ A}(f_0 = 3.9)} \tag{3.30}$$

$$\Gamma_{different} = \frac{M_{0-type\ B}(f_0 = 3.9)}{M_{0-type\ A}(f_0 = 7.7)} \tag{3.31}$$

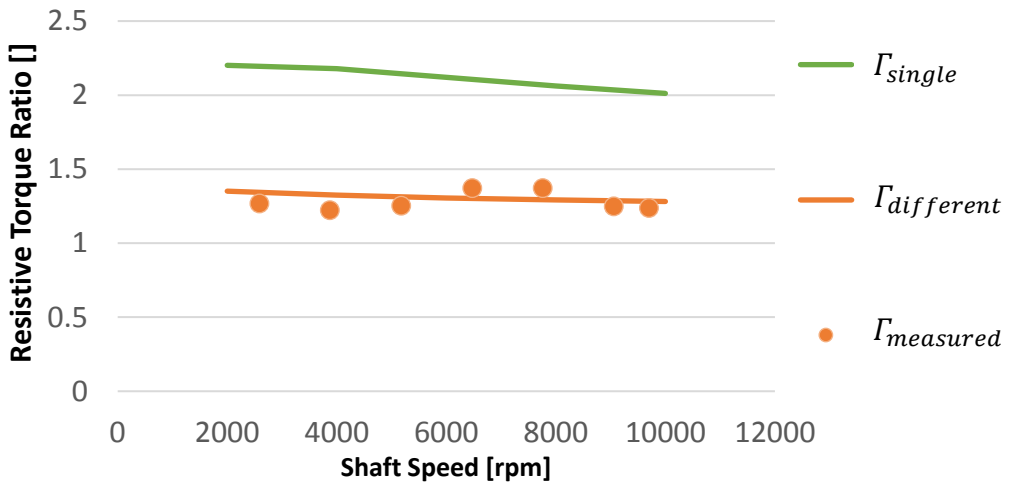

Figure 3.16 : Comparison of the influence of f_0 on resistive torque and measurements between the REBs.

The data used is for a 15L/h oil flow rate at 60°C oil injection temperature. Figure 3.16 shows that the measured ratio oscillates around a constant value of 1.25. Indeed, the type B REB produces 25 % more resistive torque then type A. The model using different values for the f_0 parameters perfectly seized this ratio. The obtained model ratio using a single f_0 parameter is on the other hand around two.

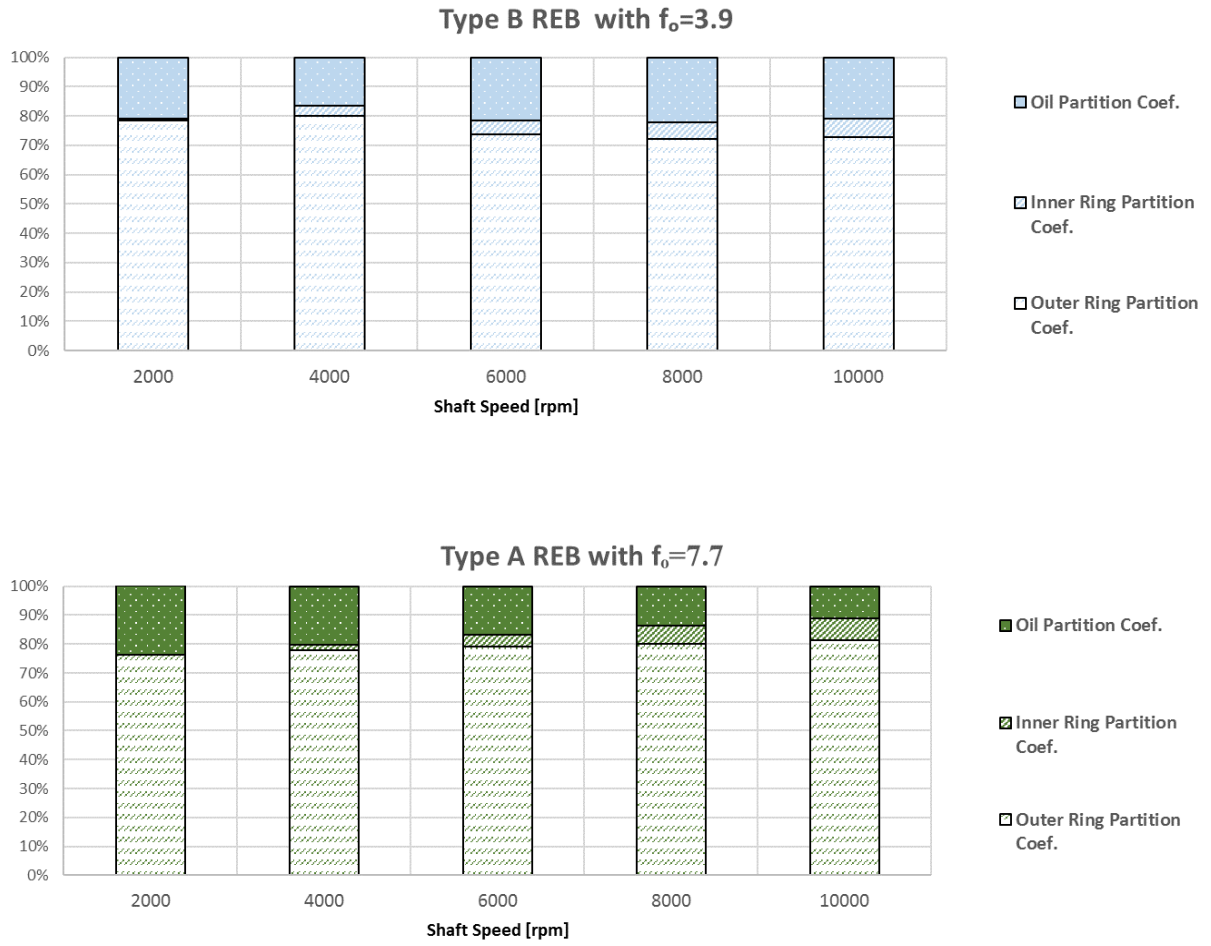

Figure 3.17 : Comparison of partition coefficient for type A and type B bearing

To analyse the REB thermal behaviours, the partition coefficients previously introduced are presented in Figure 3.17. Although the oil partition coefficients are higher for the type B REB than for the type A, both REBs have a nearly constant outer ring partition coefficient *versus* speed. The inner ring partition coefficient is relatively low (<10%) and slightly increases with speed. The oil partition decreases accordingly. The housing evacuates between 70 to 80% of the heat overall.

As a conclusion, the thermal behaviours of both REBs are similar and a single f_0 coefficient fails to predict the resistive torque differences. In the Harris-Palmgren model, only the bore diameter is considered to take into account geometry. The bore diameter at the power three forbids the use of a single universal model. Additionally, according to this model, two REBs with similar bore diameter but different rolling elements (size and

number) would generate similar resistive torques. These discrepancies lead to new developments to assess the influence of REB geometry on resistive torque.

In order to investigate the influence of geometry on REB heat production, the elasto-hydrodynamical rolling phenomenon presented in the first chapter is analytically investigated. As reported in equation *(1.9)*, the rolling traction force can be expressed depending on the rolling element loading, speed, viscosity and geometry. The idea is to extrapolate the rolling resistance of a single contact to the whole REB. The demonstration is detailed in Appendix E. The analysis focuses on deep groove ball bearing under radial load. Different hypotheses are used, such as:

- rolling without sliding at both rings
- zero diametral clearance
- standard hardened steel equivalent Young's modulus $E' = 231\ GPa$
- medium oil piezo viscosity $\alpha = 1.5 * 10^{-8}\ Pa^{-1}$
- standard ring osculations, $f_e = f_i = 0.52$
- medium oil density, $\rho_{oil} = 900\ kg/m^3$

The rolling traction force was extrapolated for each rolling element into a global resistive torque applied to the shaft. The following proportionality relationship was obtained:

$$M_{rr_{th}} \propto \cdot (\upsilon_{oil} \cdot \omega_i)^{0.66} \cdot \gamma^* \cdot d_m^{1.66} \cdot F_r^{0.47} \cdot Z^{0.53} \cdot D^{0.4} \tag{3.32}$$

The operating conditions of influence are the shaft speed ω_i, the oil viscosity υ_{oil} and the applied radial load F_r. The geometrical parameters of influence are the bore diameter d_m, the number of rolling elements Z, the diameter of rolling elements D, and a new parameter γ^* depending on the geometrical ratio γ in Equation (3.33).

$$\gamma^* = (1-\gamma)^{1.712} \cdot (1+\gamma)^{1.66} + (1+\gamma)^{1.712} \cdot (1-\gamma)^{1.66} \tag{3.33}$$

This new formulation depends on the applied radial load, while the M_0 in the orginal Harris-Palmgren model is load-independent. To compare both, the radial load was assumed to be 10% of the REB static load capacity. With a formula for the REB static capacity given by the standard [98], the relationship is adapted accordingly in equation (3.34).

$$M_{0_{th}} \propto \cdot (\upsilon_{oil} \cdot \omega_i)^{0.66} \cdot \gamma^* \cdot d_m^{1.66} \cdot Z \cdot D^{1.34} \tag{3.34}$$

The original Harris-Palmgren model was empirically obtained from a multitude of parametric experiments where the ratio between ball and bore diameters was set at 0.2 [9]. Using this geometrical assumption, (3.35) is obtained (details in Appendix G).

$$M_{0_{th}} \propto \cdot (\upsilon_{oil} \cdot \omega_i)^{0.66} \cdot d_m^{3.00} \tag{3.35}$$

Comparing to the load-independent contribution in the Harris-Palmgren model in 1.8.1, it appears that the formula are very similar. The original Harris-Palmgren load-

independent contribution is modified to include the proportionality over the previously mentioned geometrical parameters in equation (3.34). This new load-independent contribution mixes analytical considerations and empirical measurements with the f_0 parameter.

$$M_{0_{new}} = f_0 \cdot 4.5 \cdot 10^3 \cdot \upsilon_{oil}^{0.66} \cdot \omega_i^{0.51} \cdot \gamma^* \cdot d_m^{1.66} \cdot Z \cdot D^{1.34} \tag{3.36}$$

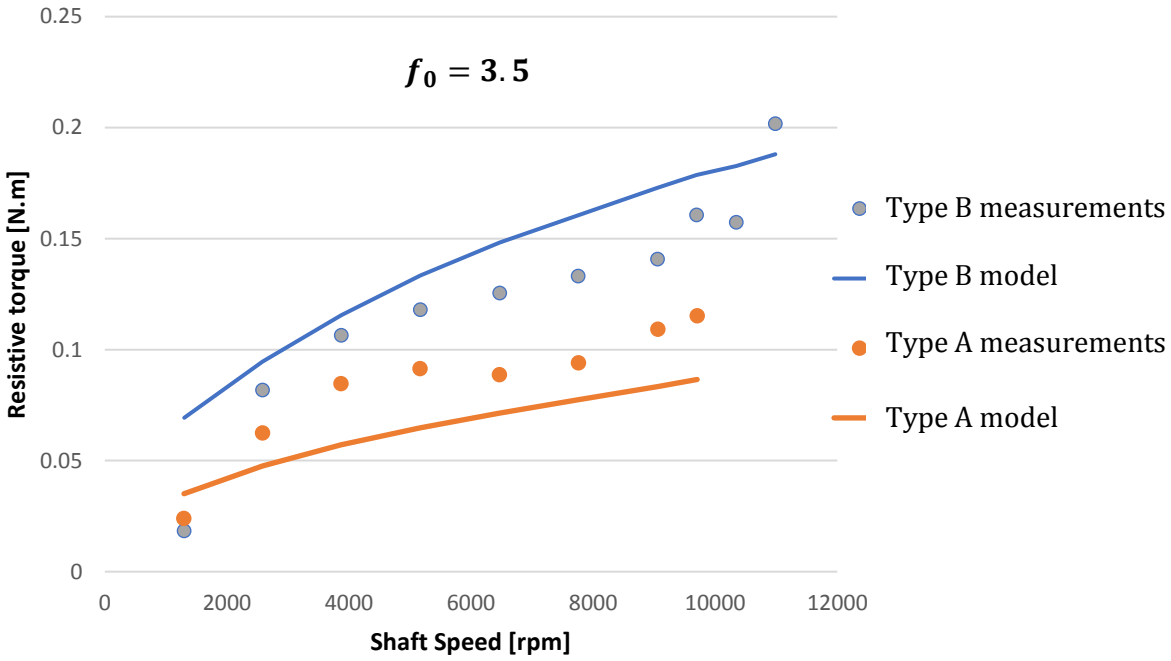

Figure 3.18 : Comparison of both REB resistive torque to the new model

This new load-independent model is compared to the resistive torque measured with both REBs on Figure 3.18. Even though this new model is not able to fit the curves, a notable improvement can be underlined as it uses a unique f_0 parameter for both REBs. The measured result gives a 25 % resistive torque increase from REB A to REB B. The original formula would have predicted a 170% resistive torque increase from REB A to REB B. This new formula gives a 73% increase.

The influence of geometry is similar than what was obtained with the SKF model in 2.5.1. To compare both approaches, some modifications must be made in order to compare the SKF rolling contribution and the new load-independent contribution.

The rolling contribution of the adjusted SKF model presented in equation *(2.13)* is expressed in equation (3.37). The same 10% C_0 threshold that was previously applied to the adjusted SKF model is used to compare low load conditions.

$$M_{rr} = 1.17 \cdot 10^{-7} \cdot R_1 \cdot \varphi_{rs} \cdot d_m^{1.96} \cdot F_{r_{threshold}}^{0.54} \cdot (\upsilon \cdot \omega_i)^{0.6} \tag{3.37}$$

In the original Harris-Palmgren model, only the bore diameter influenced resistive torque, whatever the geometrical ratio γ. The SKF model on the other hand is more

ambiguous towards the influence of geometry. The bore diameter is present to the power 1.96 for deep groove ball bearing, but depending on REB series, the R_1 coefficient differs. Moreover, the replenishment factor φ_{rs} also includes geometrical features such as ring diameters. In order to compare the evolution of SKF towards geometry, eighteen deep groove ball bearings were selected to represent a large panel of bore diameters and geometrical ratios.

N°	Designation	di	de	B	dm	C0	dri	dre	D	Z	R1	γ
		[mm]	*[mm]*	*[mm]*	*[mm]*	*[kN]*	*[mm]*	*[mm]*	*[mm]*	*[]*	*[]*	*[]*
1	61804	20	32	7	26	2.32	23.8	28.3	3.8168	13	4.7E-07	0.15
2	6204	20	47	14	33.5	6.55	28.8	38.5	7.9328	8	3.9E-07	0.24
3	6404	20	72	19	46	15	37.1	54.8	15.088	6	3.6E-07	0.33
4	61808	40	52	7	46	3.75	43.2	48.1	3.5512	21	4.7E-07	0.08
5	6208	40	80	18	60	19	52.6	67.4	12.336	9	3.9E-07	0.21
6	6408	40	110	27	75	36.5	62.8	87	20.64	7	3.6E-07	0.28
7	61812	60	78	10	69	11.4	65.6	72.4	5.5752	21	4.7E-07	0.08
8	6212	60	110	22	85	36	75.5	94.6	15.844	10	3.9E-07	0.19
9	6412	60	150	35	105	69.5	88.1	122	28.518	7	3.6E-07	0.27
10	61816	80	100	10	90	15	86.6	93.4	5.544	27	4.7E-07	0.06
11	6216	80	140	26	110	55	101	123	17.204	12	3.9E-07	0.16
12	6416	80	200	48	140	125	116	163	38.15	7	3.6E-07	0.27
13	61820	100	125	13	112.5	18.3	108	117	7.2	27	4.7E-07	0.06
14	6220	100	180	34	140	93	124	155	25.424	10	3.9E-07	0.18
15	6320	100	215	47	157.5	140	135	180	36.54	8	4.1E-07	0.23
16	61824	120	150	16	135	28	128	142	8.802	27	4.7E-07	0.07
17	16024	120	180	10	150	64	139	161	14.28	19	4.3E-07	0.10
18	6324	120	260	55	190	186	164	215	41.344	8	3.7E-07	0.22

Table 3.17 : REB list with geometrical characteristics

As it can be seen in ***Table*** 3.17, the R_1 parameter differs over this list. The geometrical ratio γ varies from 0.06 to 0.33. To only compare the influence of geometry on these models, some adaptations are made. The product of viscosity and speed, being the same for the three models, is left out. Only φ_{rs} still depends on operating condition which was arbitrarily fixed at 5000 rpm and 20 cSt kinematic viscosity. Equations (3.38), (3.39), and (3.40) presents the Harris-Palmgren, SKF and new load-independent models respectively.

$$\overline{M_{0_{HPM}}} = a_1 \cdot d_m^3 \tag{3.38}$$

$$\overline{M_{rr}} = a_3 \cdot R_1 \cdot \varphi_{rs} \cdot d_m^{1.96} \cdot \left(\frac{C_0}{10}\right)^{0.54} \tag{3.39}$$

$$\overline{M_{0_{new}}} = a_2 \cdot \gamma^* \cdot d_m^{1.66} \cdot Z \cdot D^{1.34} \tag{3.40}$$

To compare the influence of geometry on these models, coefficients a_* are added. These coefficients are obtained so that the average value of each model over the eighteen

bearings is one. Finally, the dimensionless SKF rolling contribution $\overline{M_{rr}}$ and for the dimensionless new load-independent contribution $\overline{M_{0_{new}}}$ were divided by the Harris-Palmgren dimensionless model $\overline{M_{0_{HPM}}}$ in order to provide a ratio (so that the smaller REBs can be compared to the larger ones).

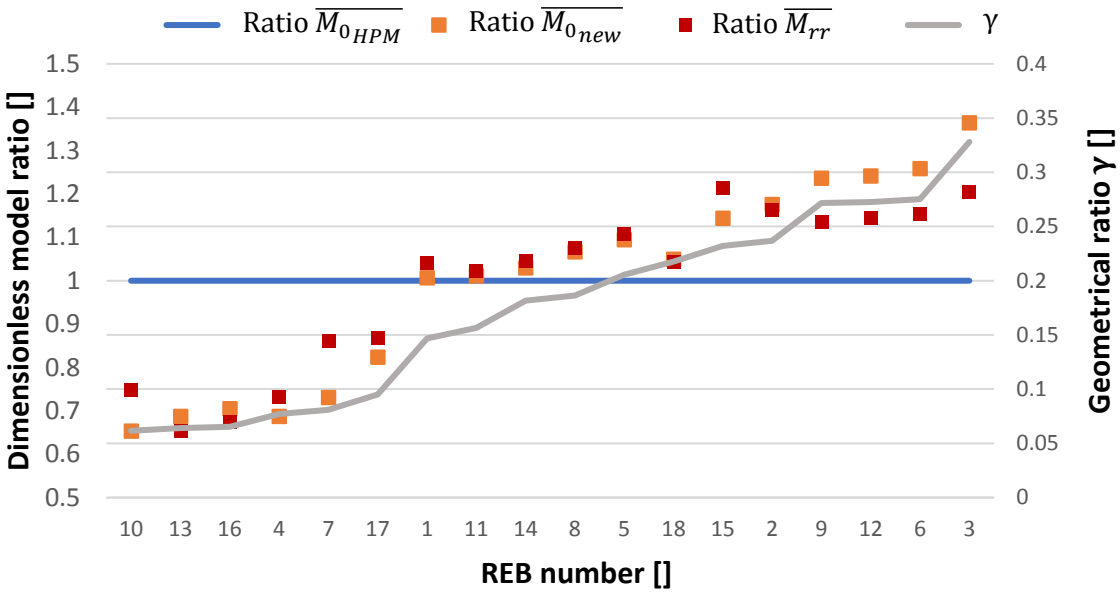

Figure 3.19 : Comparison of dimensionless models towards change in geometry.

On Figure 3.19 the REBs from ***Table*** 3.17 were sorted from low to high geometrical ratio γ. It can be seen that depending on series, the ratio of the models varies from 0.6 to 1.4. This means that the difference between the Harris-Palmgren model and the other ones can be as high as 40% depending on geometry.

The SKF model and the new model follow the same trend: as the geometrical ratio γ increases, the ratio compared to the Harris-Palmgren model increases. In fact, around $\gamma = 0.2$, the ratios are close to one, comforting the fact that the Harris-Palmgren model was based on REBs where $\gamma = 0.2$.

The ratios of the SKF and new load-independent contribution are similar, indicating that both takes the number and diameter of rolling element into account. Where the SKF model uses the R_1 parameter dependent on the REB series, the new formula only uses geometry input.

As a conclusion, the bore diameter to the power 3 in the Harris-Palmgren model is not realistic. The SKF model uses an exponent 1.96 over the bore diameter and catalogue-based coefficients to accord for the geometry. This method offers better result towards experiments on both tested bearings but is as of yet inaccurate. A modification of the Harris-Palmgren formulation from an analytical analysis offers similar results. Both methods seem consistent over the range of selected REBs. The advantage of the new load-independent contribution is the direct formulation of geometrical parameters in the

equation. Hence, the power loss model depends on the diameter and number of rolling elements in addition to the bore diameter. Moreover, this formulation can be applied to specific aeronautical REBs, which are not present in REB catalogue.

3.6 Conclusion

The thermal behaviour of the test rig was developed. In order to do so, two parameters of influence are introduced: the penetration ratio and the oil volume fraction. The penetration ratio quantifies the amount of oil entering the REB and the oil volume fraction defines the oil mist properties. New measurements of the penetration ratio are produced for different shaft speeds, oil injection temperatures and oil flow rates. It appears that the penetration ratio decreases with shaft speed, increases with oil flow rates and is constant towards oil injection temperature. To evaluate the oil volume fraction, a formula exists for split-inner ring lubrication technique, where all the oil manages to enter the REB chamber. A new formula, including this penetration ratio, is developed specifically for jet injection.

The present test rig thermal behaviour is modelled using dedicated experiments. The penetration ratio is required to model the heat exchange between oil injection, oil mist and oil outlets. When the REB power loss is significant, the oil volume fraction is required to model the convective heat exchange within the REB. This model allows the prediction of the inner ring temperature evolution.

Two topics were investigated using this model: the REB thermal behaviour according to lubrication and geometry. Firstly, it is empirically observed that the influence of oil flow rate on resistive torque is different depending on oil injection temperatures. The present thermal model shows that this behaviour is not dependent on power loss mechanisms but on thermal mechanisms. Secondly, global models fail to provide a single formula to predict power losses for both tested REBs. The second thermal investigation comparing both REB thermal behaviours do not justify this difference. A new formula issued from analytical calculation is presented for the load-independent contribution. It offers similar results compared to the SKF rolling formulation but can be applied to any REB as detailed single geometrical characteristics are taken into account.

Conclusion

Friction in Rolling Elements Bearings result in heat production, that should be rigorously evaluated during the development phase of any transmission system. In a helicopter gearbox, the cool-off system is optimised to inject the right amount of oil at the right place. In order to evaluate temperature distribution ahead of expensive empirical trials, a thermal model of the entire gearbox is compulsory. To that extent, evaluating the quantity of heat produced by REBs is not enough. Given the proximity some REBs to gear meshes, heat can be exchanged between components before exiting the system through the oil. Some knowledge about the heat pathway within the REB is therefore necessary in addition to its heat production calculation.

The first chapter of this study has focused on REB heat production models. Over the past decades, REB friction mechanisms have been widely examined. Three main physical phenomena are presented:

-The rolling contribution consists of the inlet meniscus being squeezed and reflowed. It has been taken into account in various ways in the literature. The product of viscosity and speed at the power 2/3 seems to reach agreement.

- The sliding contribution consists of the oil film shearing when slip occurs over the contact. It has been investigated using non-Newtonian piezo-viscous models. Yet, the sliding speeds required to calculate it are only found through dense iterative calculations.

-The drag and the churning contributions englobe all the interactions between the moving parts and the lubricant or an oil-air mixture. The drag contribution is presented as an analytical formula. Below 1 million $N \cdot d_m$, it appears negligible. The contact between cage and rolling elements are comparable to a lowly loaded plain bearing, which generates heat from viscous friction.

Alongside local phenomena, two global power loss models are also presented. Their simplicity of use already made them useful tool in the calculation of REB power loss:

- The Harris-Palmgren model separates a load-independent contribution and a load-dependent one. It was developed over a series of experiment on REBs. The load-independent contribution presents the same viscosity-speed product at the power 2/3.

- The SKF model separates three contributions: rolling, sliding and drag. Again, the viscosity-speed product is found at a power about 2/3 for the rolling contribution. The sliding contribution is built to assess changes in lubrication regime, from boundary regime to full film one. The drag contribution is in fact made of two terms representing the aerodynamical drag and the churning of the rolling elements in a lubricated bath.

The second chapter has presented new empirical data on REB power losses. The focus was put on Deep Groove Ball Bearing under radial loads. Two REBs are tested under

different operating conditions including shaft speeds, loads, lubrication techniques, oil injection temperatures and oil flow rates. These new measurements are compared to both models.

For the Harris-Palmgren model, it was first found that the power 2/3 over speed in the load-independent contribution is too high. An exponent 0.51 seems more suitable. The viscosity at the power 2/3 is however in good agreements with experiments. The model is also in good agreement with an increase in radial load, when the multiplication factor is adapted. The influence of oil flow rate on resistive torque depends on the oil injection temperature: at low temperature, an increase in oil flow rate implies an increase in resistive torque, whereas at high temperature it has little impact. The load-independent contribution also requires an adaptation of its multiplying coefficient. From oil injection to oil bath lubrication, the load-independent coefficient decreases by 11%. From one REB to the other, it changes by 97%.

For the SKF model, the shaft speed to the power 2/3 is already dampened by the replenishment factor. However, this factor also reduces the impact of high viscosities, which underpredicts resistive torque at low temperature. The aerodynamical drag has been suppressed, its evolution towards speed being incoherent with measurements. The radial load in the rolling contribution requires a threshold, as low load experiments still produce a non-neglectable amount of heat. The influence of load is too strong when considering both the rolling and sliding contributions. Either the first one is load independent, or the other one is null. The impact of oil flow rate is not investigated for this model. From one REB to the other, the rolling multiplying coefficients also needed to be adapted, but only by 34%.

The third chapter has presented a thermal model in the form of a REB thermal network. The thermal model manages to reproduce dedicated temperature measurements. Results showed that the partition coefficient varies with oil injection temperature and should not be calculated analytically ahead of thermal simulations.

This model is first used to investigate the influence of oil flow rate on resistive torque. It was found that the increase of oil flow rate at low oil injection temperature lowers the temperature balance. The colder the temperature, the more the REB produces heat due to the oil viscosity. At high oil injection temperature, the role of oil flow rate in cooling the REB is counterbalanced by the heat brought in by the injection. In conclusion, heat production mechanisms are independent from oil flow rate within the limits of this study.

The thermal model is then used to simulate both tested REBs. The thermal behaviours of both REBs are similar. Thus, the influence of geometry on thermal behaviour is not sufficient to explain the model discrepancies. The analytical formula for the rolling phenomenon is extrapolated to the whole REB. A new formula based on this development and on the Harris-Palmgren load-independent contribution is provided. It offers similar results compared to the SKF model. Yet, it provides a more universal method

to take into account geometry as it uses not only the bore diameter but also the number of rolling elements and their diameter.

As a conclusion, some questions remain on the simplicity of adapting the SKF model to the present experimental result: some terms are modified, others are suppressed, some still need modifications such as the replenishment factor and the sliding contribution. In the case of aeronautical REBs, such as the ones used in helicopter gearboxes which are uncommon ones, the use of the modified SKF model with its catalogue-based coefficients is problematic.

Conversely, the Harris-Palmgren is proven genuinely adaptable to experiments. Only one coefficient is needed to fit the load-independent contribution. With the new geometry formulation, this contribution can adapt to both tested REBs with a single coefficient within 20% maximal error.

The created thermal model can be integrated in more complex thermal simulation. It has already been tested for a helicopter tail gearbox, integrating a gear set and two pairs of preloaded angular ball bearings. The REB thermal model using only four node per REB is used coupled with the Harris-Palmgren model. Figure II.1 shows the partition coefficient obtained from this simulation [99].

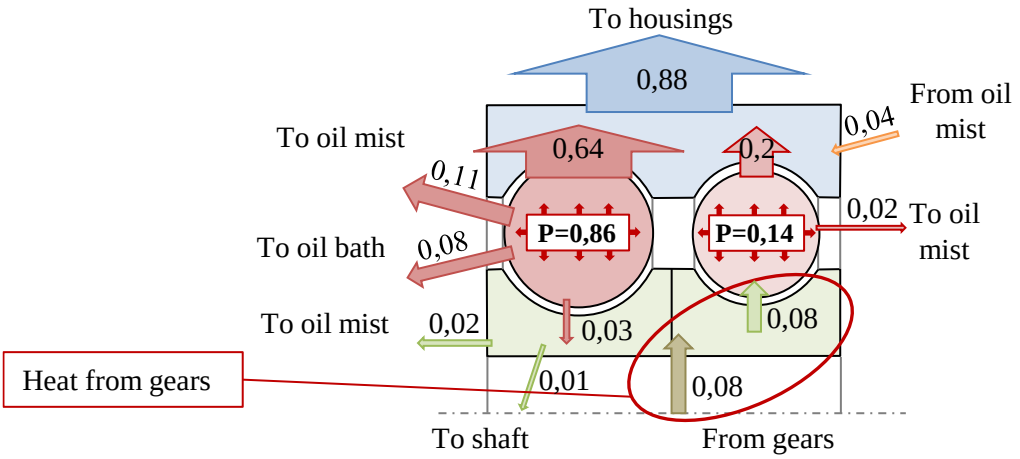

Figure II.1: Partition coefficients for a dual angular ball bearings in an helicopter tail gearbox application [99].

The use of the developed model brings insight of how the gears brought heat to the bearings *via* the shaft. This integration should now be applied to helicopter mean gearbox simulations.

The new geometric formulation is still too dependent on REB bore diameter. The 20% error using the same f_0 parameter can still be enhanced. To do so, the author suggests an analytical investigation on the film thickness replenishment factor. Indeed, the Harris-Palmgren model needed its speed exponent to be changed from its 2/3 value. This exponent has proved correct for the viscosity and is present in both models and in the

analytical rolling traction force. The SKF rolling contribution replenishment factor seems a more adequate method to correct the impact of high speed on resistive torque. The bore diameter influences the equivalent radii of contact and it can be intuited that a larger REB undergoes higher starvation mechanisms.

One of the remaining interrogations is the influence of geometry on the Harris-Palmgren load-dependent contribution (or for the SKF sliding contribution in that matter). A specific campaign should be conducted to be able to validate the linearity of this contribution with REB bore diameters. The SKF sliding contributions should be investigated at low-speed, high-load conditions to justify its regime partition function.

Finally, this work has been focused only one deep groove ball bearings. A new tested REB housing, integrating an angular ball bearing and/or a cylindrical roller bearing has been developed. Its purpose is to test the thermal behaviour of axially loaded ball bearings in tandem, of radially loaded ball bearing, and of radially loaded cylindrical roller bearing. The global models will be used to adjust its empirical parameters on specific aeronautical REBs in order to be used in helicopter gearboxes.

Appendix

Appendix A: Theoretical speeds

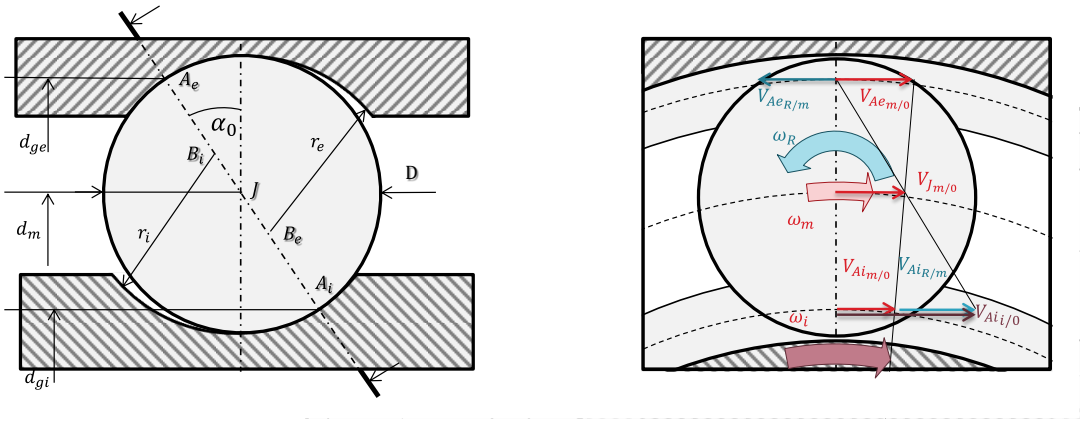

a. Cross sectional view ***b. Speed vector equilibrium***

Figure A.1 : Scheme of an angular ball bearing

Rolling element bearings transform a single rotation between solids that would imply sliding into several rotations that will prevent excessive sliding. The rolling elements rotate around their own axis and also have an orbital motion around the shaft axis. The points A and B respectively stands for the points of contacts and the ring groove curvature centres represented in Figure A.1.a. The diameters d_{ge} and d_{gi} are dependent of geometrical ratio γ. The inner ring linear and the outer ring linear speed are presented in Equations (A.1) and (A.2). The subscripts m, R respectively stand for the orbital motion and the element own rotation, the subscripts i, e respectively stand for the inner and outer ring.

$$V_{Ai_{i/0}} = V_{Ai_{R/0}} + V_{Ai_{m/0}} \qquad \text{(A.1)} \qquad V_{Ae_{e/0}} = V_{Ae_{m/0}} - V_{Ae_{R/0}} \qquad \text{(A.2)}$$

In most application, the outer ring is in fixed position, and the inner ring rotates at the shaft speed. Considering point contact and steady-state conditions, rolling without sliding is achieved if the balance of speed is preserved. A scheme of speed equilibrium for ball bearing is found on Figure A.1.b. The obtained equation for the rolling speed V_R is given in (A.3).

$$V_{Ae_{e/0}} = V_{Ai_{i/0}} = V_R = \frac{1}{4} \cdot \omega_i \cdot d_m \cdot (1 - \gamma^2) \qquad \text{(A.3)}$$

The following equations (A.4) and (A.5) are respectively for the theoretical orbital rotation and elements own rotation [10].

$$\omega_m = \frac{1}{2}\omega_i \cdot (1 - \gamma) \qquad \text{(A.4)} \qquad \omega_R = \frac{1}{2}\omega_i \cdot \frac{d_m}{D}(1 - \gamma^2) \qquad \text{(A.5)}$$

Appendix B: Sliding mechanisms

Rolling without sliding does not systematically occur in rolling element bearing. Understanding the amount of sliding is essential for different reasons. First, sliding between loaded surfaces will result in wear. It can also increase other fatigue mode such as pitting, micro-pitting, spalling, *etc*. Sliding may also result in severe dynamical problems, such as vibrations, noise, cage failure. Sliding will also produce friction increasing the amount of heat generated. The emphasis will be put on the different sliding mechanisms here.

3.6.1 Macro sliding

The first cause of sliding is the skidding of the rolling elements. Skidding occurs when the rolling elements failed to reach their theoretical speed value and are late compared to the raceway motions.

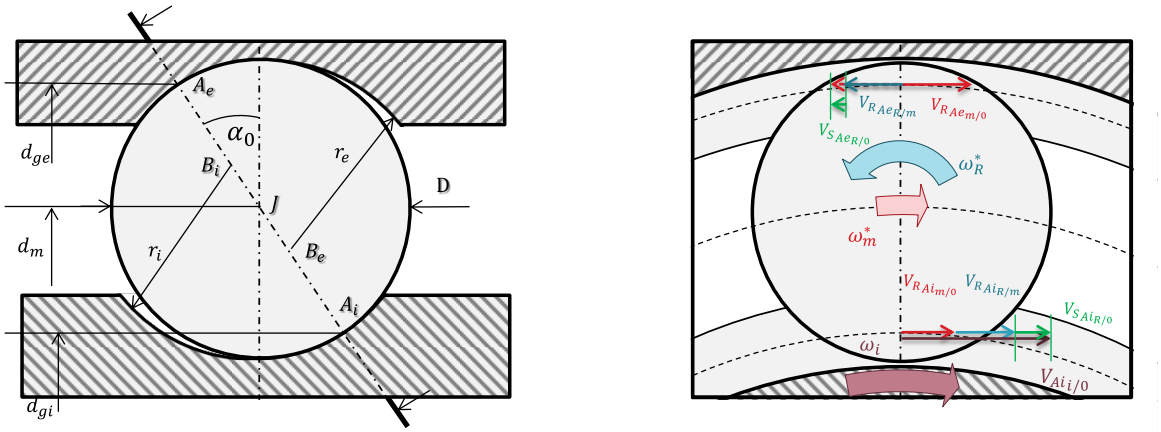

Figure B.1: Cross sectional view of an angular ball bearing with skidding speed reppresented

Sliding then occurs at the inner ring contact and/or at the outer ring contact. This macro phenomenon is represented on Figure B.1. This lateness is due to the rolling resistance exerted by other friction mechanisms such as drag or rolling. The total sliding over the ellipse will create traction forces opposed to the sliding motion. The more the REB is loaded, the less sliding is required to induce the traction forces necessitated to reach the theoretical equilibrium [67]. The rotation vectors ω_m^* and ω_R^* are inferior to their theoretical values. Assuming the outer ring is fixed and the inner ring rotates at the shaft speed, equation (B.6) and (B.7) can be obtained for the linear speed at both rings.

$$V_{S_{Ai_{R/0}}} = V_{R_{Ai_{i/0}}} - V_{R_{Ai_{R/m}}} - V_{R_{Ai_{m/0}}} \quad \text{(B.6)} \qquad V_{S_{Ae_{R/0}}} = V_{R_{Ae_{R/m}}} - V_{R_{Ae_{m/0}}} \quad \text{(B.7)}$$

3.6.2 Micro-sliding

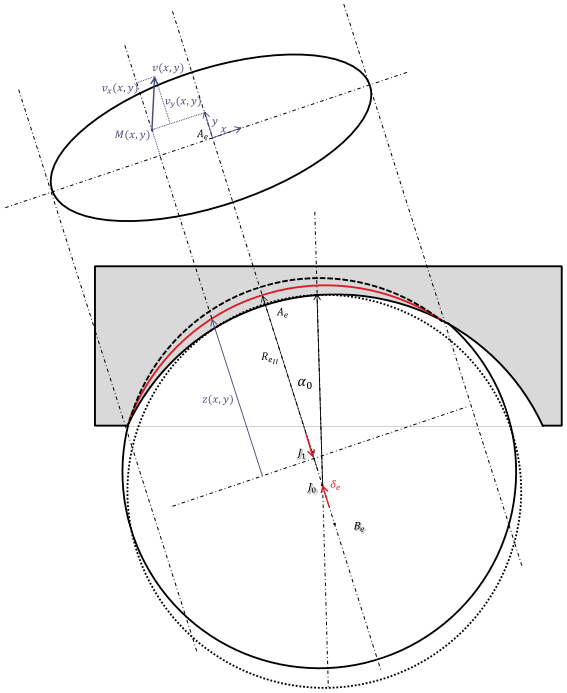

Figure B.2: Scheme of contact ellipse with micro-sliding

Additionally, because absolute point contact does not actually occur between the raceway and the elements, some sliding occurs over the contact ellipse. Due to deformation of the surfaces, the radii of contact are not constant over the contact ellipse. A representation of this phenomenon is given in Figure B.2. Assuming rolling without sliding from a point contact will only induce two point of rolling without sliding over the contact ellipse. Between these two points the radii will be shorter than expected leading to sliding opposed to the rolling speed. Outside the two points, the radii will be longer than expected leading to some sliding in the direction of rolling.

3.6.3 Spinning

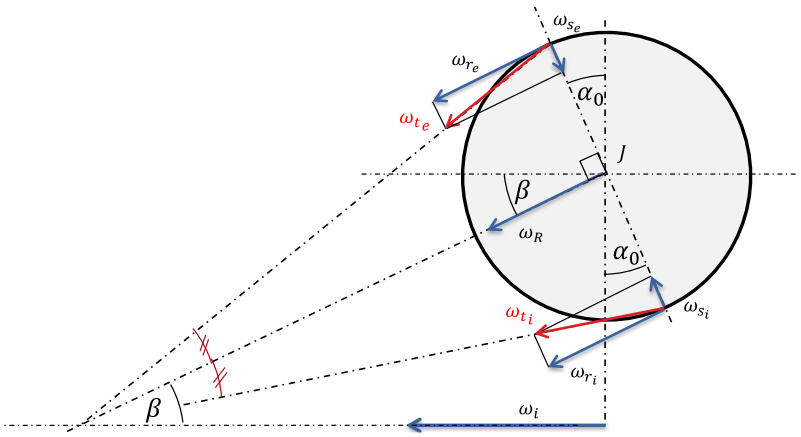

Figure B.3: Minor spinning vector equilibrium for equal contact angle

Moreover, in ball bearing with nonzero contact angles, some spinning occurs at both raceways. In Figure B.3, it can see that the ball own rotation vector ω_R, which takes place at the ball center is sequent with the shaft axis forming a pitch angle β. The contacts rotation vectors must intersect the shaft axis at this intersection. The total rotation vector at both raceways ω_{t_i} and ω_{t_e} are therefore formed from the projection of the ball own rotation ω_R. The total rotation vectors can again be projected to form rolling vectors tangent to the surface ω_{r_i} and ω_{r_e} and spinning vectors perpendicular to it ω_{s_i} and ω_{s_e}. Assuming that both contacts keep the same contact angles α_0 leads to a pitch angle β equal to α_0, and therefore to $\omega_{r_i} = \omega_{r_e} = \omega_R$. It also leads to an equal amount of spinning at both raceways $\omega_{s_i} = \omega_{s_e} = \omega_S$. It can be shown that the ratio of spin-to-roll is only dependent on geometry (Equation (B.8)). This spinning vector will generate sliding speed over the contact ellipse.

$$\frac{\omega_S}{\omega_R} = \frac{D}{d_m} \cdot \sin(\alpha_0) \tag{B.8}$$

If the centrifugal force imbalances the contact angles, the pitch angle is no longer equal to the contact angles. To reach motion equilibrium, additional spinning must occur at inner ring, outer ring or both rings. An example of spinning vector equilibrium for outer raceway control is presented in Figure B.4.

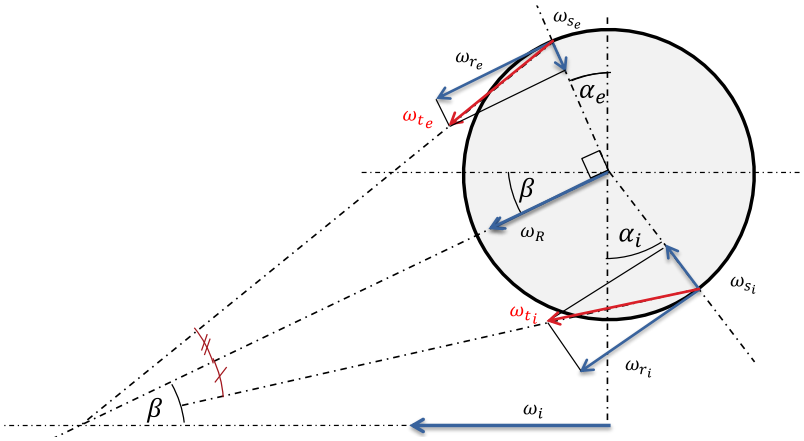

Figure B.4: Major Spinning vector equilibrium for non-equal contact angle with outer raceway control theory

3.6.4 Gyroscopic motion

Because the balls roll around an axis that is orbiting around the REB axis, a gyroscopic moment is generated, that will eventually generate a third rotation represented in Figure B.5. However, gyroscopic motion happens only if the gyroscopic moment is higher than the friction resistance. Most researches have neglected it in the past [10,67,100]. Both spinning speed and gyroscopic resistances are implied in the

concept of raceway control as defined by Jones[100]. Jones and Harris defined a leading raceway where the spinning is null and which resists the gyroscopic moment around the ball [10].

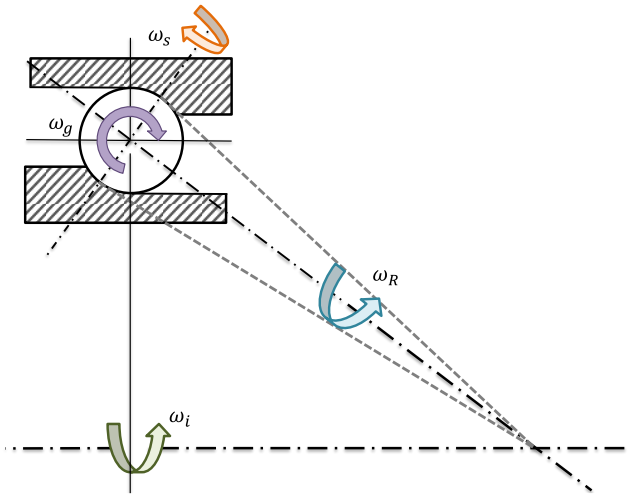

Figure B.5: Rolling, spinning and gyroscopic vectors

At low rotational speed, the leading raceway is the inner ring. As the rotational speed increases, the centrifugal forces press the ball against the outer race. At a specific threshold, the controlling raceway switches to the outer race. Another study considered Alembert's principle to establish a relationship between pitch angle and contacts angles without considering a leading raceway [101,102]. A survey of these methods can be found here[103].

Appendix C: Quasi-static Equilibrium

To understand how REBs carry a loading, some motion of theory of elasticity is required. The deformation between two solid body was first study by Boussinesq in the manner of a semi-infinite problem of point contact [104]. The problem must be transposed to an equivalent contact between a cylindrical, spherical or elliptical body against a flat body. Equivalent radii are therefore defined depending on the two bodies original radii. A differentiation can be made between roller bearings which have linear contact and ball bearings which have elliptical contact. The designs of roller bearing are not exactly cylindrical but slightly barrel shaped. Only elliptical contact theory is presented here. The contact between the inner ring and the balls is conform in the direction of rolling and is not conform in the direction of rolling. On the other hand, the contact between the outer ring and the balls is conform in both directions. The resultant equivalent radius are shown from equation (C.1) to (C.6) and represented in Figure C..

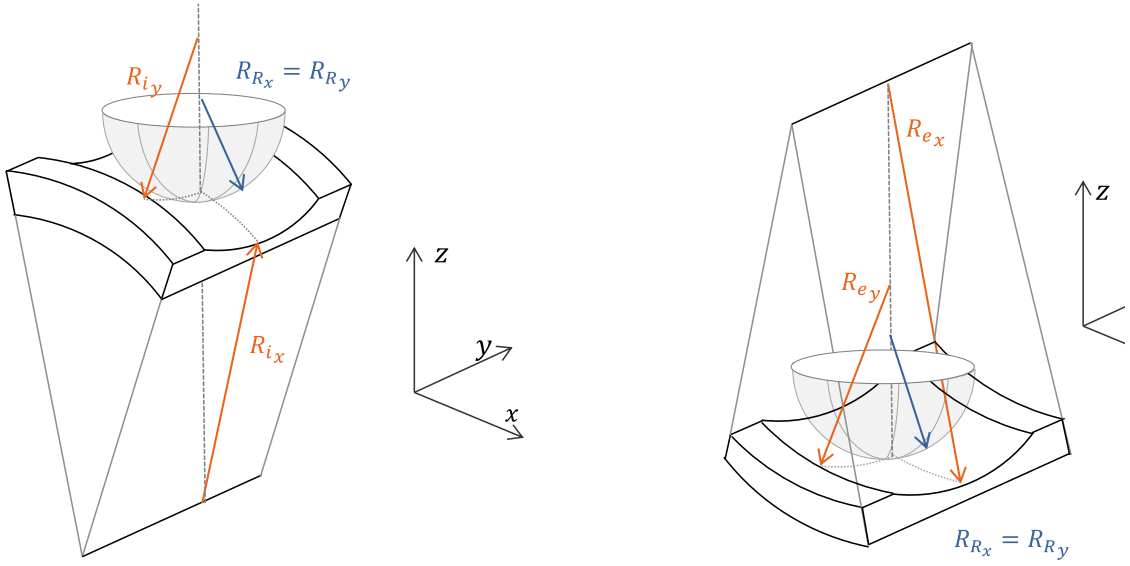

a. Inner ring contact ***b. Outer ring contact***

Figure C.1: Three dimensional scheme of raddii in ball bearings

$$R_{R-i_x} = \left(\frac{1}{R_{R_x}} + \frac{1}{R_{i_x}}\right)^{-1} = \frac{D}{2} \cdot \frac{(1-\gamma)}{(1-\gamma) + D/d_m} \quad \text{(C.1)}$$

$$R_{R-e_x} = \left(\frac{1}{R_{R_x}} - \frac{1}{R_{e_x}}\right)^{-1} = \frac{D}{2} \cdot \frac{(1+\gamma)}{(1+\gamma) - D/d_m} \quad \text{(C.2)}$$

$$R_{R-i_y} = \left(\frac{1}{R_{R_y}} - \frac{1}{R_{i_y}}\right)^{-1} = \frac{D}{2} \cdot \frac{2 \cdot f_i - 1}{2 \cdot f_i} \quad \text{(C.3)}$$

$$R_{R-e_y} = \left(\frac{1}{R_{R_y}} - \frac{1}{R_{e_y}}\right)^{-1} = \frac{D}{2} \cdot \frac{2 \cdot f_e - 1}{2 \cdot f_e} \quad \text{(C.4)}$$

$$R_{R-i} = \left(\frac{1}{R_{R-i_x}} + \frac{1}{R_{R-i_y}}\right)^{-1} \quad \text{(C.5)}$$

$$R_{R-e} = \left(\frac{1}{R_{R-e_x}} + \frac{1}{R_{R-e_y}}\right)^{-1} \quad \text{(C.6)}$$

Concerning the contact between two cylinders, Hertz showed that the distribution of pressure must be parabolic as represented inFigure C.2. The same methodology was applied to the contact between two ellipsoids [10]. He was able to create a formulation to link deformation to the load shown in equation (C.7). He also computed the characteristics of the contact area (equations (C.8) and (C.9)) and the pressure distribution (equation(C.10)). These formulations depend on dimensionless coefficients $\delta_{i,e}^*$, $a_{i,e}^*$ and $b_{i,e}^*$that can be found in a dedicated table found in anexe.

$$\delta_{i,e} = \delta_{i,e}^* \left(\frac{4\pi^2}{9R_{R-i,e}} \cdot \left(\frac{Q_{i,e}}{E_{equ}} \right)^2 \right)^{1/3} \quad \text{(C.7)}$$

$$a_{i,e} = a_{i,e}^* \left(\frac{3\pi \cdot R_{R-i,e} \cdot Q_{i,e}}{2E_{equ}} \right)^{1/3} \quad \text{(C.8)}$$

$$b_{i,e} = b_{i,e}^* \left(\frac{3\pi \cdot R_{R-i,e} \cdot Q_{i,e}}{2E_{equ}} \right)^{1/3} \quad \text{(C.9)}$$

$$p_{i,e}(x,y) = \frac{3}{2} \cdot \frac{Q_{i,e}}{\pi \cdot a_{i,e} \cdot b_{i,e}} \left(1 - \left(\frac{x}{a_{i,e}} \right)^2 - \left(\frac{y}{b_{i,e}} \right)^2 \right)^{1/2} \quad \text{(C.10)}$$

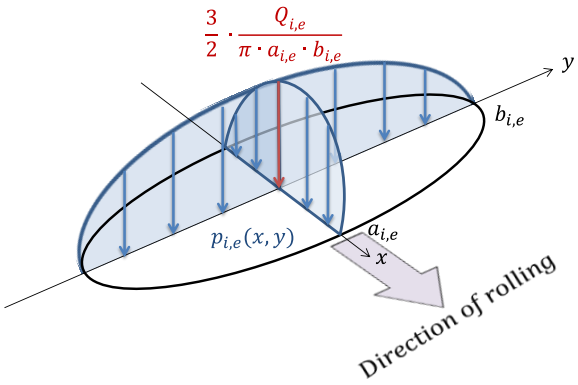

Figure C.2: Ellipse of contact

Inversing equation (C.7), Harris simplified the formulae for two steel contact bodies by introducing a deflection coefficient $K_{n_{i,e}}$ (equation (C.12)). The normal loading of each rolling can therefore be linked to its displacement (equation (C.11)).

$$Q_{i,e} = K_{n_{i,e}} \cdot {\delta_{i,e}}^{\frac{3}{2}} \quad \text{(C.11)}$$

$$K_{n_{i,e}} = 2.15 \cdot 10^5 \cdot \sqrt{R_{R-i,e}} \cdot {\delta_{i,e}^*}^{-3/2} \quad \text{(C.12)}$$

Having emphasis how a rolling element deforms to carry a normal load, the matter of how the loads are distributed among each rolling elements will be briefly discussed. Rolling element bearings are used to support an axial thrust, a radial load or both. They can also accommodate a certain amount of bending moment due to shaft misalignment or to cantilevered loads. The rolling elements are equally dispatched along the REB with an angle ψ. The loading of each rolling elements Q_ψ is more or less intense depending on their position towards the radial loadings, whereas for axial loading, the elements are equally loaded. The displacement of each rolling elements δ_ψ is ruled by geometric relationships, which link the axial, radial and angular displacement of the shaft to each rolling element own displacement. An example of such distribution is shown on Figure C.3 for combined axial and radial load.

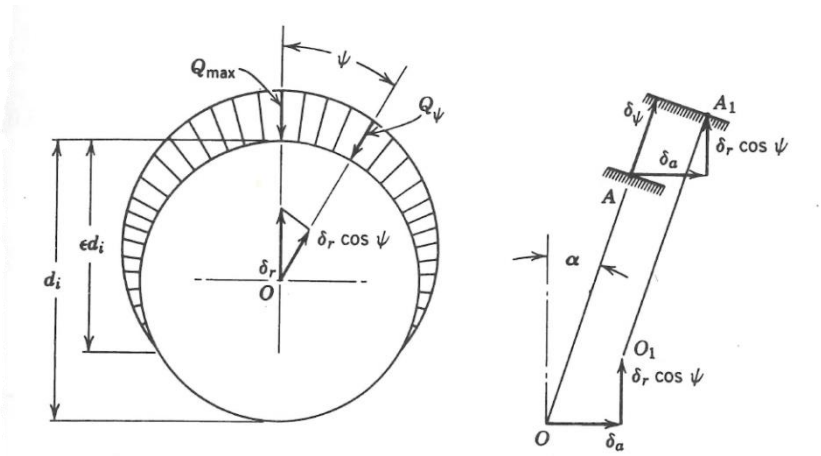

Figure C.3: Ball displacements in case of angular ball bearing in combined axial and radial loads [10]

In the quasi-static approach, the load distribution equilibrium is calculated by computing the displacement each element undergoes to reach the REB equilibrium. The associated force equations are referred in equations (C.13), (C.14)and (C.15).

$$F_r = \sum_{j=1}^{n} Q_j * \cos(\alpha_j) * \cos(\psi_j) \tag{C.13}$$

$$F_a = \sum_{j=1}^{n} Q_j * \sin(\alpha_j) \tag{C.14}$$

$$M_y = \sum_{j=1}^{n} r_j * Q_j * \sin(\alpha_j) \tag{C.15}$$

Efforts are transmitted to the element along the contact angles. Either the inner ring or the outer ring is also isolated to provide additional equations. In pure axial loading, the problem is axisymmetric, and the real contact angle is iteratively computed. In pure radial loading, contact angle is supposed constant. As the shaft speed increases, the centrifugal load imbalances the contact angles as seen in Figure C.4. The load distribution will then depend on speed and the problem is not quasi-static any longer.

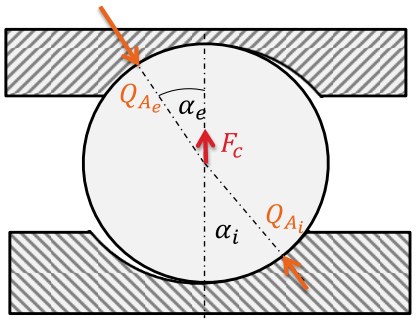

Figure C.4: Effect of centrifugal force on contact angles

Appendix D: REB motion equilibrium without centrifugal forces

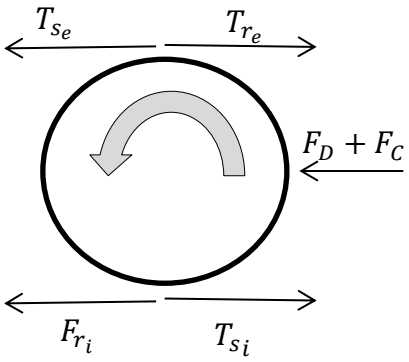

Figure D.1: Traction forces equilibrium over a rolling element

The motion equilibrium over a rolling element is showed on Figure D.1. The hydrodynamical rolling forces $T_{r_{i-e}}$ act as resistive forces that prevent the rolling motion. The drag force F_D and cage force F_C counteract the orbiting motion. In consequence, the previously mentioned skidding occurs at the raceway contact generating macro sliding. To balance these resisting forces acting on the rolling element, traction forces are present and referred here as $T_{s_{i-e}}$. These forces are opposed to the direction of the sliding speeds. When the contact angles are identical, the quasi-static approach can be made, and the direction of the load equilibrium is orthogonal to the direction of the motion equilibrium, the direction of rolling.

$$T_{s_e} + T_{r_i} + F_D + F_C - T_{r_e} - T_{s_i} = 0 \tag{D.1}$$

$$\frac{1}{2} D \cdot (T_{s_e} + T_{s_i} - T_{r_e} - T_{r_i}) = 0 \tag{D.2}$$

On equation (D.1), the force equilibrium on the rolling direction is presented. On equation (D.2), the torque equilibrium on the ball axis of rotation is presented. Both assume no acceleration nor deceleration from the rolling element.

$$T_e = F_{r_e} - \frac{1}{2}(F_D + F_C) \tag{D.3}$$

$$T_i = F_{r_i} - \frac{1}{2}(F_D + F_C) \tag{D.4}$$

These two equations lead to equations (D.3) and (D.4) where it can be seen that the traction forces are dependent on the rolling, drag and cage forces. The required sliding speed can be calculated from the traction forces using a reverse method. At relatively low speed, the cage and drag forces are low compared to the rolling forces, leading to assuming the traction as equal to the rolling forces [105].

Annex E: REB equilibrium scheme

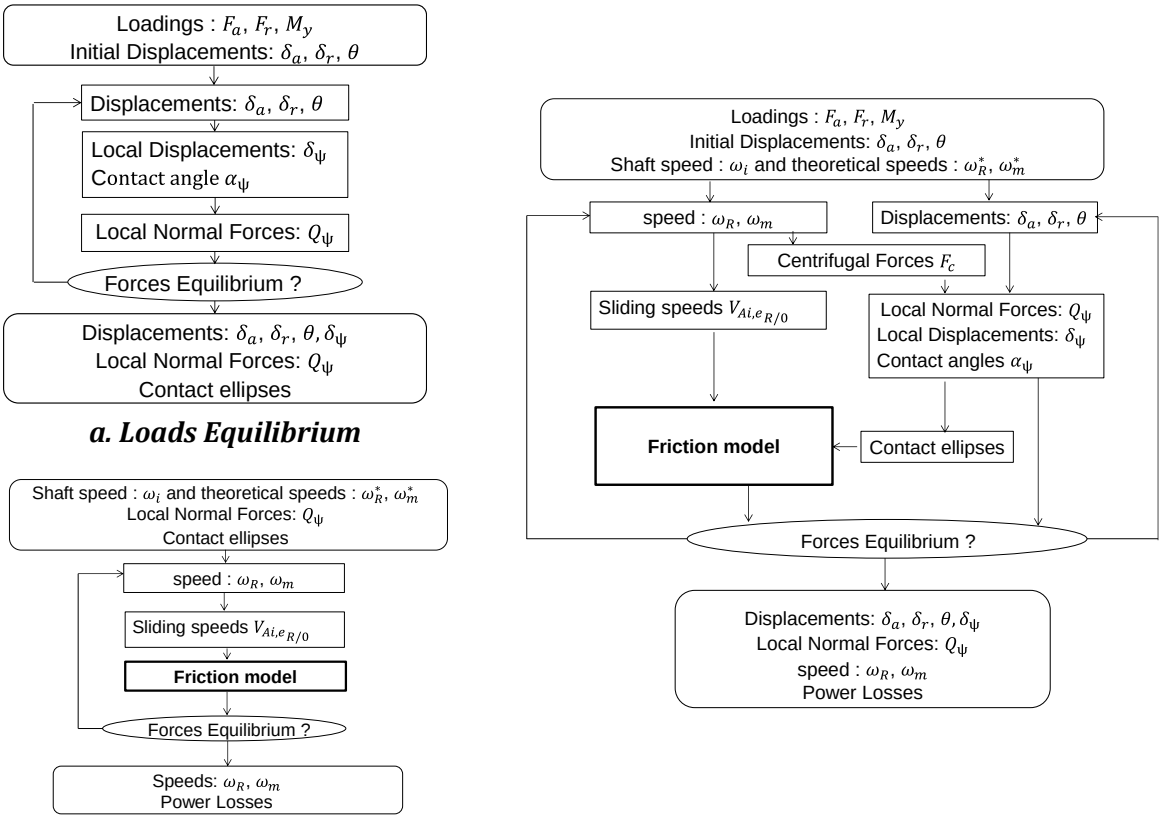

Figure E.1: Different equilibrium schemes

At high rotational speed, the force equilibrium depends on the centrifugal force and on the gyroscopic motion. If the gyroscopic motion is often neglected, the centrifugal force can be important. Because it depends on the orbiting speed of the rolling elements, it depends on the traction-motion equilibrium. Therefore, at high speed the quasi-static approach must consider motion and traction equilibrium and in conversely, neglecting the centrifugal force leads to separate the quasi-static equilibrium from the speed and traction equilibrium. Both methods are detailed in Figure E.1. Jones modelled this quasi-static approach, and later Harris detailed it so that it is known as the Jones-Harris Model [100,106]. Further works have been done to elaborate more complex models for the REB equilibrium, including cage equilibrium, stiffness matrix, thermal expansion, and finite element analysis. A survey of their achievements is found here [107]. The quasi-static approach ends where the dynamic model begins. Transient conditions are considered as an inertia term is added to each equation. One of the reasons to model a REB dynamically is to grasp the element-cage contact mechanics that can undergo choc and vibrations. Gupta's ADORE software is the referenced of REB dynamic modelling[52].

Annex F: Thin Efficiency Resistance Calculus

When modelling the heat exchange between the housing to the air, some of the heat finds its path through the test rig marble. The large surface cannot be considered as isothermal. The heat exchange depends on the heat exchange coefficient evolving from its centre where is housing rests to its tip where it is supposed null. In order to model it, a thin efficiently is calculated to reduce the actual surface to take into account:

$$\eta = \frac{\tanh\left(\sqrt{\frac{h_1 + h_2}{k_{solid} \cdot e}} \cdot L\right)}{\sqrt{\frac{h_1 + h_2}{k_{solid} \cdot e}} \cdot L} \tag{F.1}$$

In this formula, h_1 and h_2 are respectively the upper and lower convective heat transfer coefficient. In the present case, they are both equal and calculated with the Nusselt number with Equation (3.12). k_{solid} is the conductivity of the material, here of steel, e is the thickness of the marble and L its characteristic length.

The equivalent resistance applied between the air node #1 and the housing #2 is therefore:

$$R_{1-2} = \frac{L}{\eta \cdot A \cdot k_{air} \cdot N_u} \tag{F.2}$$

Durand de Gevigney applied this fin efficiency to model his test rig marble in [83]

Appendix G: Rolling Analytical formulation

G.1 General formulation

In an EHD contact, integrating the pressure gradient t the contact inlet leads to consider a force acting on the rolling element, tangent to the surfaces and opposed to the surfaces motion directions. The purpose of this annex is to extrapolate from this theoretical tangential force a global resistive torque and to compare it to the global model examined in chapter 2. The formulation of the rolling resistance force T_r is presented in the form of an integral by Dowson Higginson in the equation (G.1) [108].

$$T_r = \frac{1}{2}\int_{-a}^{a} h(x) \cdot \frac{\partial P(x)}{\partial x} \cdot dx \tag{G.1}$$

Houpert extrapolated Tevararwerck's law, itself issued from a private communication with Hamrock [3,38,40] The formula for the rolling traction force is dependent on classical parameters G U and W as seen in equation (G.2):

$$T_r = 2.86 \cdot E' \cdot R_x^2 \cdot G^{0.022} \cdot U^{0.66} \cdot W^{0.47} \cdot k^{0.348} \tag{G.2}$$

Assuming rolling without sliding on both rings, the linear speeds are equal at both ring and given in equation (A.1). By expressing the classical parameters, the traction force formulation can be developed as in equation (G.3).

$$\begin{aligned} T_r = 1.15 \\ \cdot E'^{-0.108} \\ \cdot R_x^{0.4} \\ \cdot \alpha^{0.022} \\ \cdot (\eta_{oil} \cdot \omega_i \cdot d_m)^{0.66} \\ \cdot Q_A^{0.47} \\ \cdot (1-\gamma^2)^{0.66} \\ \cdot k^{0.348} \end{aligned} \tag{G.3}$$

The geometrical parameters are now developed for both inner and outer ring. The equivalent radius in the direction of rolling are defined in equation (C.1) and (C.2). The ellipticity is equal to the ratio of equivalent radii in both directions $k_i = \frac{2f_i}{2 \cdot f_i - 1} \cdot \frac{1}{1-\gamma}$ and $k_e = \frac{2f_e}{2 \cdot f_e - 1} \cdot \frac{1}{1+\gamma}$. The equation for the rolling traction force now differs from the inner ring to the outer ring, and equations (G.4) and (G.5) are presented for both.

$$\begin{aligned} T_{r_i} = 0.87 \\ \cdot E'^{-0.108} \\ \cdot D^{0.4} \\ \cdot \alpha^{0.022} \\ \cdot (\eta_{oil} \cdot \omega_i \cdot d_m)^{0.66} \\ \cdot Q_A^{0.47} \\ \cdot (1+\gamma)^{0.66} \\ \cdot (1-\gamma)^{0.712} \end{aligned} \tag{G.4}$$

$$\cdot \left(\frac{2f_i}{2f_i-1}\right)^{0.348}$$

$$\begin{aligned} T_{r_e} = 0.87 \\ \cdot E'^{-0.108} \\ \cdot D^{0.4} \\ \cdot \alpha^{0.022} \\ \cdot (\eta_{oil} \cdot \omega_i \cdot d_m)^{0.66} \\ \cdot Q_A^{0.47} \\ \cdot (1-\gamma)^{0.66} \\ \cdot (1+\gamma)^{0.712} \\ \cdot \left(\frac{2f_e}{2f_e-1}\right)^{0.348} \end{aligned} \tag{G.5}$$

G.2 Formulation of the normal load Q_A

In the case of a radial loading, the load on each rolling element Q_A depends on its angular position ψ thanks to a distribution function $f(\epsilon\,;\psi)$ described in equation (G.6)[10]. The relationship between the load on each rolling element Q_A and the maximum load Q_{max} is presented in equation (G.7). The maximum load Q_{max} depends on the applied radial load F_r, the number of rolling element Z, the contact angle α_0 and a damping function dependent on the diametral clearance $J_r(\varepsilon)$ in equation (G.8). Therefore, for both inner and outer ring the load on each ball Q_A can be expressed depending on the applied radial load F_r in (G.9).

$$f(\epsilon\,;\psi) = 1 - \frac{1}{2\epsilon}(1-\cos(\psi)] \tag{G.6}$$

$$Q_A = Q_{max} \cdot f(\epsilon\,;\psi)^{1.5} \tag{G.7}$$

$$Q_{max} = \frac{F_r}{J_r(\varepsilon) \cdot Z \cdot \cos(\alpha_0)} \tag{G.8}$$

$$Q_A = \frac{F_r \cdot f(\epsilon\,;\psi)^{1.5}}{J_r(\varepsilon) \cdot Z \cdot \cos(\alpha)} \tag{G.9}$$

Eventually, the rolling force acting on each rolling element can be expressed with the shaft speed ω_i, dynamic viscosity η_{oil}, radial loading F_r and multiple geometrical parameters in equation (G.10) and (G.11). The angular position only influences a loading distribution function $f(\epsilon\,;\psi)$.

$$\begin{aligned} T_{r_i}(\psi) = 0.87 \\ \cdot E'^{-0.108} \\ \cdot D^{0.4} \\ \cdot \alpha^{0.022} \\ \cdot (\eta_{oil} \cdot \omega_i \cdot d_m)^{0.66} \\ \cdot F_r^{0.47} \\ \cdot (1+\gamma)^{0.66} \\ \cdot (1-\gamma)^{0.712} \end{aligned} \tag{G.10}$$

$$\cdot \left(\frac{2f_i}{2f_i-1}\right)^{0.348} \cdot (J_r(\varepsilon)\cdot Z\cdot\cos\alpha)^{-0.47} \cdot f(\epsilon\,;\psi)^{0.705}$$

$$T_{r_e}(\psi) = 0.87 \cdot E'^{-0.108} \cdot D^{0.4} \cdot \alpha^{0.022} \cdot (\eta_{oil}\cdot\omega_i\cdot d_m)^{0.66} \cdot Q_r^{0.47} \cdot (1-\gamma)^{0.66} \cdot (1+\gamma)^{0.712} \cdot \left(\frac{2f_e}{2f_e-1}\right)^{0.348} \cdot (J_r(\varepsilon)\cdot Z\cdot\cos\alpha)^{-0.47} \cdot f(\epsilon\,;\psi)^{0.705} \quad \text{(G.11)}$$

G.3 Formulation of a total resistive torque

The power losses are calculated at each contact by multiplying the rolling force by the rolling speed. The total power loss due to rolling is sum up afterwards in equation (G.12). As it was proven before on Annex E, when drag force and cage force are neglected, the sliding traction force is equal to the rolling traction force in order to reach the motion equilibrium. The global influence of rolling friction has been multiplied by two in consequence. Afterwards, the total power losses are divided by the shaft speed to calculate the total resistive torque applied on the shaft in equation (G.13).

$$P_{r_{i-e}} = 2\cdot\sum_{j=1}^{Z} T_{r_{i-e}}(\psi_j)\cdot u_{r_{i-e}} = 2\cdot\frac{1}{4}\cdot\omega_i\cdot d_m\cdot(1-\gamma^2)\cdot\sum_{j=1}^{Z} T_{r_{i-e}}(\psi_j) \quad \text{(G.12)}$$

$$M_{r_{i-e}} = \frac{P_{r_i-e}}{\omega_i} = \frac{1}{2}\cdot d_m\cdot(1-\gamma^2)\cdot\sum_{j=1}^{Z} T_{r_i-e}(\psi_j) \quad \text{(G.13)}$$

It can be noticed that the total power loss is easily expressed with a single formula as the rolling forces at each ball are independent on ball location, except for loading distribution function $f(\epsilon\,;\psi)$. Svorjall already resolved the loading distribution sum in the form of an integration presented in (G.14)[109] .

$$\sum_{j=1}^{Z} f(\epsilon\,;\psi)^{\beta} = \frac{Z}{2\pi}\cdot\int_{-\pi}^{+\pi} f(\epsilon\,;\psi)^{\beta}d\psi = Z\cdot J_a(\epsilon\,,\beta\,) \quad \text{(G.14)}$$

However, Svorjall's integral only described the case were the exponent $\beta = 1.5$. Here, a numerical method based on trapeze integration is used. The values were computed for $J_a(\epsilon\,,1.5)$ and ϵ between 0.1 and 5 which verifies the validity of the integration compared to Svorjall's tables found in [109]. When considering no diametral

clearance $\varepsilon = 0$, then the parameter $\epsilon = 0.5$. Given the expression of the rolling force in (G.10) and (G.11), $\beta = 0.705$. The integral in this scenario was calculated in (G.15)

$$\frac{1}{2\pi}\int_{-\pi}^{+\pi} f(0.5\,;\psi)^{0.705} d\psi = 0.3458 \tag{G.15}$$

The total resistive torque for both inner ring and outer ring can therefore be calculated independently of each ball angular position.

$$\begin{aligned} M_{r_i} = 0.0343 \\ &\cdot E'^{-0.108} \\ &\cdot D^{0.4} \\ &\cdot \alpha^{0.022} \\ &\cdot (\eta_{oil} \cdot \omega_i)^{0.66} \\ &\cdot Q_r^{0.47} \\ &\cdot (1+\gamma)^{1.66} \\ &\cdot (1-\gamma)^{1.712} \\ &\cdot \left(\frac{2f_i}{2f_i-1}\right)^{0.348} \\ &\cdot \cos\alpha^{-0.47} \\ &D^{0.4} \\ &\cdot Z^{0.53} \\ &\cdot d_m^{1.66} \end{aligned} \tag{G.16}$$

$$\begin{aligned} M_{r_e} = 0.0343 \\ &\cdot E'^{-0.108} \\ &\cdot D^{0.4} \\ &\cdot \alpha^{0.022} \\ &\cdot (\eta_{oil} \cdot \omega_i)^{0.66} \\ &\cdot Q_r^{0.47} \\ &\cdot (1-\gamma)^{1.66} \\ &\cdot (1+\gamma)^{1.712} \\ &\cdot \left(\frac{2f_e}{2f_e-1}\right)^{0.348} \\ &\cdot \cos\alpha^{-0.47} \\ &D^{0.4} \\ &\cdot Z^{0.53} \\ &\cdot d_m^{1.66} \end{aligned} \tag{G.17}$$

To sum both inner ring and outer ring resistive torque, a new geometry parameter $\gamma^*$is defined depending on the kinematic ratio γ in equation (G.18). It can be noted that γ^* varies between 1.6 and 2.

$$\gamma^* = (1-\gamma)^{1.712} \cdot (1+\gamma)^{1.66} + (1+\gamma)^{1.712} \cdot (1-\gamma)^{1.66} \tag{G.18}$$

Also, it can be noted that the viscosity η_{oil} should be taken at the appropriate ring temperature. It was approximated that the average viscosity at ring temperature is equal to the viscosity at the average ring temperature. This hypothesis is accurate for ring temperature difference inferior to 50°C. Moreover, the ring osculations are assumed to be equal. $f_i = f_e$.

All materials are assumed to be hardened steel and the oil piezo-viscosity to have a medium value, respectively $E' = 231 * 10^9\ Pa$ and $\alpha = 1.5 * 10^{-8}\ Pa^{-1}$. Assuming an oil density of 900 kg/m3, the total resistive torque can be expressed

$$M_r = 0.122 \cdot D^{0.4} \cdot (\nu_{oil} \cdot \omega_i)^{0.66} \cdot Q_r^{0.47} \cdot \left(\frac{2f_{i,e}}{2f_{i,e}-1}\right)^{0.348} \cdot \cos\alpha^{-0.47} \cdot Z^{0.53} \cdot d_m^{1.66} \quad \text{(G.19)}$$

G.4 Comparison with the Harris-Palmgren model load-independent contribution for deep groove ball bearing

This study focusses on a standard deep groove ball bearing, with ring osculation values $f_i = f_e = 0.52$ and contact angle $\alpha_0 = 0°$.

The Harris-Palmgren model load-dependent contribution was based using a constant ball/bore diameter of 0.2. [9]. Assuming this ratio here leads to $\gamma = 0.2$. It also leads to evaluate the number of balls, assuming the space between ball is the ball diameter $Z = \frac{\pi \cdot d_m}{D} = \frac{\pi}{0.2}$ is obtained.

The total resistive torque in (G.19) is therefore compacted into a singular formula in (G.20) depending solely on the bore diameter, the shaft speed, the viscosity and the radial load.

$$M_{r_{i-e}} = 0.0342 \cdot (\nu_{oil} \cdot \omega_i)^{0.66} \cdot d_m^{2.06} \cdot Q_r^{0.47} \quad \text{(G.20)}$$

The Palmgren model was empirically created, separating a load-dependent contribution from a load-independent one. In order to compare it with the present formula, a hypothesis over the radial load was assumed. The radial load was assumed as 10% of the static capacity. The European standard yields a formulation (Equation (G.21)) for the static capacity C_0 depending on the number of elements Z, the ball diameter D and the contact angle α_0 [98].The parameter k_0 depend on the ratio of diameter, here for $\frac{D}{d_m} = 0.2$ and 0° contact angle, $k_0 = 14$.

$$C_0 = k_0 \cdot Z \cdot D^2 \cdot cos\ \alpha_0 \cdot 10^6 \quad \text{(G.21)}$$

Having already expressed the number of rolling elements and the ball diameter depending on the groove diameter, the total resistive torque obtained is presented in (G.22):

$$M_{r_{i-e}} = 548 \cdot (\nu_{oil} \cdot \omega_i)^{0.66} \cdot d_m^{3.00} \quad \text{(G.22)}$$

Bibliography

[1] Handschuch, R. F., and Rohn, D. A., 1988, "Efficiency Testing of a Helicopter Transmission Planetary Reduction Stage," NASA Tech. Pap., **2795**(1), p. 18.

[2] Coe, H. H., 1989, "Comparison of Predicted and Measured Temperatures of UH-60A Helicopter Transmission," NASA Tech. Pap., p. 16.

[3] Tevaarwerk, J. L., and K.L. Johnson, 1979, "The Influence of Fluid Rheology on the Performance of Traction Drives," ASLE Trans. J. Lubr. Technol., **101**, pp. 266–274.

[4] Niel, D., 2019, "Etude Du Comportement Thermomécanique de Paliers à Roulements Pour Une Application Hautes Vitesses," Thèse de Doctorat - Insa-Lyon - Université de Lyon.

[5] Nelias, D., Sainsot, P., and Flamand, L., 1994, "Power Loss of Gearbox Ball Bearing under Axial and Radial Loads," Tribol. Trans., **37**(1), pp. 83–90.

[6] Jeng, Y.-R., and Huang, P.-Y., 2003, "Predictions of Temperature Rise for Ball Bearings," Tribol. Trans., **46**(1), pp. 49–56.

[7] Tian, S., Chen, X., Chen, T., and He, Y., 2019, "Experimental Analysis and Modeling of the Effects of Oil–Air Lubrication Parameters on Bearings Friction Loss of High-Speed Motorized Spindle," Tribol. Trans., **62**(3), pp. 524–534.

[8] Nélias, D., 1994, "Influence de La Lubrification Sur La Puissance Dissipée Dans Les Roulements à Rouleaux Cylindriques," Rev. Française Mécanique, **2**, pp. 143–154.

[9] Palmgren, A., 1967, *Les Roulements : Description, Théorie, Applications*, SKF inc., 2nd Edition.

[10] Harris T.A., 1998, *Rolling Bearing Analysis*, New-York, 3rd Edition.

[11] SKF, 2014, *The SKF Model for Calculating the Frictional Moment*, Göteborg, Sweden.

[12] SKF, "Using a Friction Model as an Engineering Tool" [Online]. Available: http://evolution.skf.com/us/using-a-friction-model-as-an-engineering-tool-2/. [Accessed: 01-Jan-2019].

[13] Cousseau, T., Graça, B., Campos, A., and Seabra, J., 2011, "Friction Torque in Grease Lubricated Thrust Ball Bearings," Tribol. Int., **44**(5), pp. 523–531.

[14] Fernandes, C. M. C. G., Martins, R. C., and Seabra, J. H. O., 2013, "Friction Torque of Thrust Ball Bearings Lubricated with Wind Turbine Gear Oils," Tribol. Int., **58**, pp. 47–54.

[15] Niel, D., Changenet, C., Ville, F., and Octrue, M., 2018, "A New Test Rig to Study Rolling Element Bearing Thermomechanical Behavior," Int. Gear Conf., (October), pp. 121–133.

[16] Miyakawa, Y., 1973, "Study on the Performance of Ball Bearings at High Dn Values," NASA Tech. Transl., **TT F-15**(September), pp. 1–166.

[17] Pouly, F., 2010, "Modélisation Thermomécanique d'un Roulement à Billes Grande Vitesse," Thèse de Doctorat - INSA-Lyon - Université de Lyon.

[18] Parker, R. J., 1984, "Comparison of Predicted and Experimental Thermal Performance of Angular Contact Ball Bearings," (February), pp. 1–16.

[19] Neurouth, A., Changenet, C., Ville, F., and Arnaudon, A., 2014, "Thermal Modeling of a Grease Lubricated Thrust Ball Bearing," Proc. Inst. Mech. Eng. Part J J. Eng. Tribol., **228**(11), pp. 1266–1275.

[20] Brossier, P., Niel, D., Changenet, C., and Ville, F., 2020, "Experimental and Numerical Investigations on Rolling Element Bearing Thermal Behaviour," Inst. Mech. Eng. - J. Enginerring Tribol., **Part J**, pp. 1–12.

[21] Airbus Helicopters, 2017, "H225 LN-OJF Accident Investigation Status" [Online]. Available: https://www.youtube.com/watch?v=KvBLadpVscY&feature=emb_logo. [Accessed: 11-Jun-2020].

[22] Gasparini, G., and Tamborini, M., 2015, "Design and Development Strategies for Main Gear Box Loss of Oil Performance Improvement.Pdf," 9th EASA Rotorcr. Symp.

[23] R. Stribeck, 1902, "Die Wesentlichen Eigenschaften Der Gleit Und Rollenlager," Zeitschrift des Vereines Dtsch. Ingenieure, **46**, pp. 1341–1348.

[24] Hamrock, B. J., and Dowson, D., 1976, "Isothermal Elastohydrodynamic Lubrication of Point Contacts - Part 1 - Theoretical Formulation," J. Lubr. Technol., (August), pp. 223–228.

[25] Cheng H., 1970, "A Numerical Solution of the Elastohydrodynamic Film Thickness in an Elliptical Contact," ASME Trans. J. Lubr. Technol., **92**(1), pp. 155–162.

[26] Guay, P., 2015, "Lubrification Élastohydrodynamique," Tech. l'Ingénieur, **tri1540**.

[27] Moes, H., and Bosma, R., 1972, "Film Thickness and Traction in EHL at Point Contact," *Symposeum on EHL Lubrication*, I. Mech E., pp. 149–152.

[28] Wolveridge, P. E., Baglin, K. P., and Archard, J. F., 1971, "The Starved Lubrication of Cylinders in Line Contact," *Proc Instn Mech Engrs*.

[29] Hamrock, B. J., and Dowson, D., 1977, "Isothermal Elastohydrodynamic Lubrication of Point Contacts : PartIV- Starvation Results," Trans. ASME J. Lubr. Technol., pp. 16–22.

[30] Chiu, Y. P., 1974, "An Analysis and Prediction of Lubricant Film Starvation in Rolling Contact Systems," ASLE Trans., **17**(1), pp. 22–35.

[31] Damiens, B., 2003, "Modelisation De La Lubrification Sous-Alimentee Dans Les Contacts Elastohydrodynamiques Elliptiques," Thèse de Doctorat - INSA-Lyon - Université de Lyon.

[32] Biboulet, N., Colin, F., and Lubrecht, A. A., 2013, "Friction in Starved Hydrodynamically Lubricated Line Contacts," Tribol. Int., **58**, pp. 1–6.

[33] Chevalier, F., Lubrecht, A. A., Cann, P. M. E., Colin, F., and Dalmaz, G., 1998, "Film

Thickness in Starved EHL Point Contacts," J. Tribol., **120**(1), pp. 126–133.

[34] Gershuni, L., Larson, M. G., and Lugt, P. M., 2008, "Lubricant Replenishment in Rolling Bearing Contacts," Tribol. Trans., **51**(5), pp. 643–651.

[35] Nogi, T., Shiomi, H., and Matsuoka, N., 2018, "Starved Elastohydrodynamic Lubrication with Reflow in Elliptical Contacts," J. Tribol., **140**(1), pp. 1–9.

[36] Houpert, L., 1984, "A Study of Mixted Lubrication Conditions in Modern Deep Groove Ball Bearings," *Proc. 11th Leeds-Lyon Symposium, Leeds*, pp. 55–63.

[37] Diab, Y., 2008, "Analyse Des Pertes de Puissance Dans Les Transmissions Par Engrenages," Thèse de Doctorat - INSA-Lyon - Université de Lyon.

[38] Houpert, L., 2002, "Ball Bearing and Tapered Roller Bearing Torque: Analytical, Numerical and Experimental Results," Tribol. Trans., **45**(3), pp. 345–353.

[39] Houpert, L., 1999, "Numerical and Analytical Calculations in Ball Bearings," *8th European Space Mechanisms and Tribology Symposeum*, Toulouse, p. 243.

[40] Houpert, L., and P. Leenders, 1985, "A Theoretical and Experimental Investigation into Rolling Bearing Friction," *4ème Congrès Européen de Tribologie - EUROTRIB 1985*, Ecully, pp. 2–10.

[41] Snare, B., 1968, "Rolling Resistance in Lightly Loaded Bearings," Ball Bear. J., **152**(3), p. 13.

[42] Crook, A. W., 1963, "The Lubrication of Rollers IV. Measurements of Friction and Effective Viscosity," Philos. Trans. R. Soc. A Math. Phys. Eng. Sci., **255**(1056), pp. 281–312.

[43] Towsend, D. P., Allen, C. W., and Zaretsky, E. V., 1973, "Study of Ball Bearing Torque Under Elastohydrodynamic Lubrication," *ASME/ASLE Joint Tribology Conference*, ASME.

[44] Houpert, L., 1986, "Piezoviscous-Rigid Rolling and Sliding Traction Forces, Application: The Rolling Element-Cage Pocket Contact," *ASME/ASLE Joint Tribology Conference*, Journal of Tribology, Pittsburgh.

[45] Houpert, L., 2014, "An Enhanced Study of the Load-Displacement Relationships for Rolling Element Bearings," J. Tribol., **136**(1), pp. 1–11.

[46] Zhou, R. S., and Hoeprich, M. R., 1991, "Torque of Tapered Roller Bearings," J. Tribol., **113**(3), pp. 590–597.

[47] Biboulet, N., and Houpert, L., 2010, "Hydrodynamic Force and Moment in Pure Rolling Lubricated Contacts. Part 1: Line Contacts," Proc. Inst. Mech. Eng. Part J J. Eng. Tribol., **224**(8), pp. 765–775.

[48] Biboulet, N., and Houpert, L., 2010, "Hydrodynamic Force and Moment in Pure Rolling Lubricated Contacts. Part 2: Point Contacts," Proc. Inst. Mech. Eng. Part J J. Eng. Tribol., **224**(8), pp. 777–787.

[49] Dowson, D., and Higginson, G. R., 1966, *Elasto-Hydrodynamic Lubrication : The*

Fundamentals of Roller and Gear Lubrication, Pegamon Press, First Edition.

[50] Houpert, L., 1997, "A Uniform Analytical Approach for Ball and Roller Bearings Calculations," J. Tribol., **119**(4), pp. 851–858.

[51] Olaru, D. N., and Gafitanu, M. D., 1993, "Starvation in Ball Bearings," Wear, **170**(2), pp. 219–234.

[52] Gupta, P., 2002, "Thermal Interactions in Rolling Bearing Dynamics," (April).

[53] Achenbach, E., 1972, "Experiments on the Flow Past Spheres at Very High Reynolds Numbers," J. Fluid Mech., **54**(3), pp. 565–575.

[54] Marchesse, Y., Changenet, C., and Ville, F., 2019, "Drag Power Loss Investigation in Cylindrical Roller Bearings Using CFD Approach," Tribol. Trans., **62**(3), pp. 403–411.

[55] Pouly, F., 2010, "Modélisation Thermomécanique d'un Roulement à Billes Grande Vitesse," Thèse de Doctorat - INSA-Lyon -Université de Lyon.

[56] Marchesse, Y., Changenet, C., Ville, F., and Velex, P., 2015, "Numerical Investigation of the Cage and Rings Influence on the Ball Drag Coefficient," Soc. Tribol. Lubr. Eng. Annu. Meet. Exhib. 2015, pp. 701–703.

[57] Hu, J., Wu, W., Wu, M., and Yuan, S., 2014, "Numerical Investigation of the Air-Oil Two-Phase Flow inside an Oil-Jet Lubricated Ball Bearing," Int. J. Heat Mass Transf., **68**, pp. 85–93.

[58] Adeniyi, A. A., Morvan, P., and Simmons, K. A., 2015, "A Multiphase Computational Study of Oil-Air Flow within the Bearing Sector of Aeroengines," *Proccedings of ASME Turbo Expo*, Montréal, pp. 1–10.

[59] Wu, W., Hu, J., Yuan, S., and Hu, C., 2016, "Numerical and Experimental Investigation of the Stratified Air-Oil Flow inside Ball Bearings," Int. J. Heat Mass Transf., **103**, pp. 619–626.

[60] Feldermann, A., Fischer, D., Neumann, S., and Jacobs, G., 2017, "Determination of Hydraulic Losses in Radial Cylindrical Roller Bearings Using CFD Simulations," Tribol. Int., **113**(March), pp. 245–251.

[61] Coulomb, C. A., 1785, *Théorie Des Machines Simples*.

[62] Barus G., 1893, "Isothermals, Isopiestics and Isomettrics Relative to Viscosity," Am. J. Sci., **45**, pp. 87–96.

[63] Roelands, C. J. . A., 1966, "Correlational Aspects of Viscous-Temperature-Pressure Relationships of Lubricating Oils," Delft University of Technology.

[64] Van Leeuwen, H., 2009, "The Determination of the Pressure-Viscosity Coefficient of a Lubricant through an Accurate Film Thickness Formula and Accurate Film Thickness Measurements," Proc. Inst. Mech. Eng. Part J J. Eng. Tribol., **223**(8), pp. 1143–1163.

[65] Ree, T., and Eyring, H., 1955, "Theory of Non-Newtonian Flow. Part I - Soldi Plastic

System, and Part II- Solution System of High Polymers," J. Appl. Phys., **26**(1), pp. p793-809.

[66] Johnson, K. L., 1970, "Regimes of Elastohydrodynamic Lubrication," J. Mech. Enginnering Sci., **12**(1), pp. 9–16.

[67] Nelias, D., 1994, "Power Loss of Gearbox Ball Bearing Under Axial and Radial Loads," Tribol. Ser., **37**(1), pp. 83–90.

[68] Geneix, J., 2007, "Rendement Des Mécaniques Engrenantes," thèse de Doctorat - Insa-Lyon - Université de Lyon.

[69] Habchi, W., and Bair, S., 2019, "Is Viscoelasticity of Any Relevance to Quantitative EHL Friction Predictions?," Tribol. Int., **135**(February), pp. 96–103.

[70] Parker, R. J., 1984, "Comparison of Predicted and Experimental Thermal Performance of Angular Contact Ball Bearings," NASA, **TP-2275**(February), pp. 1–16.

[71] Pouly, F., Changenet, C., Ville, F., Velex, P., and Damiens, B., 2010, "Power Loss Predictions in High-Speed Rolling Element Bearings Using Thermal Networks," Tribol. Trans., **53**(6), pp. 957–967.

[72] 2001, *ISO 14179-2: 2001. Gears – Thermal Capacity – Part 2: Thermal Load-Carrying Capacity, 14179-2.*

[73] 2001, *ISO 14179-1: 2001. Gears – Thermal Capacity – Part 1: Rating Gear Drives with Thermal Equilibrium at 95°C Sump Temperature, 14179-1*.

[74] Palmgren, A., 1967, *Les Roulements : Description, Théorie, Applications*.

[75] Boness, R. J., 1989, "Churning Losses of Disks and Gears Running Partially Submerged in Oil," Proc. 1979 Int. Power Transm. Gearing Conf. Chicago, Illinoise, **1**, pp. 255–359.

[76] Changenet, C., Leprince, G., Ville, F., and Velex, P., 2011, "A Note on Flow Regimes and Churning Loss Modeling," J. Mech. Des., **133**(12), p. 121009.

[77] Signer, H., Bamberger, E. N., and Zaretsky, E. V., 1974, "Parametric Study of the Lubrication of Thrust Loaded 120-Mm Bore Ball Bearings to 3 Million Ndm," ASME J Lubr. Technol., **96**, p. 524.

[78] Pinel, S. I., Signer, H. R., and Zaretsky, E. V., 2001, "Comparison between Oil-Mist and Oil-Jet Lubrication of High-Speed, Small-Bore, Angular-Contact Ball Bearings," Tribol. Trans., **44**(3), pp. 327–338.

[79] Harris T.A., 1998, "Tribological Performance Prediction of Aircraft Gas Turbine Mainshaft Ball Bearings," Tribol. Trans.

[80] Patir, N.; Cheng, H. S., 1965, "A Refined Solution to the Thermal-Elastohydrodynamic Lubrication of Rolling and Sliding Cylinders," A S L E Trans., **8**(4), pp. 397–410.

[81] Roulet, B., 1995, "Modelisation de l'évolution de La Dissipation de La Puissance et

Du Comportement Thermique d'une Boite de Viteses Manuelle," Thèse de Doctorat - Université Paris 6.

[82] Changenet, C., Oviedo-Marlot, X., and Velex, P., 2006, "Power Loss Predictions in Geared Transmissions Using Thermal Networks-Applications to a Six-Speed Manual Gearbox," J. Mech. Des., **128**(3), p. 618.

[83] Durand De Gevigney, J., Changenet, C., Ville, F., and Velex, P., 2012, "Thermal Modelling of a Back-to-Back Gearbox Test Machine: Application to the FZG Test Rig," Proc. Inst. Mech. Eng. Part J J. Eng. Tribol., **226**(6), pp. 501–515.

[84] Touret, T., Changenet, C., Ville, F., Lalmi, M., and Becquerelle, S., 2018, "On the Use of Temperature for Online Condition Monitoring of Geared Systems – A Review," Mech. Syst. Signal Process., **101**, pp. 197–210.

[85] Boni, J.-B., 2020, "Modélisation Thermique d'un Train Épicycloïdal Lubrifié Par Barbotage," Thèse de Doctorat - INSA-Lyon - Université de Lyon.

[86] Pouly, F., Changenet, C., Ville, F., Velex, P., and Damiens, B., 2010, "Investigations on the Power Losses and Thermal Behaviour of Rolling Element Bearings," Proc. Inst. Mech. Eng. Part J J. Eng. Tribol., **224**(9), pp. 925–933.

[87] Changenet, C., 2006, "Modélisation Du Comportement Thermique Des Transmissions Par Engrenages," Thèse de Doctorat - INSA-Lyon - Université de Lyon.

[88] Niel, D., Changenet, C., Ville, F., and Octrue, M., 2019, "Thermomecanical Study of High Speed Rolling Element Bearing: A Simplified Approach," Proc. Inst. Mech. Eng. Part J J. Eng. Tribol., **233**(4), pp. 541–552.

[89] Hannon, W. M., 2015, "Rolling-Element Bearing Heat Transfer—Part I: Analytic Model," J. Tribol., **137**(3), p. 031102.

[90] Neurouth, A., 2016, "Etude de La Performance Energetique d'une Transmission Mécanique," Thèse de Doctorat - INSA-Lyon - Université de Lyon.

[91] Muzychka, Y. S., and Yovanovich, M. M., 2002, "Thermal Resistance Models for Non-Circular Moving Heat Sources on a Half Space," J. Heat Transfer, **123**(4), p. 624.

[92] Holman, J., 2010, *Heat Transfert, Tenth Edition*, McGraw-Hill.

[93] Becker, K. M., 1963, "Measurements of Convective Heat Transfer from a Horizontal Cylinder Rotating in a Tank of Water," J. Heat Mass Transf., **6**, pp. 1053–1062.

[94] Duez, C., 2009, "Effets Du Mouillage En Hydrodynamique Macroscopique : Traînée , Impacts et Ruissellement," Hal, p. 209.

[95] Huyghe, J., Mondin, H., and Villeuneuve, J., 1961, *Transfert de Chaleur Par Mélange de Liquide et de Gaz En Convection Forcée Turbulente Avec Faible Vaporisation de La Phase Liquide*, Comité à L'Energie Atomique, Grenoble, France.

[96] Isbin, H. S., Moy, J. E., and Da Cruz, A. J. R., 1957, "Two-phase, Steam-water Critical Flow," AIChE J., **3**(3), pp. 361–365.

[97] Coe, H. H., and Zaretsky, E. V, 1978, "Predicted and Experimental Performance of Jet-Lubricated 120-Millimeter-Bore Ball Bearings Operating to 2,5 Million DN," NASA Tech. Pap., **TP-1599**(April).

[98] International Organization for Standardization, 2006, *ISO 76:2006. Rolling Bearings—Static Load Ratings*, Geneva.

[99] Quiban, R., *Personal Communication*, 1st June 2020.

[100] Jones, A. B., 1959, "Ball Motion and Sliding Friction in Ball Bearings," J. Basic Eng. (Transactions ASME), **81**(ser D), pp. 1–12.

[101] Ding, A. A., Zhao, S. K., and Zhou, F. Z., 2000, "A New Method of Calculating Rolling Element Attitude Angle in Ball Bearings," *Mechanical Engineering (ICME00)*, pp. 158–163.

[102] Lei, C., Rui, Z., Liu, J., Feng, R., and Zhao, J., 2010, "A New Method for Computing Contact Angle of High Speed Ball Bearing," 3rd Int. Jt. Conf. Comput. Sci. Optim. CSO 2010 Theor. Dev. Eng. Pract., **1**, pp. 331–334.

[103] Noel, D., Ritou, M., Furet, B., and Le Loch, S., 2013, "Complete Analytical Expression of the Stiffness Matrix of Angular Contact Ball Bearings," J. Tribol., **135**(4), pp. 1–8.

[104] Boussinesq, J., 1892, *Compt. Rend.*

[105] Bălan, M. R. D., Stamate, V. C., Houpert, L., and Olaru, D. N., 2014, "The Influence of the Lubricant Viscosity on the Rolling Friction Torque," Tribol. Int., **72**, pp. 1–12.

[106] Harris T.A., 1971, "Ball Motion in Thrust-Loaded, Angular Contact Bearings with Coulomb Friction .Pdf."

[107] Hong, S. W., and Tong, V. C., 2016, "Rolling-Element Bearing Modeling: A Review," Int. J. Precis. Eng. Manuf., **17**(12), pp. 1729–1749.

[108] Dowson, D., and Higginson, G. R., 1959, "A Numerical Solution to the Elasto-Hydrodynamic Problem," J. Mech. Eng. Sci., **1**(1), pp. 6–15.

[109] Sjoväll, H., 1933, "THe Load Distribution within Ball and ROller Bearings under Given External Radial and Axial Load," Tek. Tidskr. Mek, **9**.

FOLIO ADMINISTRATIF

THESE DE L'UNIVERSITE DE LYON OPEREE AU SEIN DE L'INSA LYON

NOM : Brossier DATE de SOUTENANCE :

(avec précision du nom de jeune fille, le cas échéant)

Prénoms : Pierre Joseph Benjamin

TITRE : Combined analytical and empirical modelling of power losses in Rolling Element Bearings

NATURE : Doctorat Numéro d'ordre : 2020LYSEI081

Ecole doctorale : MEGA ED 162

Spécialité : Mécanique

RESUME : Le développement de l'industrie du transport conduit la conception de transmissions mécaniques de puissance toujours plus légères et efficientes. Les composants de ces transmissions doivent supporter des efforts transmis dans des environnements de plus en plus restreints. Du fait que les carters soient devenus de plus en plus compacts, les systèmes de refroidissement se sont aussi complexifiés. C'est dans ce contexte que les paliers à roulement, plus communément appelés roulements, doivent produire moins de chaleur, opérer dans des espaces plus proches des engrènements, tout en ayant des durées de vie plus grandes. Le calcul des pertes énergétiques des roulements est essentiel pour quantifier la quantité d'huile à injecter pour refroidir ces composants. L'objectif de cette étude est donc de fournir des outils pour modéliser les pertes dans les roulements et leur comportement thermique

Dans un premier temps, une analyse bibliographique a été menée sur les pertes de puissance dans les roulements, incluant des modèles locaux et globaux de pertes de puissance. Un banc d'essais dédié a été utilisé afin d'analyser les puissances dissipées et la thermique de roulements à billes à gorge profonde. Les influences de la vitesse de rotation, du chargement, de la température d'injection, du débit d'huile injecté, des techniques de lubrification ont été examinées. Les modèles globaux précédemment investigués ont été comparés aux données expérimentales. Enfin, un modèle thermique a été développé pour comprendre l'influence des transferts de chaleur dans les pertes de puissance générées par les roulements. Des comparaisons entre différentes lubrifications et différentes géométries ont été faites. Une nouvelle formule du couple résistif a été proposée pour mieux prendre en compte la géométrie du roulement considéré.

MOTS-CLÉS : Palier de roulement, perte de puissance, résultats empiriques, modèle thermique

Laboratoire (s) de recherche : LamCos - LabECAM

Directeur de thèse : Fabrice Ville

Co-directeur de thèse : Christophe Changenet

Président de jury :

Composition du jury : Gorge Seabra ; Jean Bouyer ; Souad Harmand